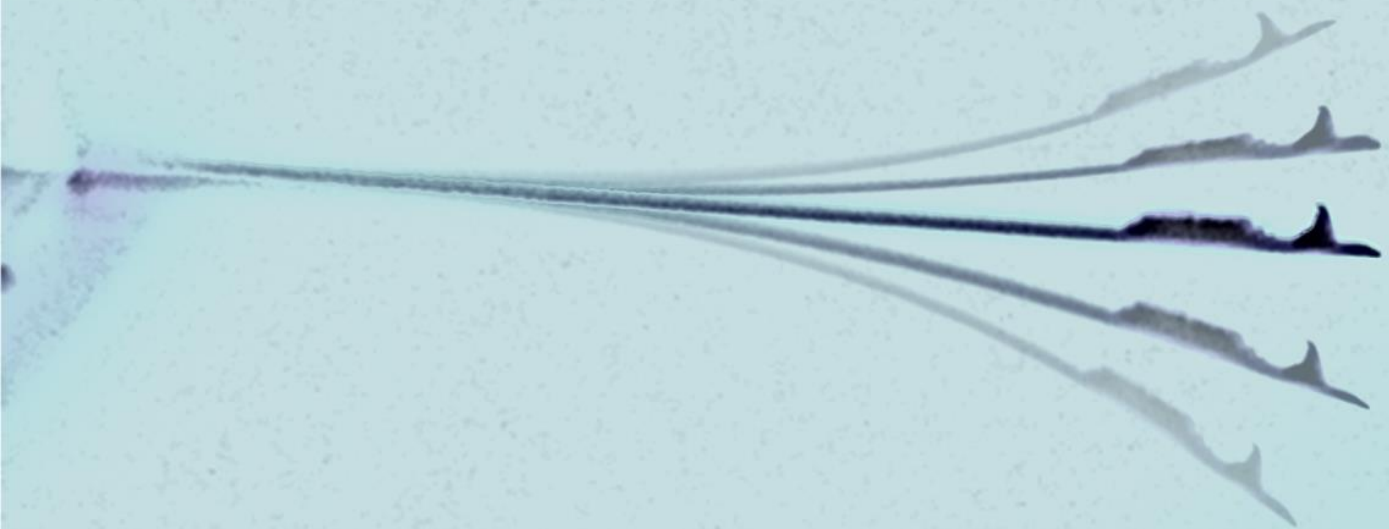


Department of Precision and Microsystems Engineering

**Mass and stiffness measurement using
a multi-modal analysis**

L.M.F.R. Hauzer

Report no : 2017.056
Coach : F. Alijani, M.K. Ghatkesar, P. Belardinelli
Professor : P.G. Steeneken
Specialisation : MNE / DMN
Type of report : MSc. thesis
Date : 11 December 2017



Mass and stiffness measurement using a multi-modal analysis

by

L.M.F.R. Hauzer

to obtain the degree of Master of Science
at the Delft University of Technology,
to be defended publicly on Monday December 11, 2017 at 10:00 AM.

Student number: 4079043
Project duration: January 15, 2017 – December 11, 2017
Thesis committee: Prof. dr. P.G. Steeneken, Delft University of Technology
Prof. dr. M. Amabili, McGill University
Dr. F. Alijani, Delft University of Technology
Dr. M.K. Ghatkesar, Delft University of Technology
Dr. P. Belardinelli, Delft University of Technology

An electronic version of this thesis is available at <http://repository.tudelft.nl/>.

Abstract

Biomechanics of cells have been identified as an important factor relating to their functionalities. Consequently, the need for sensitive measurement methods for mechanical analysis on the nano- and microscale is high. Micro-cantilever resonators can have a large impact in material determination at the nanoscale. When adding a material, the resulting shift in resonance frequency is associated with its mass and stiffness properties. The goal of this project is to exploit the contribution of higher flexural modes on the determination of both the density and Young's modulus of an added polymer on a micro-cantilever.

The identification of mass and stiffness is, in this thesis, restricted to the deposition of a two-photon polymerized layer on micro-cantilevers. A polymeric material is used, since cells are complex systems with viscoelastic properties, where polymers are less complex and mimic biological matter very well. Two configurations are investigated: an added polymer near the tip of the cantilever and a polymeric layer near the base of the beam. Experimentally and theoretically derived multi-modal analysis are linked, to decouple the mass and stiffness properties.

The added polymeric layer affects the resonance frequency of the system, which is found to be location and mode related. Decoupling of the mass and stiffness properties based on the modes with the largest frequency shift, lead to different outcomes compared to considering modes with the largest deflection and curvature at a specific location. The use of higher modes does affect the outcomes of the decoupling of mass and stiffness. Whether it leads to an increase on accuracy is yet elusive.

Preface

Almost a year ago I started on this project. Looking back to the beginning makes me realize how much knowledge I have gained through this hands-on project. Not only about mass and stiffness disentanglement, but about myself as well. I was supported by some people to push both the project and myself to a higher level.

First of all I would like to thank Peter Steeneken and my direct supervisors Farbod Alijani, Murali Ghatkesar and Pierpaolo Belardinelli. Despite having a busy schedule themselves, they always made time to give me feedback or help when needed. Their advices made me more puzzled sometimes, but forced me to take a step back, look at problems from a different perspective and eventually come up with a solution or alternative approach. The four of them provided me with all the equipment and knowledge to prevent stagnation of my project.

I would like to direct a word of thanks to Patrick van Holst, Harry Jansen, Rob Lutjjeboer and Spiridon van Veldhoven for their technical support and bad jokes in and around the laboratory. Paola Fanzio taught me a lot about the Nanoscribe system and was willing to help at any time, which I really appreciate. I would like to thank Bas Heming as well, for offering a telephone helpline while working with the Polytec system or network analyser. Furthermore I am thankful for Warner Venstra (Quantified Air B.V.) for lending his inkjet printer. Additionally he has been a big help in the usage of it.

During the year I spent time in the laboratory mostly, nonetheless I had a desk in the best office of the department. The fellow students in there were always longing for a coffee, waiting for the lunchbreak to start or just looking for someone to chat with. For this reason I would like to thank Thomas Gribnau, Bram van den Brink, Ryan van Dommelen, Bart Holtzer, Yannick Janssens, Pieter Kapel, Elena De Lazzari, Rens van der Nolle, Heleen Payens, Jimmy van Schoubroeck and Jelmer de Zeeuw for making my project more fun.

Last but certainly not least, I want to thank my family, boyfriend and friends for their endless support, for putting my problems in perspective and for offering distraction from my work during the weekends.

*L.M.F.R. Hauzer
Delft, 11 December 2017*

Contents

1 Literature review	3
1.1 Measurement methods	3
1.1.1 Stiffness measurement	3
1.1.2 Mass measurement	6
1.1.3 Micro- and nanomechanical systems - State-of-the-art	7
1.2 Theoretical model.	11
1.2.1 Analytical model	11
1.3 Summary	13
1.4 Research Question	13
2 Approach: Experiment and theory	15
2.1 Experiment: Cantilever dimensions.	16
2.2 Experiment: Deposition of material.	17
2.2.1 Dipping	18
2.2.2 Ink-jet technique.	18
2.2.3 Two-photon Laser Direct Writing	20
2.2.4 Material properties	22
2.3 Experiment: Cantilever multi-modal measurements	23
2.3.1 Actuation	23
2.3.2 Detection	23
2.4 Experiment: Cantilever parameters	25
2.5 Analytical Model: Modal Analysis	26
2.5.1 Modal analysis of a cantilever beam	26
2.5.2 Modal analysis of a cantilever beam with added polymer	26
3 Results	29
3.1 Deposition of a polymer by various methods	29
3.1.1 Dipping	29
3.1.2 Ink-jet printing of a water-soluble polymer	30
3.1.3 Two-photon polymerization	31
3.1.4 Discussion on deposition methods	31
3.2 Polymer location	33
3.3 Modal analysis	33
3.4 Disentangling of mass and stiffness.	37
3.4.1 Validation	37
3.4.2 Decoupling of mass and stiffness based on the frequency shift contribution.	37
3.4.3 Decoupling of mass and stiffness based on the absolute deflection and curvature	38
3.4.4 Comparison between both approaches	40
4 Discussion	43
4.1 Deposition of a polymer	43
4.2 Multi-modal analysis	44
4.2.1 Difference in amplitude of the peaks before and after deposition of material	44
4.2.2 Differences in the resonance frequency shift between samples	46
4.3 Theoretical model.	47
4.4 Decoupling of mass and stiffness	48

5	Conclusion	49
6	Recommendations	51
	Appendix	53
A	ManualControl Nanoscribe	53
B	Cantilever fabrication process	55
C	Determining mode shapes	56
D	Results desktop printer	58
E	Results Nanoscribe	60
F	Optimization results	61
F1	Modal analysis	61
F2	Single-mode approach by using literature values	63
F3	Single-mode approach by combining different locations	66
F4	Multi-mode approach by using literature values	67
F5	Multi-mode approach by combining different locations	68
F6	Raw data of single- and multi-mode approach	70
F7	Participation factors	79
F8	Combining modes with the largest participation factor	80
G	Differences between two approaches	85
H	Combining multiple modes	86
I	Clamping effect	87
J	Validation for the Young's modulus via an indentation method	90
K	Cantilever profile	92
L	Experimentally derived mode shapes	93
M	Improve adhesion.	95

List of Figures

1	This figure shows a histogram of peak frequency shifts caused by two different bacteria flowing through a resonator [1]. The brown coloured data corresponds to Escherichia coli and the blue coloured bars to Bacillus subtilis bacteria.	1
2	Results of obtained cell stiffness through cyto-indentation [2]. The y-axes indicate the number of cells and the x-axes show the measured Young's modulus. The results obtained from cancerous cells are shown in Figure a. and from normal cells in Figure b.	1
1.1	An AFM can be used for indentation or for deriving a map of the surface topology of a sample. The setup consists of a laser, a photodetector, a piezoelectric actuator, a cantilever with a sharp tip on the end and the necessary electronics. The actuator controls the displacement of the cantilever. When the tip comes close to the sample surface, the cantilever will bend due to forces between the tip and the sample. The deflection is detected via a laser and a photodetector. Such deflection can be combined with the spring constant of the cantilever in order to determine the experienced force. [3]	4
1.2	Optical magnetic twisting cytometry tests applied to a red blood cell. An applied magnetic field, normal to the magnetization of the bead, generates a torque on the bound bead. The resulting torque deforms the cell with the resultant rotating and translating bead. The in-plane displacement of the bead is tracked optically. [4]	4
1.3	Schematic explanation of how a cell is stretched by optical tweezers [5]. Human red blood cells have been directly stretched using optical traps to maximum forces of 60 pN by recourse to two or three bead attachments on cell surfaces.	5
1.4	Cells flow through a microfluidic channel. When trapped by two counterpropagating divergent laser beams, the cell deforms as a result of the induced surface force created by the laser beams. The technique is called microfluidic optical stretching. [6]	5
1.5	Mass spectrometry enables mass-to-charge ratio measurements of molecular species. A sample is ionized by bombarding it with electrons. During this process molecules can break into charged fragments. The ions are accelerated and are subjected to a magnetic field. The field forces the ions to deflect. Ions with the same mass-to-charge ratio will undergo the same amount of deflection. A detector is able to detect the ions. By correlating known masses to the sample masses, the atoms or molecules can be identified. The relative number of ions generated is plotted against their mass-to-charge ratio. This mass spectrum can be compared to characteristic fragmentation patterns for identification purposes as well.	6
1.6	Interaction forces between the cantilever and biomolecules can cause the cantilever to bend upwards. [8] In the research a pre-functionalized cantilever was used to investigate nanomechanical changes at the interface when binding with lipid vesicle.	7
1.7	This pictures is derived from a FEM simulation by Malvar <i>et al.</i> [9] to investigate the effect of the contact area on the mechanical coupling between the adsorbate and the cantilever. The larger the contact area, the higher the effect on the mechanical coupling will be.	7
1.8	The relative eigenfrequency shift is plotted against the ratio between the thickness of a uniformly adsorbed layer and a cantilever [10]. The symbol ω_1 represents the first resonance frequency of a cantilever and ω_2 depicts the resonance frequency after deposition of the layer. Silicon [Si] has a density of 2330 kg m^{-3} and a Young's modulus of 169 GPa. The self-assembled monolayer from the left blue graph has a density of 675 kg m^{-3} and a Young's modulus of 12.9 GPa. The right red graph has a myosin monolayer with a density of 183 kg m^{-3} and a Young's modulus of 0.7 GPa.	8
1.9	The two pictures show the relation of the mass and stiffness response with respect to the mode shape of a cantilever. It can be seen in the upper picture, representing the first bending mode, that the stiffness effect is high near the base while the mass effect overrules at the tip of the cantilever. The lower picture shows the effects for the second bending mode. It demonstrates that the mass and stiffness effect cancel each other out at the anti-node. [11]	9

1.10	The location of an attached particle can be obtained by using a graph shown in this figure [12]. The mass ratio ($\Delta m/m_0$) is plotted against the position of a particle for all possible locations along a cantilever (z/L). The resulting graphs are different per mode but they intersect at a specific point. The location corresponds to the real position of the particle and its mass. In this situation, the intersection is found at $z/L=0.8$ and $\Delta m/m_0 \approx 10^{-2}$ and is highlighted with an arrow.	11
1.11	A side view of a solid cantilever is shown on the left-hand side of the figure. The right-hand side of the figure presents a mid-section of the cantilever.	12
2.1	This image shows the coarse process steps of the method. Initially, a cantilever has to be selected. The resonance response has to be measured. Subsequently, a material needs to be deposited on the cantilever. The frequency response of this system has to be obtained as well. Both frequency spectra have to be evaluated by a computational model. eventually the mass and stiffness properties of the added material should be the final result.	15
2.2	The main components of a scanning electron microscope [SEM] are shown in this schematic drawing. The electron gun produces the electrons which are subsequently accelerated by a high electric potential. The magnetic lenses ensure the focus of the beam on the specimen. The scanning coil enables the scanning over the sample surface. Electrons from the beam that collide with electrons in the object are knocked out of their usual orbits. These secondary electrons can be traced with detectors that are placed in the sample chamber. Images are generated depending on the contrast in the magnitude of the signals obtained while scanning. The whole process takes place in vacuum since air molecules can cause the electrons to scatter. This would affect the quality of the picture. [3]	16
2.3	This graph shows the sputter rate as a function of the plasma current for different targets.[13]	16
2.4	The three investigated deposition methods are dipping (a.), the ink-jet technique (b.) and 3-D direct laser writing (c.).	17
2.5	This photograph shows the setup for dipping. A 3-D printed head is mounted on the arm of the MiBot. A chip with cantilever is attached to the mount with glue. Using the MiBot underneath a microscope, enables a clear view on the process via a computer screen.	18
2.6	The Epson Stylus SX235 desktop printer that is used for ink-jet based experiments.	19
2.7	The setup of the ink-jet printer with one nozzle only. The upper part with the nozzle, camera and strobe light can be moved up and down to control the distance between the nozzle and the sample.	19
2.8	The focal point of a laser beam is shown in picture a. A darker red area represents a higher intensity. The corresponding two-dimensional graph is shown in b. where the squared relation between the excitation intensity and x can be seen. FWHM is the abbreviation for Full Width at Half Maximum. The purple colour in graph c. shows the polymerized volume caused by the laser in a resin. As can be seen in subfigure d., the width of the graph at the polymerization threshold corresponds to the writing resolution. When the laser intensity is decreased in subfigure e., the resolution increases [14].	20
2.9	The solidified resin can form a structure as shown in this picture. This is only possible when writing in three (x, y and z) directions is possible [14].	20
2.10	The setup of a cantilever in the Nanoscribe can be seen in this figure. The glass substrate is placed in a holder above the lens. A piece of glass is mounted on top of the substrate to create a known distance between the cantilever and the glass substrate. The chip is placed up-side-down on the glass piece such that the cantilever is not supported. The dimensions are exaggerated to create more clear overview.	21
2.11	The setup shown in this figure [15] is used for the clamping and actuation of the cantilever. A spring is used to keep the cantilever chip in place on top of a piezoelectric actuator. In between the actuator and the chip, a piece of PDMS is placed for an increase in contact.	23

2.12	A variation of detection methods to measure the deflection of a beam [3]. (a) Optical detection. (b) This method uses a Scanning Tunnelling Microscope tip to measure the change in tunnelling current caused by a variation of distance between the tip and the surface. (c) Piezoresistive material has a changing resistance due to the strain that is caused by bending. (d) The cantilever and a parallel plate act like a parallel-plate capacitor. Deflection is detected because of the changing distance between the two parts. (e) Optical interferometry. The distance affects the interference pattern.	23
2.13	The setup that is used for the detection of the frequency response is visualised in this figure. A laser Doppler vibrometer [Polytech, MSA 400] is used to measure the velocity and displacement of the sample, which is placed underneath the lens. A vibrometer controller [Polytech, OFV-5000], junction box [Polytech MSA-400], computer [Polytech, DMS] regulate all the electronics.	24
2.14	Solid cantilever side view and cross section	26
2.15	Solid cantilever with adsorbate side view and section	27
3.1	These pictures show how a cantilever is dipped into a droplet of water. Figure a. shows a cantilever that is approaching the edge of a droplet. It touches the droplet in b. and pushes against it in c. and d. In e. the cantilever has enough force to break through the surface stress and enter the droplet as shown in f. When retracting the cantilever from the droplet as visualised in g., h. and i., one can see that no liquid is withdrawn by the cantilever. The surface is hydrophobic.	29
3.2	EPSON Stylus SX235W desktop printer.	30
3.3	Droplets of a solution of PEDOT:PSS in water (1 mL PEDOT:PSS (1.3%wt) : 10 mL H ₂ O) are deposited on a cantilever. The most left picture a. shows the situation with one added droplet. Photos b., c. and d. show 4, 7 and 10 droplets respectively.	30
3.4	The first result derived via two-photon polymerization is shown in this figure, obtained via an optical microscope. A well shaped blue cube can be seen. The colour is due to the light of the microscope.	31
3.5	The Nanoscribe system contains a camera to enable sight on the writing process. This picture is taken with this camera after the polymerization process while the cantilever chip was in the system. The location and shape of the result are visible.	31
3.6	An SEM picture of the adsorbate on sample tip ₁ . The cantilever tip is pointing to the right. It can be seen that delamination has occurred on the upper layer near the end.	33
3.7	An SEM picture of sample tip ₁ . The added polymer is located near the tip of the cantilever.	33
3.8	An SEM image from the side of the adsorbate on a coloured sample near the base (base ₁).	33
3.9	An SEM picture of sample base ₁ . The added polymer is located near the base of the cantilever, highlighted with a yellow colour.	33
3.10	This figure shows the frequency response of a bare cantilever represented by the blue line. An added layer IP-L 780 ($\pm 50 \times 50 \times 3 \mu\text{m}$) is deposited near the tip, highlighted with colour. (sample tip ₁)	33
3.11	This figure shows the frequency response of a bare cantilever represented by the blue line. The picture on the right depicts the same cantilever with a false-coloured added cube IP-L 780 ($\pm 50 \times 50 \times 3 \mu\text{m}$) near the clamping. (sample base ₁)	34
3.12	The relation between the deposition location and frequency shift per mode is shown in this graph. The thinner the line, the higher the mode. The dotted red lines represent the locations from the experiments of this research.	35
3.13	In this figure, the location of the centre of mass is compared with the operational deflection shape per mode for sample tip ₁	35
3.14	In this figure, the location of the centre of mass is compared with the operational deflection shape per mode for sample base ₁	35
3.15	The squared deflection of mode shapes 1 to 5 is plotted against the location on a clamped cantilever in this figure. It can be seen that the deflection near the base increases at higher modes. The deflection near the tip decreases at higher modes.	36
3.16	The squared curvature of mode shapes 1 to 5 is plotted against the location on a clamped cantilever in this figure. It can be seen that the curvature near the base increases at higher modes. Furthermore, higher modes induce a larger curvature on an added layer near the tip.	36

3.17	The left graph shows the ρ of the added material of sample tip ₁ per mode, that corresponds to a Young's modulus of 1 (blue line), 1.5 (orange line) or 2 GPa (yellow line). The right graph shows the corresponding error between the experimental and theoretical values that is minimised. The grey area represents the values from literature. The dashed lines are added to guide the eye.	37
3.18	In the left graph, the values for E can be obtained from corresponding densities of 1000 kgm ⁻³ (blue line) and 2000 kgm ⁻³ (orange line) per mode. The grey area represents the values from literature. The minimum difference found on the experimental and theoretical values are shown in the graph on the right. The dashed lines are added to guide the eye.	38
3.19	The two graphs show the normalized participation factors for sample tip ₁ per mode. The left figure gives insight in the participation of mass and the graph on the right-hand side shows the influence of stiffness. The dashed lines are added to guide the eye.	38
3.20	The two graphs show the normalized participation factors for sample base ₁ per mode. The left figure gives insight in the participation of mass and the graph on the right-hand side shows the influence of stiffness. The dashed lines are added to guide the eye.	39
3.21	These graphs show experimentally and theoretically derived resonance frequency shifts per mode. The dashed lines are added to guide the eye. For subfigure a., the theoretical outcomes are obtained from a density of 1939.18 kgm ⁻³ and a Young's modulus of 2.85 GPa. The outcomes shown in subfigure b. are derived via a ρ of 1389.42 kgm ⁻³ and an E of 4.23 GPa. The samples with an added polymeric layer near the base showed different outcomes for both approaches: The density and Young's modulus via the modes with the largest absolute values for deflection and curvature (red points) in c. are 1101.21 kgm ⁻³ and 0.93 GPa and in d. are 2445.11 kgm ⁻³ and 2.21 GPa, respectively. The yellow points are based on modes with the largest frequency shift contribution and show the resulting change in frequency from a density of 630.18 kgm ⁻³ and a Young's modulus of 0.38 GPa in subfigure c. and a density of 1623.91 kgm ⁻³ and a Young's modulus of 1.24 GPa in subfigure d.	41
3.22	These figures show experimentally and theoretically derived resonance frequency shifts per mode. The theoretical values are obtained by combining the first three, four, five or six flexural modes. The lower modes resulted in infeasible values compared to the values from the literature. The dashed lines are added to guide the eye.	42
4.1	Delamination of layers occurred in sample tip ₁ (a.), base ₁ (b.) and base ₂ (c.). It can even be seen that the polymeric layer is not fully adhered to the cantilever surface for sample base ₂ (c.)	43
4.2	This image visualises the effect of shrinkage on voxel lines on the left-hand side. This causes a bending moment when multiple voxel lines are manufactured parallel and adjacent. [16]	43
4.3	The location of the laser influences the results. As can be seen in picture a.), the fifth flexural mode is visible while the fourth flexural mode is not. Figure b.) on the other hand shows the fourth mode while the fifth mode is invisible. It can be concluded that the laser is pointed directly on a nodal point of an invisible node.	44
4.4	When the laser is not directed at the centreline of the cantilever, torsional modes will arise in the results. They are visible in picture a.). The difference with a measurement on the centreline is shown in picture b.). The peak that is pointed out with the most left red arrow is a combination of the first torsional mode and the second flexural mode. The red arrow in the middle shows the location of the first torsional mode and the most right arrow clarifies the second torsional mode.	45
4.5	Tests on the clamping effect resulted in normal distributions of the Q-factor per mode as shown in this figure.	45
4.6	A normal distribution on the resonance frequency of a cantilever beam is shown for five bending modes. The variation increases for higher modes.	46
4.7	The frequency shift of two samples tip ₁ and tip ₂ caused by an adsorbate on similar locations but a different thickness are compared in this graph.	46
4.8	The frequency shift of samples base ₁ and base ₂ is shown in this figure. The changes caused by a polymer on similar locations, are compared in this graph.	47
4.9	The writing directions during the two-photon polymerization process are shown in this graph. Sample tip ₁ (a.), tip ₂ (b.) and base ₁ (c.) are written in the direction of the width of the cantilever. Sample base ₂ (d.) is written along the length of the beam.	47

4.10	The experimentally derived mode shapes for sample tip ₁ are shown in this figure. A blue coloured line represents the shape obtained for the bare cantilever and the red line shows the shape of the cantilever with a polymeric layer near the tip.	48
4.11	The experimentally derived mode shapes for sample base ₁ are shown in this figure. A blue coloured line represents the shape obtained for the bare cantilever and the red line shows the shape of the cantilever with a polymeric layer near the base.	48
4.12	The quality of the adhesion of the polymeric layer on the cantilever surface is unknown. It could be the case that the layer is only adhered to the cantilever via the bottom of a voxel as shown in subfigure a. However, a contact area as shown in subfigure b. and c. are possible as well. Sample base ₂ had shown detachment from the surface at many locations. Maybe the contact area will look like as sketched in subfigure d.?	48
6.1	The process steps for the fabrication of AFM probes are shown in this figure. [17]	55
6.2	The $U_n(x),x$ -graphs represent a side-view of the first five mode shapes (n) of a cantilever. The cantilever is clamped at $x=0$ and has a length L.	57
6.3	Polystyrene beads of $\sim 5\mu m$ in a water droplet. The agglomeration of beads is clearly visible a. within the droplet and b. on the edge of the droplet. The agglomeration on the side is caused by the evaporation of the water. The amount of evaporation over the surface of the droplet is equal, which causes the droplet to shrink. Accordingly, the outer particles are pushed to the inside, resulting in the 'coffee stain effect'.	58
6.4	A white light interferometer picture of 40 small-sized droplets of PEDOT:PSS printed on glass with an EPSON Stylus SX235W desktop printer.	58
6.5	An AFM picture of 40 small-sized droplets of PEDOT:PSS printed on glass with an EPSON Stylus SX235W desktop printer.	58
6.6	Results obtained when printing 40 small sized droplets of PEDOT:PSS in water printed on a specific location using an EPSON desktop ink-jet printer [Epson Stylus SX235W]. The scale-bar in picture a. depicts a length of 200 μm , for b. to g. it represents 30 μm	59
6.7	A white light interferometer picture of 150 medium-sized droplets of PEDOT:PSS printed on glass with an EPSON XP-235 desktop printer.	59
6.8	This figure shows three different results when writing cubes of 50x50 μm with different settings on a glass substrate. Subfigure a. has too large hatching and slicing distances. Separate voxel lines are visible. Subfigure b. and c. have a too low and too high laser power, respectively.	60
6.9	For the investigation on the right settings, print jobs like the one in this figure were performed. The columns show an increase in laser power, the rows an increase in scan speed.	60
6.10	When writing over a polymerized part, bubbles arise as shown in this figure. By stopping the process, the bubbles often disappear. The picture is taken by a camera within the Nanoscribe system.	60
6.11	An SEM image of a second sample with a polymeric layer near the tip of a cantilever can be seen in this figure. Its thickness is smaller than that of the cantilever. Contamination on the bottom side of the cantilever is revealed by this picture.	61
6.12	An SEM picture of sample tip ₂ . The added polymer is located near the tip of the cantilever.	61
6.13	The blue line in this figure represents the frequency response of a bare cantilever. A fake coloured orange cube IP-L 780 ($\pm 50 \times 50 \times 3 \mu m$) is added near the tip. (sample tip ₂)	61
6.14	In this figure, the location of the centre of mass is compared with the operational deflection shape per mode for sample tip ₂	62
6.15	This picture shows the side of the added material on the cantilever (sample base ₂). As can be seen, the adhesive forces between the added layer and the cantilever were not strong enough, resulting in a release of material at multiple locations.	62
6.16	An SEM picture of sample base ₂ . The added polymer is located near the base of the cantilever.	62
6.17	This graph figures the frequency response of a bare cantilever represented by the blue line. The added cube IP-L 780 ($\pm 50 \times 50 \times 3 \mu m$) is deposited near the clamping and highlighted with a fake colour (orange). The material is deposited in lines over the length of the cantilever.(sample base ₂)	62
6.18	In this figure, the location of the centre of mass is compared with the operational deflection shape per mode for sample base ₂	63

6.19	The left graph shows the ρ of the added material of sample tip ₁ per mode, that corresponds to a Young's modulus of 1 (blue line), 1.5 (orange line) or 2 GPa (yellow line). The right graph shows the corresponding error between the experimental and theoretical values that is minimised. The grey area represents the values from literature.	64
6.20	The ρ of the adsorbate of sample tip ₂ that corresponds to a Young's modulus of 1 (blue line), 1.5 (orange line) or 2 GPa (yellow line) per mode is shown in the left graph. The grey area represents the values from literature. The right graph gives information on the corresponding error between the experimental and theoretical values that is minimised.	64
6.21	In the left graph, the values for E can be obtained from corresponding densities of 1000 kgm ⁻³ (blue line) and 2000 kgm ⁻³ (orange line) per mode. The grey area represents the values from literature. The minimum difference found on the experimental and theoretical values are shown in the graph on the right.	65
6.22	The Young's moduli that are related to densities of 1000 kgm ⁻³ (blue line) and 2000 kgm ⁻³ (orange line) per mode are shown in the left graph. The minimum variation found on the experimental and theoretical values are shown in the graph on the right. The grey area represents the values from literature.	65
6.23	The outcomes from the combination of samples with a polymeric layer near the tip and samples with an added polymer near the base are shown in this Figure. The graph on the left-hand side shows the density values per mode, where the graph on the right shows the corresponding Young's moduli. No convergence was obtained when minimizing the RMS error for three combinations on mode 5 and are therefore missing.	66
6.24	This graphs show the results of a multi-mode approach for sample tip ₁ . Young's moduli of 1 (blue line), 1.5 (orange line) or 2 GPa (yellow line) are used to obtain the density of the added polymer (graph on the left-hand side) and the corresponding RMS error (graph on the right-hand side). The grey area corresponds to the values for ρ from literature.	67
6.25	A multi-mode approach for sample tip ₂ resulted in densities as shown on the left and RMS errors as presented on the left side of the figure. Young's moduli of 1 (blue line), 1.5 (orange line) or 2 GPa (yellow line) are used.	67
6.26	The graph on the left of this figure shows the Young's moduli corresponding to densities of 1000 (blue line) and 2000 kgm ⁻³ (orange line). The second graph shows the RMS error.	68
6.27	Densities of 1000 (blue line) and 2000 kgm ⁻³ (orange line) are used for the obtaining of the Young's moduli. The corresponding RMS errors are plotted on the right-hand side. The grey area represents the values for E from literature.	68
6.28	A recursive approach between two different samples has lead to Young's moduli and values for the density of the added polymer. All the combinations are shown in this figure where the graph on the left shows the values for E and the most right graph shows the values for ρ . The grey areas represent the literate values.	69
6.29	The participation factors for sample tip ₁ , normalised with respect to the largest value, are shown in these graphs. The figure on the left-hand sides shows the weighting factors regarding the mass and the figure on the right shows the participation factors per mode regarding the stiffness. The dashed lines are added to guide the eye.	80
6.30	The participation factors for sample tip ₂ , normalised with respect to the largest value, are shown in these graphs. The figure on the left-hand sides shows the weighting factors regarding the mass and the figure on the right shows the participation factors per mode regarding the stiffness. The dashed lines are added to guide the eye.	81
6.31	The participation factors for sample base ₁ , normalised with respect to the largest value, are shown in these graphs. The figure on the left-hand sides shows the weighting factors regarding the mass and the figure on the right shows the participation factors per mode regarding the stiffness. The dashed lines are added to guide the eye.	82
6.32	The participation factors for sample base ₂ , normalised with respect to the largest value, are shown in these graphs. The figure on the left-hand sides shows the weighting factors regarding the mass and the figure on the right shows the participation factors per mode regarding the stiffness. The dashed lines are added to guide the eye.	83

6.33	The results for the combination of two modes from one sample are shown in this scatter plot. The samples with a polymer near the tip derived ρ from the lower and E from the higher modes. Conversely, the samples with base-located polymers used lower modes to find E and higher modes to find ρ . The grey area represents the literature values. For the mode combinations within a square, the modes with a largest mass and largest stiffness effects are combined.	84
6.34	The participation factor based on mass depends on the location and spread of the added polymer. This graph shows the modes with the highest participation factors for different locations and lengths. The properties of base ₂ are used to freeze the other variables.	84
6.35	The participation factor based on stiffness depends on the location and spread of the added polymer. This graph shows the modes with the highest participation factors for different locations and lengths. The properties of base ₂ are used to freeze the other variables.	85
6.36	This box plot shows the influence of the clamping on the Q-factor for the first five flexural modes. One beam was clamped, measured and taken out of the set-up for ten times. The Q-factor was determined by Polytech software which is based on a curve fit of one peak and subsequently using the -3 dB method.	87
6.37	The box plots in this figure clarify the deviations in the Q-factor, due to the clamping. One beam was clamped, measured and taken out of the set-up for ten times. The Q-factor was determined by Polytech software which is based on a curve fit of one peak and subsequently using the -3 dB method.	88
6.38	From this figure it can be seen that the deviation in resonance frequencies due to clamping is low. The spread of the whisker plots are small. One beam was clamped, the resonance frequency for each mode was measured and afterwards the cantilever chip was taken out of the set-up for ten times in a row.	89
6.39	This whisker plots show the effect of the clamping on the resonance frequency of the cantilever. One beam was clamped, measured and taken out of the set-up for ten times in a row.	89
6.40	This graph represents the experimental results of an AFM indentation experiment. The orange part of the curve can be evaluated using the Hertz model. In this way, the Young's modulus of the sample can e determined.	90
6.41	Theoretically and experimentally derived force, distance-curves are plotted in this figure. The red coloured lines represent the results for a MICA sample, the blue lines show the results for the IP-L 780 sample. Dashed lines give information on theoretical values.	91
6.42	The profiles of the cantilevers before and after the deposition of a polymeric layer are shown in this figure. They are derived with an SEM. Beam 2 is sample tip ₁ , beam 4 sample base ₁ , beam 7 sample base ₂ and beam 10 sample tip ₂ . Only beam 2 shows a small distortion due to the polymer.	92
6.43	The experimentally derived mode shapes for sample tip ₁ are shown in this figure. The coloured shapes on the foreground are after the deposition of a polymeric layer. A red colour relates to a positive displacement of the measured point and the green colour represents a negative displacement. The grey shapes on the background are obtained from the bare cantilever.	93
6.44	The experimentally derived mode shapes for sample base ₁ are shown in this figure. The coloured shapes on the foreground are after the deposition of a polymeric layer. A red colour relates to a positive displacement of the measured point and the green colour represents a negative displacement. The grey shapes on the background are obtained from the bare cantilever.	93
6.45	The experimentally derived mode shapes for sample base ₂ are shown in this figure. The coloured shapes on the foreground are after the deposition of a polymeric layer. A red colour relates to a positive displacement of the measured point and the green colour represents a negative displacement. The grey shapes on the background are obtained from the bare cantilever.	94
6.46	The experimentally derived mode shapes for sample tip ₂ are shown in this figure. The coloured shapes on the foreground are after the deposition of a polymeric layer. A red colour relates to a positive displacement of the measured point and the green colour represents a negative displacement. The grey shapes on the background are obtained from the bare cantilever.	94

List of Tables

2.1	An overview of the available IP photoresists from Nanoscribe. [18]	22
2.2	The material properties of the used materials are listed in this table.	22
2.3	This table lists the properties of the cantilever that is chosen for this research [19].	25
3.1	The advantages and disadvantages of the three experimentally investigated deposition methods are listed in this table. Because of the control of the shape and location of the polymerized structure, two-photon polymerization is chosen to be the method to continue with.	32
3.2	The values for the frequency shift of caused by a polymeric layer near the tip of a cantilever are listed in this table.	34
3.3	Sample base ₁	34
3.4	Two modes of sample tip ₁ are used to derive the values in this table. The RMS error is minimized to find ρ from one and E from another mode. It can be seen that combinations of modes with a high participation factor give feasible results.	39
3.5	Two modes of sample base ₁ are used to derive the values in this table. The RMS error is minimized to find ρ from one and E from another mode. It can be seen that combinations of modes with a high participation factor give feasible results.	40
3.6	This table presents the resulting Young's modulus and density for an approach where the relation between the deposition location and the frequency shift contribution are used.	40
3.7	This table presents the resulting Young's modulus and density for an approach where the modes with the largest participation factor for mass and stiffness are combined per sample.	40
3.8	This table presents the material properties of the polymeric layer for an approach where the RMS error for a combination of all the measured modes is minimised.	41
6.1	The measured frequencies of sample (sample tip ₂) before and after the deposition of material on beam tip ₂ and the exact change and the difference in percentage.	63
6.2	sample base ₂	63
6.3	The raw data of single- and multi-mode method for sample tip ₁ is presented in this table. The RMS value is minimized to find ρ for a given E .	70
6.4	The raw data of single- and multi-mode method for sample tip ₂ is presented in this table. The RMS value is minimized to find ρ for a given E .	71
6.6	The raw data of single- and multi-mode method for sample base ₂ is presented in this table. The RMS value is minimizes to find E for a given ρ .	71
6.5	The raw data of single- and multi-mode method for sample base ₁ is presented in this table. The RMS value is minimizes to find E for a given ρ .	74
6.7	This table presents the outcomes of a recursive method between samples tip ₁ and base ₁ . The values for the density are derived from sample tip ₁ and the Young's modulus from base ₁ .	75
6.8	This table presents the outcomes of a recursive method between samples tip ₁ and base ₂ . The values for the density are derived from sample tip ₁ and the Young's modulus from base ₂ .	76
6.9	This table presents the outcomes of a recursive method between samples tip ₂ and base ₁ . The values for the density are derived from sample tip ₂ and the Young's modulus from base ₁ .	77
6.10	This table presents the outcomes of a recursive method between samples tip ₂ and base ₂ . The values for the density are derived from sample tip ₂ and the Young's modulus from base ₂ .	78
6.11	The participation factors for mass, per mode, for all samples. The numbers are normalised with respect to the largest value.	79
6.12	The participation factors for stiffness, per mode, for all samples. The numbers are normalised with respect to the largest value.	79
6.13	A recursive approach between two modes of sample tip ₁ is used to derive the values in this table. The RMS error is minimized to find ρ from the lower and E from the higher mode.	80

6.14 A recursive approach between two modes of sample tip ₂ is used to derive the values in this table. The RMS error is minimized to find ρ from the lower and E from the higher mode.	81
6.15 A recursive approach between two modes of sample base ₁ is used to derive the values in this table. The RMS error is minimized to find E from the lower and ρ from the higher mode.	82
6.16 A recursive approach between two modes of sample base ₂ is used to derive the values in this table. The RMS error is minimized to find E from the lower and ρ from the higher mode.	83
6.17 This table gives a list of statistic values from combinations of two modes from one sample. The mean value, variance and standard deviation are given for E and ρ per sample.	84
6.18 Sample tip ₁ gives the listed results for a density of 1939.18 kgm ⁻³ and a Young's modulus of 2.85 GPa.	85
6.19 Sample tip ₂ gives the listed results for a density of 1389.42 kgm ⁻³ and a Young's modulus of 4.23 GPa.	85
6.20 Sample base ₁ gives the listed results for a density of 1101.21 kgm ⁻³ and a Young's modulus of 0.93 GPa.	85
6.21 Sample base ₂ gives the listed results for a density of 2445.11 kgm ⁻³ and a Young's modulus of 2.21 GPa.	86
6.22 Sample base ₁ gives the listed results for a density of 630.18 kgm ⁻³ and a Young's modulus of 0.38 GPa.	86
6.23 Sample base ₂ gives the listed results for a density of 1623.91 kgm ⁻³ and a Young's modulus of 1.24 GPa.	86
6.24 This table lists the resulting material properties when combining multiple modes and minimizing the RMS error.	86
6.25 This table lists the measured Q-factors for the first five modes of ten different tests. For each test a cantilever is clamped in the setup.	87
6.26 The resonance frequencies of the first five modes are measured for a cantilever in ten different tests. For each test, the cantilever was clamped in the setup. The results are listed below.	88

Introduction

Nowadays, people are surrounded by large structures such as bridges, skyscrapers and cranes. It is possible to safely design and build these structures on a macroscale since the mechanical properties of the materials used are known. These characteristics are often unknown on nano- and microscales. Consequently, the need for sensitive measurement methods upon these scales is high.

To create a feeling for the impact that a precise measurement of mechanical properties could have, a medical application could be an example. Mass measurements can be used for differentiation between bacteria (Figure 1). Stiffness measurements help to distinguish metastatic from normal cells (Figure 2), even if no morphological difference is found. When a life threatening disease, such as cancer, is detected in an early stage, the chances of surviving are higher. A good understanding of the mechanisms of cells is crucial in order to develop treatment.

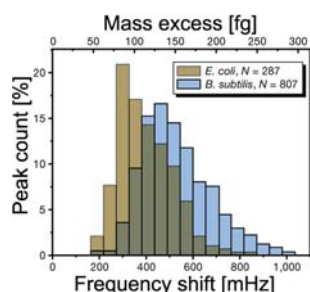


Figure 1: This figure shows a histogram of peak frequency shifts caused by two different bacteria flowing through a resonator [1]. The brown coloured data corresponds to *Escherichia coli* and the blue coloured bars to *Bacillus subtilis* bacteria.

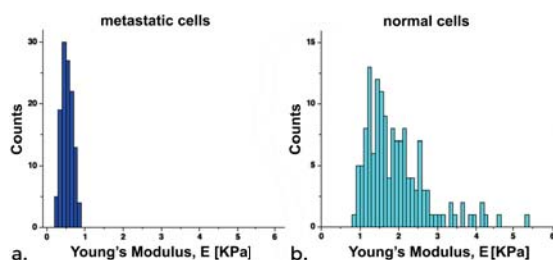


Figure 2: Results of obtained cell stiffness through cyto-indentation [2]. The y-axes indicate the number of cells and the x-axes show the measured Young's modulus. The results obtained from cancerous cells are shown in Figure a. and from normal cells in Figure b.

In summary, the determining of mass and stiffness on the nano- and microscales could have a large impact. Several techniques are adopted for measurement at the microscale, but acquiring evidence that confirms the results, is difficult. Micro- and nano-cantilever resonators seem to be a promising candidate for the performance of sensitive measurements, since they have the potential to derive many properties from an added material at once by analysing the dynamic behaviour of the system [20]. Malvar *et al.* [9] have shown that by looking at the first two resonance frequencies of a nanocantilever it is possible to find mass and stiffness simultaneously. However, from continuum theory it is known that a cantilever beam has many frequencies and that the effect of deposited material may have a larger influence on other modes of vibration. It has been shown that higher flexural modes result in a larger mass sensitivity for addition of uniform layers [21]. Additionally, by combining multiple mode shapes, a more accurate approximation on the location of the added material can be obtained [22]. However, less is known about the usage of higher modes on measurements on both mass and stiffness. Are specific deposition locations needed to decouple the counteracting mass and stiffness effect [23] or will a consistent identification of both properties be obtained by looking at multiple resonant frequencies simultaneously [24]?

The goal of this project is to exploit the contribution of flexural higher modes on the determination of mass and stiffness properties of a polymeric material on a microcantilever. A microcantilever is used since many factors affect the response of a cantilever at the nanoscale. The fabrication process entails uncertainties for example. Furthermore, the identification of mass and stiffness is, in this thesis, restricted to polymeric materials deposited on cantilevers. Cells are complex systems with viscoelastic properties. Their skeleton is a polymer network that shapes the cell and provides its mechanical rigidity [6]. Compared to real cells, polymers are less complex. Moreover, they mimic biological matter very well.

The state-of-the-art for mass and stiffness measurements is introduced via a thorough literature study in Chapter 1. Chapter 2 elaborates on the different methods for the addition of material. Moreover, it introduces

a setup for the multi-modal analysis and presents a theoretical model for the decoupling of mass and stiffness. The third chapter of the present study shows the obtained results. The experimental results are linked to a theoretical model such that mass and stiffness properties can be extracted simultaneously by minimizing the error between the theoretical and experimental frequencies in the presence of the polymer sample. Both the experimentally and theoretically obtained results will be discussed in Chapter 4. Subsequently, the report concludes in Chapter 5 by giving a brief review on the main findings. During the research process, much knowledge is gained and the outcomes entail new interesting questions. The relevant recommendations are given in Chapter 6. More detailed information is included in the Appendices.

Literature review

Much research is done on methods that are able to measure mechanical properties on a microscale. This literature study will focus on the techniques that are available nowadays to measure stiffness or mass, furthermore discuss the opportunities for the measurement both of stiffness and mass, subsequently elaborate on the theory behind this and finally propose an approach that will necessitate a thorough research for the identification of mass and stiffness using multi-modal vibration analysis.

1.1. Measurement methods

1.1.1. Stiffness measurement

The Young's Modulus is a measure of stiffness, which can be derived by means of multiple techniques. This section reflects on some of them.

Atomic Force Microscopy

First of all, the stiffness of materials can be determined through indentation. While indenting the surface of a material, force and displacement are continuously measured [25]. An atomic force microscope [AFM] [2] could be used for soft materials like cells. A standard AFM is presented in Figure 1.1. The method is based on bringing the AFM probe, which works as an indenter, close to the material surface. By then indenting the probe into the material surface and subsequently retracting it from the surface, a force-displacement curve is created. The Young's modulus is obtained by converting the force-displacement curve into a force-indentation curve and by fitting it with an analytical model like the Hertz model [26]. This model registers the indentation and the loading force, before predicting the contact area as a function of the loading force. It assumes an infinitely stiff, conical indenter and a soft, homogeneous, infinitely large sample. Therefore, this model is only appropriate as long as the indentation is smaller than the thickness of the sample [27].

One has to take into account that the material becomes considerably compressed by indenting it for the procurement of the force curve. When cells are investigated, they could be damaged by the tip. To check whether the process is non-destructive for the material, the probe should be moved to another spot on the material. If it shows the same behaviour, it can be concluded that the material has relaxed and fully recovered after obtaining a force curve. The compression is reversible and does not damage the material. If this is not the case, fine glass needles can be utilised instead of an AFM probe alternatively [27]. To decrease the risk of damage to the sample a lot, scanning acoustic microscopy could be an interesting option [28]. In such cases sound is used to investigate the material properties, instead of indenting a cell with a physical indenter.

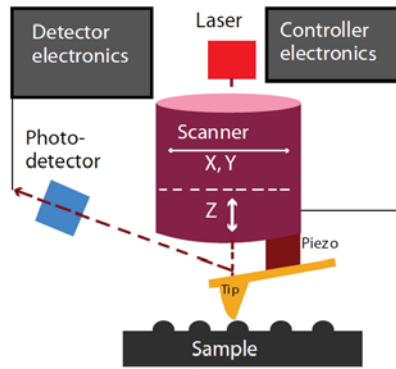


Figure 1.1: An AFM can be used for indentation or for deriving a map of the surface topology of a sample. The setup consists of a laser, a photodetector, a piezoelectric actuator, a cantilever with a sharp tip on the end and the necessary electronics. The actuator controls the displacement of the cantilever. When the tip comes close to the sample surface, the cantilever will bend due to forces between the tip and the sample. The deflection is detected via a laser and a photodetector. Such deflection can be combined with the spring constant of the cantilever in order to determine the experienced force. [3]

Magnetic twisting cytometry

A sample can be deformed through magnetic twisting cytometry as well. When a functionalised ferrimagnetic micro bead is attached to the membrane of the sample, it can be subjected to an oscillatory magnetic field. The resulting torque will cause a deformation of the sample. By optically tracking the oscillatory forcing and resulting bead motions, the elastic and frictional moduli can be computed. This method is presented in Figure 1.2.

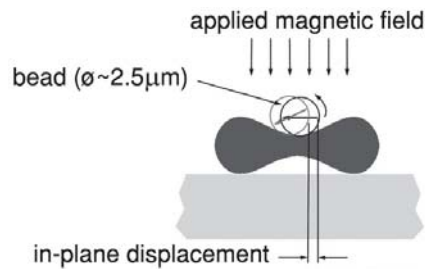


Figure 1.2: Optical magnetic twisting cytometry tests applied to a red blood cell. An applied magnetic field, normal to the magnetization of the bead, generates a torque on the bound bead. The resulting torque deforms the cell with the resultant rotating and translating bead. The in-plane displacement of the bead is tracked optically. [4]

Optical tweezers

When multiple micro-sized particles are strategically bound to the surface of a sample, they can be trapped with optical tweezers [5]. A parallel beam is connected to an upright or inverted optical microscope. The objective lens of the microscope is utilized to obtain a tightly focussed laser beam. When this beam passes through a high-refractive-index dielectric medium, the photons emitted from the laser beam undergo a change in momentum. In other words, micro-sized particles need to have a refractive index that is greater than that of the surrounding medium. Subsequently, a force is exerted on a micro-particle that pushes it towards the focal point of the laser beam. The micro-particle then becomes trapped. The beads act like handles and the sample can be stretched by sticking one bead to the surface and moving another bead with the optical tweezers [3]. Figure 1.3 gives an overview of this method when it is applied to a human red blood cell. A force ranging from tens to hundreds of pN (10^{-12} N) can be applied for the deformation of the cell. A three-dimensional computational model is used to extract the elastic and viscoelastic properties of the cell membrane from the cell deformation.

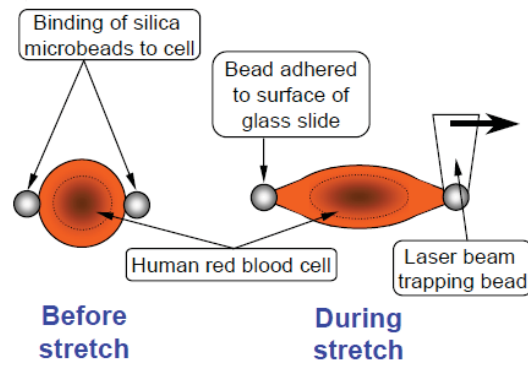


Figure 1.3: Schematic explanation of how a cell is stretched by optical tweezers [5]. Human red blood cells have been directly stretched using optical traps to maximum forces of 60 pN by recourse to two or three bead attachments on cell surfaces.

Microfluidic optical stretcher

Lasers are also used in a method called microfluidic optical stretcher. This method (see Figure 1.4) utilises two counterpropagating divergent laser beams, coaxially aligned, which induce optical forces. These forces provide a stable trapping situation because they balance each other exactly in the middle of the light sources. A trapped sample can be deformed by them as well. The strength of the sample can be determined by tracking the optical deformability which corresponds to the compliance after a certain time [6].

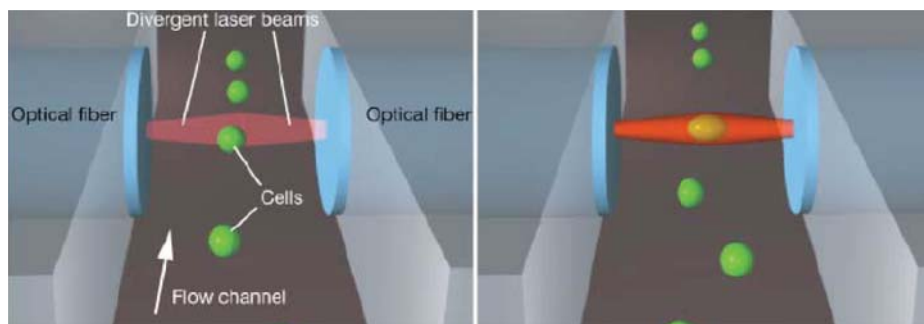


Figure 1.4: Cells flow through a microfluidic channel. When trapped by two counterpropagating divergent laser beams, the cell deforms as a result of the induced surface force created by the laser beams. The technique is called microfluidic optical stretching. [6]

Micropipette aspiration

Another way to determine the stiffness of a sample can be done by using micropipette aspiration. This technique uses micropipette suction to draw the sample into a glass tube, while the aspiration pressure and the leading edge of the sample surface are tracked [29]. The extent of the deformation is controlled by the stepwise increase in the aspiration pressure and the chosen inner diameter of the glass tube. A stepwise increase is important, because the sample needs to find a new equilibrium after the increase in pressure has occurred. The deformation is tracked with an optical microscope. A resolution in the order of pN for the force and nm (10^{-9} m) for the displacement can be monitored [5]. In order to obtain the elastic and viscous properties of a sample, basic continuum models are used [29]. When analysing a cell for example, the most popular models assume that the cell is a homogeneous elastic solid or that it is surrounded by an elastic cortical shell.

Microfluidic channel flow assays rely on the same principle [30]. A natural pressure difference enables samples to pass through channels that are produced by means of photolithographic techniques.

Micropores filtration

Another technique based on the deformability of cells is micropores filtration [31]. With this technique, samples are artificially pushed through a filter. The required peak pressure can be used as an index of deformability. The size of the micropores in the filter influence the peak pressure and determine the precision of this method. The size of the pores needs to be adjusted to the size of the investigated sample. Instead of a two-dimensional structure, three-dimensional structures can be used as a filter as well [32]. Biological cells are

able to interact with the cage-like structures. Normal and malignant cells can be distinguished via the ability to enter these constructions.

Electrostatic pull-in instability

A different way to measure stiffness could be by interpreting it through quasistatic electrostatic pull-in instability[33]. A cantilever and a substrate combined, work like a capacitor when applying a driving voltage between the two. A critical electric potential will be reached when the driving voltage is increased. At that moment, the cantilever will snap towards the substrate. The pull-in voltage is affected by the geometry and stiffness of the cantilever, and the interaction between the substrate and the beam due to the electrostatic load.

1.1.2. Mass measurement

There are well-established techniques for determining mass. This section will elaborate on the currently most common methods.

Mass spectrometry

For the identification of substances in a material sample, mass spectrometry is widely used. The system is presented in Figure 1.5 [7]. By ionizing a sample, accelerating the ions and directing them through a magnetic or electric field, the sample's particles will deflect. The amount of deflection depends on the mass of the particle. By correlating known masses to the sample masses, the atoms or molecules can be identified. Mass spectrometry facilitates the mass-to-charge ratio measurement of molecular species, but is not able to perform a measurement on nanostructures and biological assemblies [34].

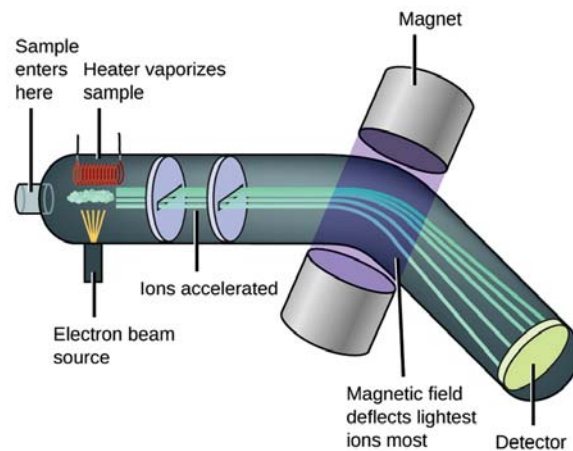


Figure 1.5: Mass spectrometry enables mass-to-charge ratio measurements of molecular species. A sample is ionized by bombarding it with electrons. During this process molecules can break into charged fragments. The ions are accelerated and are subjected to a magnetic field. The field forces the ions to deflect. Ions with the same mass-to-charge ratio will undergo the same amount of deflection. A detector is able to detect the ions. By correlating known masses to the sample masses, the atoms or molecules can be identified. The relative number of ions generated is plotted against their mass-to-charge ratio. This mass spectrum can be compared to characteristic fragmentation patterns for identification purposes as well.

Nano- and micro-mechanical resonators

Previous research has been done on the measuring of mass using nanomechanical resonators. The most common configuration is a cantilever resonator - a beam clamped at one end, which is actuated at its first flexural mode [35]. At a resonant mode, the shape of the vibration is known and the energy is fully commuted between the kinetic and potential state which results in an unstable system. This phenomenon occurs at the resonance frequency. Since this frequency of a system is a sensitive function of its mass, the eigenfrequency changes when material is added. Added mass affects the kinetic energy level, thus resulting in a decrease in the resonance frequency. An advantage of such a system is that the set-up can be easily scaled down to increase the sensitivity. As a result, minuscule added masses can be sensed [36]. However, a counteracting effect is caused by the stiffness of the added material [37]. This affects the potential energy which means that

the eigenfrequency will increase. Theoretical models often neglect the added stiffness because the effect can be easily hidden by the mass effect when the adhesive is positioned at the tip of a cantilever. However, when ignoring the effect of the added stiffness, this can lead to a significant underestimation of the mass depending on its location [38].

Micro- and nano-cantilever resonators seem to be a promising candidate for the performance of sensitive measurements, since the resonance frequency is affected by mass and stiffness. Is it possible to disentangle mass from stiffness by using vibrations to measure both properties at the same time? One equation with two unknowns cannot be solved. Extra information is needed to decouple the mechanical properties. The state-of-the-art of the disentanglement of mass and stiffness using micro- and nanomechanical systems will be examined in the following section.

1.1.3. Micro- and nanomechanical systems - State-of-the-art

The operation modes of nanomechanical resonators are defined in terms of a static and a dynamic mode. The difference is that the beam is excited in the dynamic mode and not in the static mode. The advantages of both modes will be discussed in the following subsections.

Static mode

Previous research states that both the location of the adsorbate and an adsorption induced change in surface stress and stiffness influences the behaviour of a cantilever [39]. The investigation of this impact can be done in the static mode. A distortion in the cantilever's profile arises when adding a substance. This is due to gravitational forces and the adsorption of molecules. The local change in the cantilever curvature designates the location and spread of the adhesive, but can be used to obtain the difference in surface stress before and after the deposition of material as well since the cantilever has a free end to allow deformation or bending to relieve the stress [38]. When material is added to one side of a cantilever, the asymmetry of the system causes extra surface stresses. Charge reorganization and intermolecular forces affect the stresses likewise [40]. The molecular interaction between a cantilever and biomolecules can cause a cantilever to bend upwards. This is shown in Figure 1.6. An optical scanning method combines the optical beam deflection technique with an automated two-dimensional scanning of a single laser beam by voice-coil actuators. By directing the laser beam on the cantilever and arranging a two-dimensional linear position detector to collect the reflected beams, a change in the local curvature of the cantilever surface becomes visible due to the displacement of the reflected laser beam spot on the detector [41].

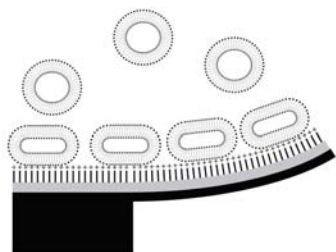


Figure 1.6: Interaction forces between the cantilever and biomolecules can cause the cantilever to bend upwards. [8] In the research a pre-functionalized cantilever was used to investigate nanomechanical changes at the interface when binding with lipid vesicle.

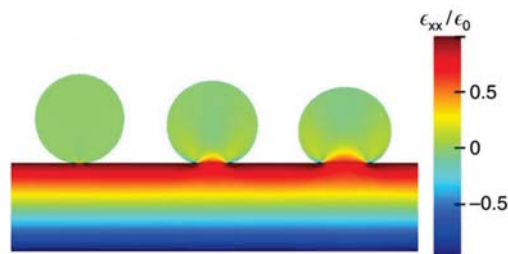


Figure 1.7: This pictures is derived from a FEM simulation by Malvar *et al.* [9] to investigate the effect of the contact area on the mechanical coupling between the adsorbate and the cantilever. The larger the contact area, the higher the effect on the mechanical coupling will be.

It has to be taken into account that the contact area of the adsorbent and the cantilever's surface plays an important role. When a material is laying on the cantilever but is not adhered to it, there will be no extra resistance to stretching: no stiffness effect will occur. This is visualised in Figure 1.7.

The effect of surface stress on the natural frequencies of a cantilever are investigated in a preceding analysis [42]. It states that the surface-bulk ratio is an important factor whether the surface stress is negligible or not. The usage of a cantilever with a thickness in the nanometre range shall be affected more than a beam that has a thickness in the micrometer range. This will result in a respectively large or negligible shift in the resonance frequency. Other research is done on a variety of thickness for the added material as well [37, 43]. Zhang *et al.* state that for small ratio's between the adsorbate and cantilever thickness, the mass effect dominates. Sadeghian *et al.* [10] stated that this thickness ratio is affected by the density ratio of the

used materials. The two graphs of Figure 1.8 both show a nonlinear decrease of shift in resonance frequency at the start, which depicts the mass effect. Subsequently the graphs become horizontal. This indicates an equal mass and stiffness effect. Thereafter, the slope increases, pointing out that the influence of the added stiffness overshadows that of the mass. The thickness ratios where these turning points occur are different for the two used materials.

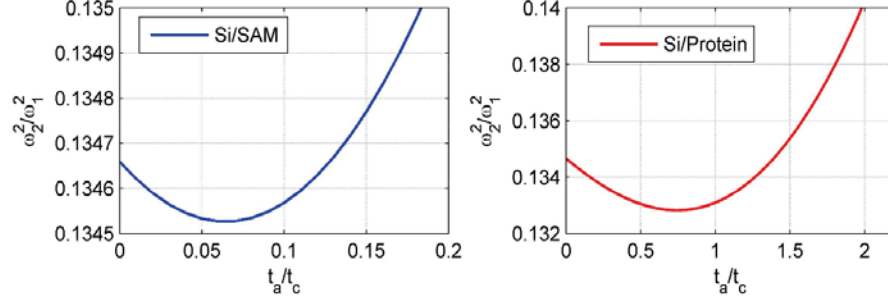


Figure 1.8: The relative eigenfrequency shift is plotted against the ratio between the thickness of a uniformly adsorbed layer and a cantilever [10]. The symbol ω_1 represents the first resonance frequency of a cantilever and ω_2 depicts the resonance frequency after deposition of the layer. Silicon [Si] has a density of 2330 kg m^{-3} and a Young's modulus of 169 GPa. The self-assembled monolayer from the left blue graph has a density of 675 kg m^{-3} and a Young's modulus of 12.9 GPa. The right red graph has a myosin monolayer with a density of 183 kg m^{-3} and a Young's modulus of 0.7 GPa.

Dynamic mode

By using the dynamic mode, information about the mass, stiffness, location or mass distribution can be obtained. This subsection will elaborate on different approaches found in literature.

Determination of mass

Added mass affects the kinetic energy level: when placing a substance at a point where the displacement is large, the mass effect is the largest. The largest displacement is obtained at the tip of the cantilever when observing the first flexural mode. By looking at the shift of the first resonance frequency, the added mass can be obtained [35]. The relation between these two variables is described via the following equation:

$$\Delta m = \frac{k}{4\pi^2} \left(\frac{1}{f'^2} - \frac{1}{f_0^2} \right) \quad (1.1)$$

In case of a uniform deposition layer of material on a cantilever, the resonance frequency can be derived by,

$$\frac{\Delta f_n}{f_{0n}} \approx -\frac{1}{2} \frac{m_{\text{adhesive}}}{m_{\text{beam}}} \quad (1.2)$$

Former research is done on the use of higher modes. By investigating the addition of a uniform gold layer on the upper side of a cantilever, it was found that the sensitivity (ratio of frequency shift to unit mass loaded) increases by using higher modes [21]. A comparable study was performed Dohn *et al.*[44]: Instead of using a uniform gold layer, a single gold bead was positioned on a cantilever. Experiments up to excitation of the fourth mode resulted in an increased mass sensitivity for higher modes compared to the fundamental bending mode.

Sharos *et al.* [45] investigated the usage of torsional and lateral modes of cantilevers instead of the flexural modes. By placing a mass as far as possible from the centreline near the tip of a cantilever, the first torsional and lateral modes are affected more, in contrast to the first vertical bending mode. Furthermore, because of this addition, an asymmetric geometry arises. It can cause uncoupled closely positioned resonance frequencies to couple heavily: this phenomenon is called mode veering [46]. Higher flexural modes can be more sensitive to added mass due to the higher natural frequency and because of veering with a torsional mode. Nonetheless, it could be hard to determine the exact frequencies of the modes individually when coupling occurs.

Determination of stiffness

Nanomechanical resonators were used as mass sensors until around the year 2006. It was then that a positive shift in resonance frequency was found. The location of the deposition of soft materials seemed to locally affect the flexural rigidity of the cantilever [47]. The added stiffness influences the potential energy of the system. The adsorption induced change in surface stress and added stiffness affect the effective stiffness of the system. Hence, the increase of resonant frequency becomes significant at locations where curvature arises during bending. When investigating the shift in resonance frequency for the first flexural mode for example, the adhesive should be located near the clamping [37].

Mass and stiffness

Ramos *et al.* [47] changed the adsorption position to decouple the effects of stiffness and mass. The added mass was determined with a deposition location near the free end and the added stiffness was quantified with an adhesive position near the base. To illustrate the counter effect of mass and stiffness, Figure 1.9 shows the mass and stiffness effect based on the location of deposited material. Consequently, the flexural rigidity D in the equation for the eigenfrequency of a cantilever shown in Equation 1.3 [38] depends on the position " x ".

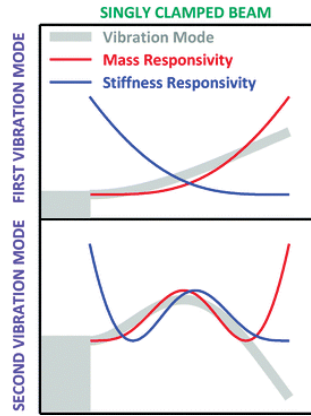


Figure 1.9: The two pictures show the relation of the mass and stiffness response with respect to the mode shape of a cantilever. It can be seen in the upper picture, representing the first bending mode, that the stiffness effect is high near the base while the mass effect overrules at the tip of the cantilever. The lower picture shows the effects for the second bending mode. It demonstrates that the mass and stiffness effect cancel each other out at the anti-node. [11]

$$\omega_n^2 = \frac{\int_0^L D(x) \frac{\partial^2 \psi_n(x)}{\partial x^2} (x) dx}{\rho_c W T_c \int_0^L \left(1 + \frac{\rho_a T_a(x)}{\rho_c T_c}\right) \psi_n^2(x) dx} \quad (1.3)$$

L denotes the length, W the width and T the thickness of the cantilever (subscript c) or adhesive (subscript a), ψ_n is the shape function per mode n and x is the location along the length of the beam. Moreover, the bending rigidity can be obtained as [38]:

$$D(x) = \frac{W}{12} \frac{E_c^2 T_c^4 + E_a^2 T_a^4(x) + 2E_c E_a T_c T_a(x)(2T_c^2 + 2T_a^2(x) + 3T_c T_a(x))}{E_c T_c + E_a T_a(x)} \quad (1.4)$$

Furthermore, research has shown that the shape of the vibration mode affects the shift in frequencies differently at specific regions [23]. Ramos *et al.* state that different locations need to be used for the disentanglement of mass and stiffness properties of the added material: At anti-nodes or at the tip of a cantilever for obtaining the mass. Conversely, at nodes or near the base of the beam for the derivation of stiffness. They state that the stiffness overshadows the mass effect on nodes, while no positive frequency shift was obtained at any node up to the third flexural mode. The mass effect is minimized due to the small vibration amplitude around the node and it is not proven that the stiffness effect is larger than the mass effect.

As mentioned before, the sensitivity of the system will increase on a smaller scale. Horizontal silicon nanowires¹ [48] have the potential to be ultrasensitive in mass sensing and stiffness spectrometry. Perfectly

¹A nanowire is a nanostructure that has a diameter in the nanometre range, or a length-to-width ratio that is larger than 1000.

shaped nanowires theoretically vibrate at the same frequency in all planes in flexural vibration. A small imperfection in the cross-sections in the wire affect this tendency. As a result, the single vibrational resonance peak breaks up into two closely spaced peaks with a similar amplitude. The imperfection-induced peaks correspond to vibrations in orthogonal directions. This splitting of the resonance frequency gives rise to the decoupling of the mass and stiffness properties of the system. Only two different driving frequencies are used within this method. A limitation is caused by the boundary condition that the cross-section and thickness has to be much smaller than the thickness and cross-section of the nanowire itself. Furthermore, the asymmetry factor has to be small. The nanowires that are used in this experiment, were created via the vapour-liquid-solid [VLS] technique. This method combines chemical vapour deposition² with a catalytic liquid alloy phase which speeds up the growth process. Silicon nanowires with a diameter of 100 to 300 nm are produced via the VLS method [49]. There will always be some imperfections in the initial situation, entailing asymmetry.

Another method for the disentangling of the mass and stiffness properties is proposed by investigating the quality factor [Q-factor] [50]. The Q-factor depends on the frequency, the width of the cantilever and the viscosity and density of the surrounding medium. The resonance frequency of the system is affected by the mass and the stiffness, but the study states that the Q-factor is only influenced by the mass of an adsorbate. On the basis of this assumption, the determining of the mechanical properties is facilitated. This method sounds promising, but how the Q-factor is used raises questions. First of all, the Q-factor is a sensitive parameter. Consequently the variation within the results for two modes in air and three modes in water, is great ($\pm 12.5\%$). This affects the accuracy and the sensitivity of the analysis. Furthermore, the Q-factor is not only depending on mass. The resonance frequency and thus the added stiffness affects this parameter as well. This is shown in the following equations:

$$Q = \frac{1}{2\zeta}$$

$$\zeta = \frac{c}{2\sqrt{km}}$$
(1.5)

An array of dual nanomechanical resonators [51] is proposed in a different study to further improve the quality of the specificity. By measuring the frequency shift of the beams for two modes and a deposition of material near the free or clamped end of the cantilever, the mass and stiffness effects are both inspected. Due to the use of a relatively thinner cantilever (100 nm), the sensitivity of the cantilever near the free end is limited, while a higher sensitivity and a greater selectivity is obtained near the clamping. By using an array of cantilevers as described in the method, there could be a chance that coupling occurs between the cantilevers. This could affect the results and thus cause less accuracy compared to the use of beams separately. The used cantilevers are in the micro-regime (400 x 100 x 1.0 μm , first mode at 300 kHz) wherefore the coupling effect could be small. By way of contrast other research [52] has used the coupling effect in order to determine masses of ~ 17 pg. Their cantilevers were 16 times smaller (25 x 10 x 0.1 μm , first mode at 133 kHz). This sensing method is based on the difference in amplitude of the peaks on resonance frequencies. The advantage of the usage of an array of dual nanomechanical resonators is that larger datasets can be obtained at once.

Mass and position

When obtaining a larger mass sensitivity by introducing higher bending modes, Dohn *et al.* introduced the localization of added material by measuring multiple modes [12]. When a particle is placed on a node, its mass and stiffness contribution will be equal to zero. Controversially, if the material is added on an anti-node, the influence of the mass and stiffness on the resonance frequency will be maximum. More nodes and anti-nodes occur at higher flexural modes. Combining multiple modes can therefore approximate the position of a particle (see Figure 1.10). The result will become more accurate when obtaining more modes [22].

This approach was expanded by the determining of the locations of multiple particles [22]. The equation for kinetic energy is made dependent on a population P of particles with mass Δm_p and M_p particles at position $z_{\Delta m_p}$. Small particles are used and therefore it is assumed that they do not affect the mode shape of the cantilever. As a result, the strain energy is taken to be zero. A minimization method is used to optimize the locations. Since the point-like gold particles are non-compliant, the measurements are robust. Hanay *et al.* measured mass and position of particles by adding them separately (one by one) on a resonator and measuring the frequency shift for four modes real-time [53] to validate the method, they subsequently performed

²Chemical Vapour Deposition [CVD] is a fabrication technique which exposes a substrate to one or more gaseous volatile precursors. These vapours react and/or decompose on the surface of the substrate. In this way, a desired deposit is produced.

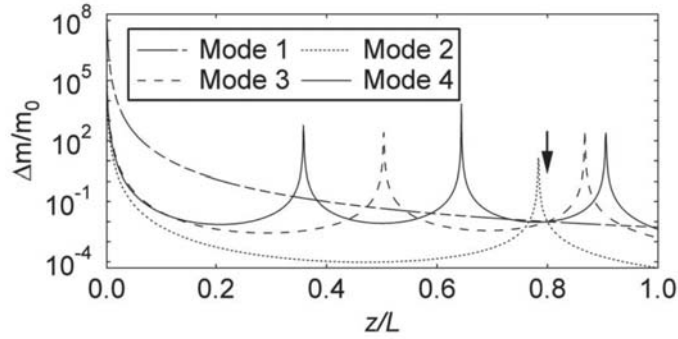


Figure 1.10: The location of an attached particle can be obtained by using a graph shown in this figure [12]. The mass ratio ($\Delta m/m_0$) is plotted against the position of a particle for all possible locations along a cantilever (z/L). The resulting graphs are different per mode but they intersect at a specific point. The location corresponds to the real position of the particle and its mass. In this situation, the intersection is found at $z/L=0.8$ and $\Delta m/m_0 \approx 10^{-2}$ and is highlighted with an arrow.

similar measurements using liquid micro-droplets instead [20]. The results were comparable.

Mass and geometric data

The inertial mass, position, size and shape of adsorbates are obtained from experimentally and numerically derived results from downward frequency shifts of multiple modes [20]. In this case, the shift of the resonance frequency enables the determination of the added mass like described before. The position is derived from the maximum or minimum change in the resonance frequencies. When adding mass at a node of a mode shape, the shift is minimum. Conversely when adding mass at an anti-node, the shift will be maximum. The shape and size of added material is investigated using the skewness and difference of higher mode peaks for a doubly clamped beam (first, second, fourth and tenth mode).

Bending modes contain nodes and anti-nodes. Similarly do the torsional mode shapes. By combining the two type of nodes for the monitoring of frequency changes, more parameters of the added material could be derived [54]. When a particle is situated at a nodal point of a flexural mode, a shift in resonance frequency could still occur due to rotational effects. This gives insight in the centre of mass and rotational inertia properties (size, shape, mass distribution and orientation) of the added material. If a particle is positioned at a nodal point of a torsional mode shape, a change in the frequency spectrum is provoked by translation inertia properties only.

1.2. Theoretical model

As depicted in the previous section, added material changes the dynamic behaviour of a cantilever. It results in a shift in resonance frequency which relates to both mass and stiffness of the adsorbate. The added mass induces a positive effect on the resonance frequencies, but the added stiffness a negative effect. These counteracting effects can be disentangled when combining experimental methods for a multi-modal vibration analysis with an inverse problem of the theory³. The sensitivity and range vary through the cantilever properties, the surrounding medium, the distribution of the added mass and the accuracy of the theoretical method. This section will elaborate on some different analytical methods to analyse the dynamic response of a microcantilever beam.

1.2.1. Analytical model

The Euler-Bernoulli beam theory [55] is often used to model a beam. It is based on the equilibrium of forces that act on an infinitesimal piece of the beam and assumes the usage of a linear material and small deflections ($u(x, t)$). The assumption is plausible when the cantilever is a slender beam, which is the case when the ratio between the length and the thickness of the cantilever ($\frac{\text{length}}{\text{thickness}}$) is large enough. The rotational inertia and the shear deformation are neglected. Furthermore, the inextensionality theory is applied. This principle states that the length of a beam does not change when bending. The displacements of the beam in x -direction are equal to zero and the displacements in y -direction are dependent on the location within the system.

³Instead of obtaining natural frequencies from the mass and stiffness of a cantilever, the mass and stiffness have to be obtained from experimentally derived resonance frequencies.

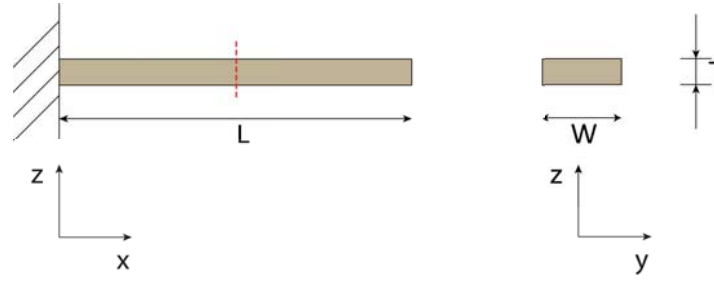


Figure 1.11: A side view of a solid cantilever is shown on the left-hand side of the figure. The right-hand side of the figure presents a mid-section of the cantilever.

The potential and kinetic energy of an Euler-Bernoulli cantilever can be obtained as follows, respectively:

$$V = \frac{1}{2}EI \int_0^L \left(\frac{\partial^2 u}{\partial x^2}\right)^2 dx \quad (1.6)$$

$$T = \frac{1}{2}\rho A \int_0^L \left(\frac{\partial u}{\partial t}\right)^2 dx \quad (1.7)$$

E represents the Young's modulus and ρ is the density of the material. The moment of inertia is I . The dimensions of the beam are described via L being the length of the cantilever and A the cross-sectional area. $u(x, t)$ is the displacement function of the beam.

By using Hamilton's principle [56] it can be shown that the equation of motion of the Euler-Bernoulli beam is:

$$\rho A \frac{\partial^2 u(x, t)}{\partial t^2} + EI \frac{\partial^4 u(x, t)}{\partial x^4} = 0 \quad (1.8)$$

A Timoshenko model [57] could be used as well, particularly when shear deformation and rotary inertia have to be considered. Another method could be to model the cantilever with adhesive as a lumped parameter system [58].

Rayleigh's method

Rayleigh's method [55] is able to find fundamental eigenfrequencies at the point where the maximum potential and maximum kinetic energy are equal. It is a common used approximation method [37, 38, 47]. The potential energy (V) of a cantilever of length L due to bending is described by Equation 1.6. The kinetic energy (T) is formulated as Equation 1.7. As depicted in Appendix C, for an Euler-Bernoulli beam the solution of the equation of motion is position and time dependent:

$$u(x, t) = \sum_{n=1}^{\infty} \psi_n(x) \cos(\omega t) \quad (1.9)$$

When substituting this formula in equations 1.6 and 1.7, and finding their maximum, subsequently the eigenfrequencies can be determined via the following equation:

$$\omega^2 = \frac{V(\psi(x, y))}{T(\psi(x, y))} \quad (1.10)$$

This formula is known as the Rayleigh quotient. It can be used for specific eigenmodes. Rayleigh's method assumes the use of a conservative system. Therefore, energy losses are not considered. The more precise one can predict the bending mode shapes of a system, the higher the accuracy of the method will become. The shapes are mostly determined via displacement. In general, displacement based formulations are derived from the potential energy and therefore are approximated too stiff. As a result, the eigenfrequency founded by Rayleigh's quotient will be slightly higher compared to the exact eigenfrequency. (Conversely, stress based formulations are derived from complementary energy and therefore too compliant.)

1.3. Summary

Many methods for stiffness or mass measurements exist. Microcantilever resonators are a promising tool since they give rise to more information on the material properties. Research is done in many aspects and possibilities of these resonators. Combining multiple resonant modes enables the derivation of for example mass, position, volume and stiffness of an added material. It has been shown that higher modes (up to the fourth bending mode) result in a larger mass sensitivity. By combining multiple mode shapes a more accurate approximation on the location of the added material can be obtained. Less is known about the stiffness: Will a multi-modal vibration analysis lead to a higher sensitivity of mass and stiffness disentanglement as well?

To disentangle mass and stiffness, experimentally derived resonance frequencies need to be linked to theoretical models. Different models exist with their own assumptions and boundary conditions. For the decoupling, independent equations for different modes are solved. On the macroscale, Amabili *et al.* [24] were able to extract tensile force and stiffness in tie-rods from ancient monumental masonry buildings by looking at four to six resonant frequencies simultaneously. The method shows a consistent identification of the tensile force where the use of three or four modes is already rather exact. It would be interesting to investigate whether a system on the micro and nanoscale has a comparable dynamic behaviour.

1.4. Research Question

Throughout the literature review it has become apparent that not much is known yet about the effect of higher modes on the mass and stiffness sensitivity of a cantilever beam. On the micro- and nanoscale it has been shown that the use of higher modes lead to a larger mass sensitivity, but the mass could be overestimated when stiffness is not taken into account. Therefore, the research question of this Master's thesis becomes:

- What is the effect of using multiple modes simultaneously for the decoupling of mass and stiffness, via a multi-modal analysis of a clamped-free micro-cantilever?

The dynamic response of the cantilever needs to be examined before and after the deposition of material. The sub-questions that are entailed by the proposed research question are:

- In what way can a material with known mass and stiffness properties be positioned on a microcantilever?
- Which method can be used to perform a multi-modal vibration analysis on a microcantilever?
- What theoretical model should be used for an inverse method in order to decouple mass and stiffness?
- Does the accuracy of the approximation of added mass and stiffness relate to the amount of modes that are used?

The following two chapters will elaborate on the experimental and theoretical methods of this approach respectively.

2

Approach: Experiment and theory

This chapter elaborates on the procedure of this research. Different methods for each step of the process will be proposed. The complete approach is explained in the schematic in Figure 2.1, which matches with the following listed procedure:

1. Select a bare cantilever
2. Measure the dimensions of this beam (Section 2.1)
3. Perform a multi-modal analysis (Section 2.3)
4. Deposit material (Section 2.2)
5. Perform a multi-modal analysis
6. Measure the dimensions of the added material
7. Insert the experimental results in a theoretical model (Section 2.5)
8. Run the model
9. Derive the mass and stiffness of the added material

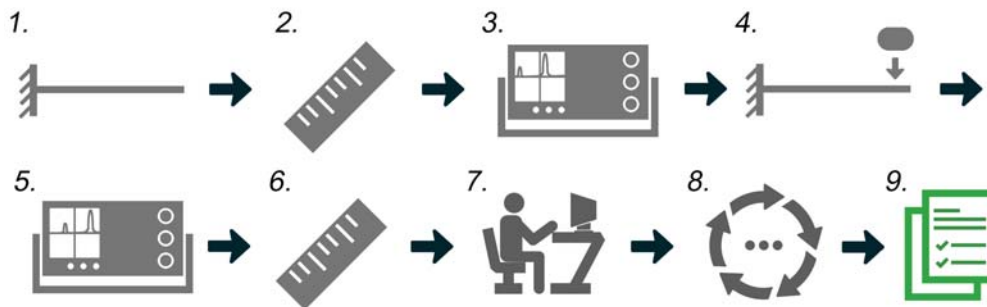


Figure 2.1: This image shows the coarse process steps of the method. Initially, a cantilever has to be selected. The resonance response has to be measured. Subsequently, a material needs to be deposited on the cantilever. The frequency response of this system has to be obtained as well. Both frequency spectra have to be evaluated by a computational model. eventually the mass and stiffness properties of the added material should be the final result.

2.1. Experiment: Cantilever dimensions

Since the dimensions of each cantilever vary slightly, they need to be obtained accurately. This can be done with a scanning electron microscope [SEM] (JEOL JSM-6010LA). The SEM [3] employs fast-moving electrons to image a sample, whereas ordinary optical microscopes make use of visible light. The resolving wavelength of electrons used in an ordinary SEM is $\sim 1\text{nm}$ while the wavelength of visible light is in the range of 400 to 700nm , consequently the resolution of an SEM is much better. Figure 2.2 shows the working principle of an SEM.

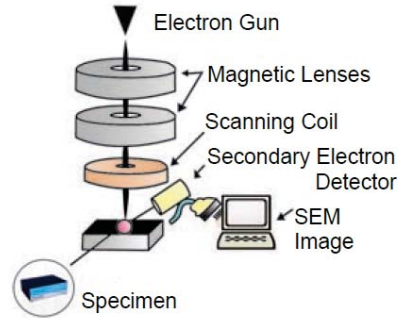


Figure 2.2: The main components of a scanning electron microscope [SEM] are shown in this schematic drawing. The electron gun produces the electrons which are subsequently accelerated by a high electric potential. The magnetic lenses ensure the focus of the beam on the specimen. The scanning coil enables the scanning over the sample surface. Electrons from the beam that collide with electrons in the object are knocked out of their usual orbits. These secondary electrons can be traced with detectors that are placed in the sample chamber. Images are generated depending on the contrast in the magnitude of the signals obtained while scanning. The whole process takes place in vacuum since air molecules can cause the electrons to scatter. This would affect the quality of the picture. [3]

An SEM works within a vacuum environment since electrons can interfere with molecules in air. This will lead directly to a lower quality of the picture from a sample. When investigating a non-conductive material with an SEM, electrons will interact with the sample. The sample will get charged. When operating with voltages around one kV and a short working distance¹, a non-conductive sample will be visible. Nevertheless, the quality will be affected. One way to terminate this problem is by adding a conductive layer over the sample. This can be done with a sputter coater (SC7620, Emitech). An Argon gas flow (Zero Grade: 99.999%) is used as sputtering gas to eject material from the solid gold/palladium (Au/Pd) target (80/20%). Electrical power adds energy to the Argon particles to excite them to a higher energy state. The plasma that arises is used to bombard the target. Ions with an energy larger than the surface binding energy are able to eject atoms from the target and land on the sample. It is possible to add a sputtered layer of for instance gold, silver, gold/palladium or copper. Figure 2.3 shows the relation between the settings for the plasma current and the thickness of the sputter layer in time.

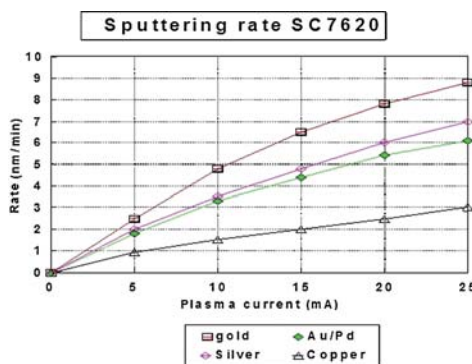


Figure 2.3: This graph shows the sputter rate as a function of the plasma current for different targets.[13]

¹The working distance is the distance between the objective and the sample

When analysing biological materials, the deposition of a conductive layer with a sputter coater can be inconvenient. Samples can be air dried to enable their investigation, but this could lead to shrinkage of the sample. An environmental SEM is an often used method which allows a lower vacuum environment in the specimen chamber. Saturated water vapour conditions makes examination of biological samples possible. Alternatively, liquid substitution could be used to allow inspection. Water is replaced with a liquid that has a low rate of evaporation under high vacuum such that the use of an SEM is possible. [59]

2.2. Experiment: Deposition of material

As mentioned in the introduction of Chapter 1, the tests of this research could be the beginning of an interesting application in the biologic sector. *Escherichia coli* cells are used in previous research for mass and stiffness disentanglement with a microcantilever already [47]. The Young's modulus of this bacteria is 1.3 GPa. The skeleton of cells consist of polymers. Therefore, polymers have roughly similar material properties and could be a useful material to add to a cantilever for experiments. In fact, different polymers are combined with real cells by for example using them as scaffold material in tissue engineering; poly(vinyl alcohol) [PVA] is used to form hydrogels [60], for example.

A controlled deposition of material is essential for this research. It is challenging to perform this at the microscale. Widely used additive manufacturing [AM] methods are selective laser sintering [SLS] and fused deposition modelling [FDM]. These methods do not have the accuracy that is needed to add the small masses that are desired in this research. Since the cantilever on the chip is fragile, direct-write techniques are more adequate compared to traditional AM processes. Direct-write methods are more promising and can be divided into four groups: dispensing, flow-based, particle beam and laser techniques [61]. In literature, an often used dispensing method is dipping; a cantilever is dipped in a suspension [62]. The ink-jet technique [47, 63] is a regularly used flow-based method. This procedure uses a pulse voltage to drive a piezoelectric transducer. It causes a pressure pulse which results in a droplet being forced through the nozzle. The volume is adjustable since the amount of droplets can be controlled. Malvar *et al.* use a different technique called electrospray ionization [ESI] [9]. This method can be classified as a particle beam method. A nanoparticle solution is guided by ion optics through three chambers with decreasing pressure. In the first chamber, an aerosol is created under high voltage. In other words, fine liquid droplets with nanoparticles in it are directed to the second chamber. Subsequently, the solvent of the particles evaporate due to a high temperature. The droplets become smaller and therefore get highly charged. Finally, the droplet separates from the ions, leaving a stream of nanoparticles directed to the sample.

Laser-based additive micro fabrication enables the addition of material on the micro- nanoscale. A laser beam is able to polymerize photoresist that is sensitive to UV light locally. By using two-photon polymerization² a high accuracy can be accomplished. This method is utilized in former research [64] to fabricate probes on microcantilevers for the use of atomic force microscopy.

This section will elaborate on techniques that are available in the department of Precision and Microsystems Engineering within the faculty of Mechanical, Maritime and Materials Engineering of Delft University of Technology: dipping, ink-jetting and two-photon direct laser writing.

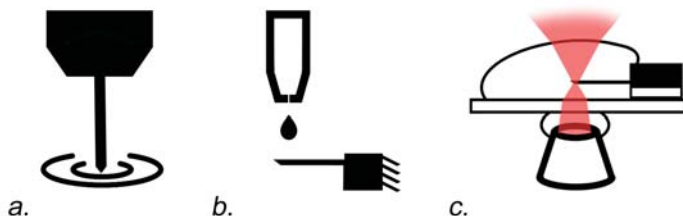


Figure 2.4: The three investigated deposition methods are dipping (a.), the ink-jet technique (b.) and 3-D direct laser writing (c.).

²Two-photon polymerization is explained in section 2.2.3.

2.2.1. Dipping

Dipping is a fast and easy deposition method. Ilic *et al.* [62] have immersed cantilevers with an immobilized antibody layer on the surface into a solution of antibodies. Cells were able to attach to the surface. Loose cells were removed by rinsing the samples with deionized water and dried with nitrogen. Since the cells that were bounded on the surface of the beams were distributed randomly, it is difficult to link the experiments to a theoretical model. Moreover, a known volume should be added. This can be achieved by acquiring a small droplet of a solution using an arbitrary cantilever chip and depositing it on top of the beam that will be investigated for this research. Consequently, multiple deposition locations can be investigated and it will be easier to determine the added volume.

First, experiments are performed with a micro-manipulator (MiBot BT-14, Imina technologies). This mobile micro-robot has a holder in which an arbitrary cantilever chip is mounted. By melting perforated laboratory film (Bemis, parafilm "M") on a microscope slide (VWR, Super Premium Microscope Slides, BS 7011), a droplet with a large contact angle could be obtained. The arbitrary cantilever is penetrated into this droplet with the MiBot.

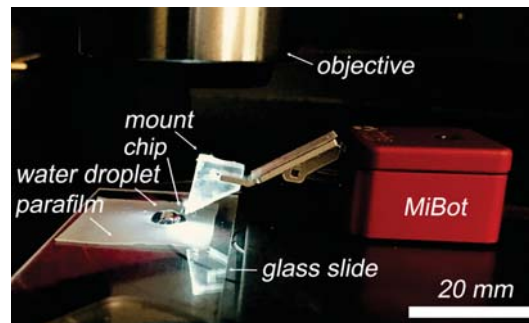


Figure 2.5: This photograph shows the setup for dipping. A 3-D printed head is mounted on the arm of the MiBot. A chip with cantilever is attached to the mount with glue. Using the MiBot underneath a microscope, enables a clear view on the process via a computer screen.

2.2.2. Ink-jet technique

In literature, an often used method for the deposition of material on microcantilevers is the ink-jet technique [47]. The device that is able to work with this technology in high precision and with different materials is expensive (around €50,000, =; supplier Microdrop Technologies [63]). In this section, the use of desktop printers and a controllable separate nozzle are investigated. The nozzles of the ink-jet printer are around 25 μm and are able to create droplets with a diameter of 35 μm .

Desktop printer [Epson Stylus SX235W]

Mechanical Engineering Bachelor's students from Delft University of Technology have developed an ink-jet device based on an EPSON desktop ink-jet printer [Epson Stylus SX235W] [65]. When interchanging the ink cartridges with one containing other fluids, the principle is the same but the price tag (around €238, =) is much smaller than the machine from Microdrop Technologies. Would it be possible to print polymers as well?

Polystyrene beads with a diameter of 5 μm were used for initial investigations, but the nozzles got clogged (more information can be found in Appendix D). Besides particles, fluids can be printed as well. The viscosity of the material needs to be low enough to be pushed through the nozzles of the printhead to print. (Attention still has to be paid towards clogging!) When heating up a polymer, the viscosity gets lower. However, source material has to be chosen wisely such that it does not affect the material within the system. The cartridges of the printer are produced from plastic, which would melt as well when heating the product inside. Therefore, a polymer that is soluble could be an option. Alcohol, acetone, and water are often used solubles. Unfortunately, alcohol evaporates fast which could lead to a higher risk of clogging. Acetone is a good solvent for plastics volatile as well. This soluble is inconvenient to use since the cartridges and components of the nozzles are fabricated from plastics. Consequently, water remains as an interesting solvent for this research.

An example of a polymer that is soluble in water is Polyvinyl Alcohol [PVA]. This material can be dissolved in deionized water by heating it up to 70 °C. By using high flow rate filter paper for filtration, impurities can be removed [66]. PVA is already used to mimic tissue and muscles [67]. Another example is Poly(3,4-

ethylenedioxythiophene) Polystyrene Sulfonate [PEDOT:PSS]. PEDOT itself is not soluble in water, but the combination with PSS enables the molecule to bind with the water molecules. Other examples [68] are Polyacrylic acid [PAA], Polyacrylamide [PAM] and Polyethylene glycol [PEG]. PEDOT:PSS (Aldrich Chemistry, 1.3%wt dispersion in H₂O) was chosen to work with since a solution of it in water was available. The viscosity of water is lower than PEDOT:PSS. Therefore, the PEDOT:PSS (1.3%wt) was diluted with water (1 ml PEDOT:PSS (1.3%wt) : 8 mL H₂O).



Figure 2.6: The Epson Stylus SX235 desktop printer that is used for ink-jet based experiments.

Desktop printer with stepper motor

To enable a more accurate deposition of material, a different group of Bachelor's students had modified a newer version of an EPSON desktop printer [EPSON XP-235]. By adding a stepper motor to the platform underneath the printhead, the usage of an extra dimension was enabled. The exact print location could be obtained through printing a large droplet near a calibration scale. Subsequently adding the sample that has to be imprinted and take a photograph of this setup. The image is investigated in a self-written program [Drop-On-Demand] to determine the x and y offset. The x offset is adjusted within the print job file and the y offset is adjusted by the stepper motor.

However, the use of a new type of printer entails new settings and components. Usually, a higher resolution in printing is obtained with smaller nozzles or different settings for the piezo-element for instance. The solution was therefore diluted further further (1 ml PEDOT:PSS (1.3%wt) : 9 ml H₂O).

Separate nozzle

Quantified Air B.V. is a small company in the Netherlands. They have build their own ink-jet printer: One nozzle ($\varnothing 30\ \mu\text{m}$) is combined with a stage (XY) and can be fully manually controlled. A stroboscope and camera enable the sight on the sample and the droplet. The nozzle can be controlled manually. Its rise time, fall time and pulse voltage can be adapted to the needs of the experiment. A schematic of the setup is presented in Figure 2.7.

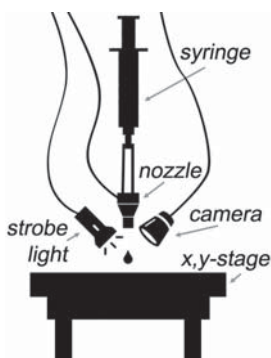


Figure 2.7: The setup of the ink-jet printer with one nozzle only. The upper part with the nozzle, camera and strobe light can be moved up and down to control the distance between the nozzle and the sample.

2.2.3. Two-photon Laser Direct Writing

Laser Direct Writing [LDW] techniques use a laser beam to polymerize a photosensitive material, locally. Two-photon polymerization enables the fabrication of structures with accuracy in the range of micrometres to nanometres. This principle requires that the sum of the energy of two photons is equal to the energy that the photo initiator needs for a transition from the ground to an excited state. Such a photo-induced excitation of the molecules causes a chemical reaction, initiating polymerization: reacting monomer molecules form polymer chains. The relation between this two-photon absorption and the laser intensity is quadratic [69]; the three dimensional voxel³ relates to a squared point-spread function. Figure 2.8 a. [14] shows the shape of the focus point of the laser, with a darker red area representing a higher intensity. The corresponding two-dimensional graph is shown in b. where the squared excitation intensity is plotted against x . When comparing this to the energy that is needed to excite the photosensitive material, Figure 2.8 c. shows that only a specific volume in the focus point of the laser has enough energy that is higher than the polymerization threshold. The voxel is highlighted with a purple colour. In Figure 2.8 d. it can be seen that the resolution of writing corresponds to the width of the quadratic function of the laser intensity at this threshold. The resolution of the writing increases when decreasing the laser power (Figure 2.8 e.).

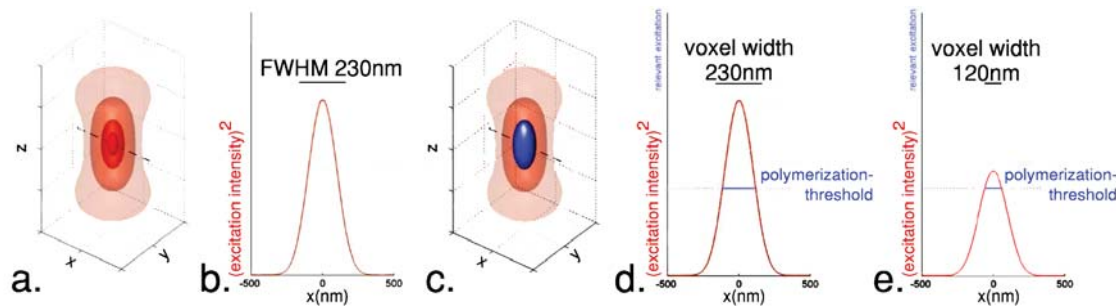


Figure 2.8: The focal point of a laser beam is shown in picture a. A darker red area represents a higher intensity. The corresponding two-dimensional graph is shown in b. where the squared relation between the excitation intensity and x can be seen. FWHM is the abbreviation for Full Width at Half Maximum. The purple colour in graph c. shows the polymerized volume caused by the laser in a resin. As can be seen in subfigure d., the width of the graph at the polymerization threshold corresponds to the writing resolution. When the laser intensity is decreased in subfigure e., the resolution increases [14].

The machine that is used for this LDW process is a Photonic Professional FT (Nanoscribe GmbH) [Nanoscribe]. It uses a near-infrared [near-IR] laser beam with a wavelength of 780 nm. It has to be mentioned that the used photosensitive resin needs to be transparent to this near-IR such that the resin outside the voxel does not have much effect on the intensity of the laser (no fading). By deflecting the laser beam with mirrors and adjusting the focus, writing in three directions (Figure 2.9) is enabled.

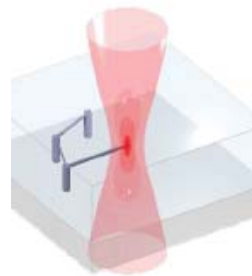


Figure 2.9: The solidified resin can form a structure as shown in this picture. This is only possible when writing in three (x , y and z) directions is possible [14].

Usually, structures are build on top of a glass plate. Previous experiments showed that the technique is capable to write on other structures. Micro-optical structures were drawn on optical fibres [70] and tailored

³A voxel can be seen as a volumetric three-dimensional pixel [61].

probes were fabricated on silicon cantilevers for AFM utilization [64, 71]. Hence, the addition of material on a cantilever for this research, must be possible.

The setup of the Nanoscribe consist of a lens, glass substrate and detector among other things. The NIR laser is focussed through the lens and is directed upwards on a glass substrate. A detector collects the refracted light. By changing the position of the lens to create a smaller or larger distance between the lens and the glass substrate, software can calculate the location of the glass substrate. An interface can be found which enables writing on the substrate. There are two printing configurations for the Nanoscribe: Dip-in Laser Lithography [DiLL] [64] and Immersion [70, 71]. When using the DiLL configuration, the photoresist is situated between the lens and the glass substrate. Writing is done on the bottom side of the glass plate which enables the fabrication of structure heights larger than the working distance. In the conventional mode, immersion oil is placed between the objective lens and the glass plate to increase the numerical aperture of the lens. The photoresist is placed on top of the substrate. Hence the manufacturing of structures takes place on the upper side of the glass, limiting the structure height to be smaller than the working distance.

In this research the goal is to write on a cantilever beam. If the beam blocks the laser to propagate further towards the detector, the DiLL mode will entail a risk of damaging the lens. The system will not be able to detect the location of the glass substrate and could break the cantilever with the objective. For this reason the immersion configuration is used in this method. Figure 2.10 shows the used setup. The supporting substrate of the cantilever is 300 μm high which is larger than the working distance (190 μm). Therefore, the chip has to be turned over such that the cantilever is situated within the working distance of the Nanoscribe. Due to the fact the the cantilever lies on top of its support, a piece of glass is placed in between Nanoscribe's substrate and the chip's substrate. In this way, a distance is created between the cantilever and the glass substrate such that writing on the cantilever is possible.

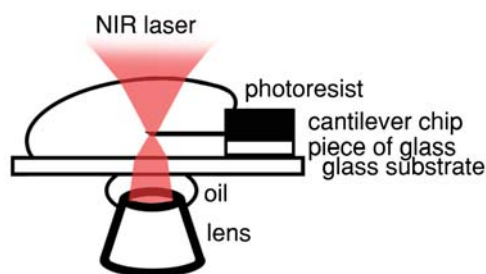


Figure 2.10: The setup of a cantilever in the Nanoscribe can be seen in this figure. The glass substrate is placed in a holder above the lens. A piece of glass is mounted on top of the substrate to create a known distance between the cantilever and the glass substrate. The chip is placed up-side-down on the glass piece such that the cantilever is not supported. The dimensions are exaggerated to create more clear overview.

A camera enables a view on the situation from below. By adjusting with the focus of the lens, the laser can be focused on the surface of the cantilever. Unfortunately, the cantilever blocks the laser and the system is not able to find the interface of the cantilever automatically. This has to be performed manually (see Appendix A).

To obtain a better adhesion state, a low pressure plasma system (Femto standard Femto-UHP corrosive gas version, Diener Plasma-Surface-Technology) with an oxygen gas flow is used to clean the cantilevers. Gas atoms are excited to a higher energy state from which plasma arises. The plasma breaks the organic bonds of the contaminants from the surface. The oxygen is able to bind with the released hydrogen and carbon molecules. Due to the gas flow, the contaminants are removed from the sample chamber. [72]

Table 2.1 gives an overview of the resins that Nanoscribe GmbH. offers. Since IP-L 780 has the highest resolution and a low shrinkage, this photoresist is chosen.

Many steps need to be performed for the fabrication of a structure on the cantilever. It begins with the preparation of the glass substrate (Thermo scientific, Menzel-Gläser, deckgläser $\varnothing 30$ mm #1.5, selektiert 0.17 ± 0.01 mm). The glass needs to be cleaned with acetone (EMSURE), subsequently with di-propanol (Honeywell Riedel-de Haën, $\geq 99.8\%$) and finally it needs to be blow dried gently. This is important for the minimization of contaminants. After the cleaning process, the substrate can be put in a specific holder. A small piece of glass (thickness 80 μm) can be taped to the glass substrate, after going through the same cleaning steps. The piece should be attached at a location off centre such that the system will be able to find an interface in the beginning of the writing process. Meanwhile, the cantilever chip needs to be cleaned with oxygen

Table 2.1: An overview of the available IP photoresists from Nanoscribe. [18]

	Form	Pre-bake / Post-bake	Resolution	Shrinkage
IP-Dip Index-matched resist formula to serve as immersion and photosensitive material	Liquid	No / No	High	Medium
IP-L 780 Highest-resolution resist formula	Liquid	No / No	High	Low
IP-G 780 High-viscosity resist for complex 3-D writing trajectories	Sol-gel ^a	Yes / No	High	Low
IP-S Index-matched medium-resolution resist for smooth surfaces and fast structuring of large 3D parts	Liquid	No / No	Medium	Low

^a *In materials science, the sol-gel process is a method for producing solid materials from small molecules. The process involves conversion of monomers into a colloidal solution (sol) that acts as the precursor for an integrated network (or gel) of either discrete particles or network polymers [73].*

plasma. Subsequently, it can be placed on the small glass piece. Afterwards, the photoresist should be added such that the cantilever is immersed. A droplet of immersion oil needs to be added on the downside of the glass substrate thereafter. When this procedure is completed, the holder can be placed in the Nanoscribe system. The glass interface will be found by the system automatically, but the surface of the cantilever needs to be found using the command 'ManualControl' (see Appendix A). Subsequently the structure can be build on the beam. When the sample holder is taken out of the Nanoscribe, the photoresist needs to be cured in propylene glycol monomethyl ether acetate [PGMEA] (Sigma-Aldrich, $\geq 99.5\%$) for 25 minutes and hereafter in di-propanol for 5 minutes. Finally, the setup can be blow dried gently.

2.2.4. Material properties

The cantilever that was used for the experiments is made of silicon, with a coating of aluminium on top to enable the detection of movement. The ink-jet deposited material is PEDOT:PSS. The photoresist IP-L 780 is deposited on the cantilever via the Nanoscribe system. The material properties [37, 74–76] of all used materials are listed in Table 2.2.

Table 2.2: The material properties of the used materials are listed in this table.

Material	Young's Modulus [GPa]	Density [kgm^{-3}]
Silicon	169	2330
Aluminium	69	2700
PEDOT:PSS	0.9 ± 0.2	958
IP-L 780	$1.3 - 2.15^a$	1000 - 1200 ^a

^a *The material properties depend on the used laser power and exposure time.*

2.3. Experiment: Cantilever multi-modal measurements

2.3.1. Actuation

A wide variety of actuation methods exists: magnetic, piezoelectric base, photo-thermal, acoustic and electrostatic actuation are few examples. Piezoelectric excitation has the advantage that no modification to the chip is needed.

The setup that is used for the excitation of the cantilever consist of a printed circuit board [PCB], a spring, piezoelectric actuator (0.5 mm thick, Piezo Systems Inc.) and a piece of PDMS (125 μm thick, Shielding Solutions) as can be seen in Figure 2.11 [15]. The chip is placed on the actuator with PDMS in between to obtain better contact between the chip and the actuator. In this way a more efficient excitation energy transfer is received.

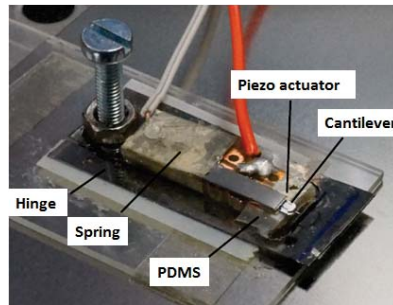


Figure 2.11: The setup shown in this figure [15] is used for the clamping and actuation of the cantilever. A spring is used to keep the cantilever chip in place on top of a piezoelectric actuator. In between the actuator and the chip, a piece of PDMS is placed for an increase in contact.

2.3.2. Detection

In order to measure the frequency response of the system, the amplitude of the deflection needs to be measured. Since the dimensions of the cantilever are in the microscale range, the deflections are small. The velocities will be larger and therefore easier to distinguish from noise. Measurement methods are shown in figure 2.12.

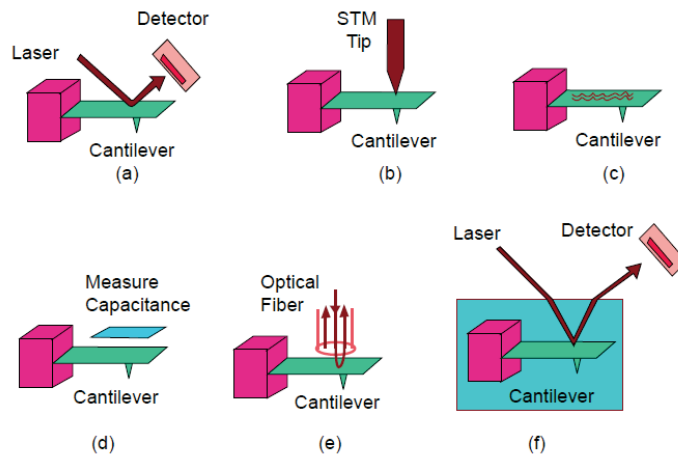


Figure 2.12: A variation of detection methods to measure the deflection of a beam [3]. (a) Optical detection. (b) This method uses a Scanning Tunnelling Microscope tip to measure the change in tunnelling current caused by a variation of distance between the tip and the surface. (c) Piezoresistive material has a changing resistance due to the strain that is caused by bending. (d) The cantilever and a parallel plate act like a parallel-plate capacitor. Deflection is detected because of the changing distance between the two parts. (e) Optical interferometry. The distance affects the interference pattern.

Optical detection methods do not affect the sensitivity of the sample and do not add complexity to it. Optical beam deflection and homodyne laser interferometry are the most commonly used detection methods for measuring the deflection of a beam [77]. A Micro System Analyzer [MSA] (Polytech, MSA-400) uses a laser Doppler vibrometer [LDV] to obtain the velocity and displacement of a sample. When directing a laser beam on a test object, the incident light is scattered by the movement of the sample. As a result, the backscattered light has a change in frequency and phase, corresponding to the characteristics of the motion of the surface. Comparing this with reference light, it provides the vibrational velocity and displacement at one point of the sample. By analysing multiple points of the test object when exciting at specific frequencies, the operational deflection shape can be calculated for each frequency. When investigating these deflection shapes, the peaks of the frequency spectrum and the corresponding phase information should be considered likewise. The deflection shape does not always correspond to a mode shape since it can be influenced by joining shapes. The operational deflection shape is a large advantage of the system since Virtual Network Analysers and AFM systems cannot give this information.

The MSA system at TU Delft uses a Helium Neon laser with a wavelength of 633 nm within the fibre optic interferometer (Polytec OFV-512). The laser spot size diameter goes down until 3 μm . The used setup for the beam detection is roughly sketched in Figure 2.13.

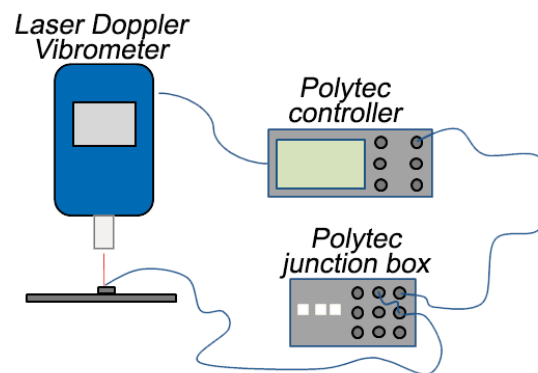


Figure 2.13: The setup that is used for the detection of the frequency response is visualised in this figure. A laser Doppler vibrometer [Polytech, MSA 400] is used to measure the velocity and displacement of the sample, which is placed underneath the lens. A vibrometer controller [Polytech, OFV-5000], junction box [Polytech MSA-400], computer [Polytech, DMS] regulate all the electronics.

2.4. Experiment: Cantilever parameters

The previous sections elaborated on all the steps of the experimental process of this research. Therefore, all the requirements for a cantilever can be listed. First of all, multiple modes have to be detected. The LDV system at Delft Technical University has a bandwidth of 1 MHz. The stiffness of the cantilever has to be low enough to measure at least five flexural modes. A shorter cantilever has a larger stiffness accompanied by a higher eigenfrequency ([10]). Furthermore, the surface of the cantilever has to be reflective since the movement is measured with a laser beam. For example silicon nitride has a low reflectivity, which results in a small signal-to-noise ratio [62]. Additionally, the thickness of the support chip needs to be large enough such that a minimal effect on the clamping of the cantilever is obtained [78]. Finally, the added material has to adhere to the cantilever surface.

AFM probes are commercially available within a wide range of resonance frequencies and dimensions. Often a layer of for example aluminium is added in order to improve the reflectivity for measurements. Because of these reasons, AFM probes can be competent for this research. These cantilevers are produced from mono-crystalline silicon wafers. The material is built in a $\langle 100 \rangle$ plane. All production steps are performed such that the cantilevers point in the $\langle 110 \rangle$ direction. Appendix B elaborates on the fabrication of the probes. The CONTR probes from NanoWorld have a resonance frequency at 13 KHz and a reflective aluminium coating. The properties are listed in Table 2.3. The support chip has dimensions 1.6 mmx3.4 mmx0.3 mm and the aluminium coating has a thickness of 30 nm. The reflectivity of the cantilever is increased by a factor of 2.5 because of this coating [19].

Table 2.3: This table lists the properties of the cantilever that is chosen for this research [19].

AFM tip		
Shape	Standard	
Height	10 - 15 μm	
Radius	<8 nm	<12 nm guaranteed
AFM cantilever		
Shape	Beam	
Length	450 μm	445 - 455 μm
Width	50 μm	45 - 55 μm
Thickness	2 μm	1.5 - 2.5 μm
Force constant	0.2 Nm^{-1}	0.07 - 0.4 Nm^{-1}
Resonance frequency	13 KHz	9 - 17 KHz

2.5. Analytical Model: Modal Analysis

The Euler-Bernoulli beam theory is used for the theoretical model of this research. The corresponding shape function is derived in Appendix C [55] and is assumed not to change due to adhesives. The model presumes a slender beam which requires a length, thickness-ratio larger than ten. (For the used cantilever, this ratio is equal to 225.) The rotation inertia and shear deformation are neglected. A uniform rectangular cross-section, small deflections and linear elastic material properties are assumed. Damping is neglected, as are the effects of any surrounding fluid, such that Rayleigh's quotient can be used to obtain the theoretical values of the resonance frequencies.

2.5.1. Modal analysis of a cantilever beam

The cantilever is modelled as shown in Figure 2.14. The length L , width W and thickness T are derived via an SEM.

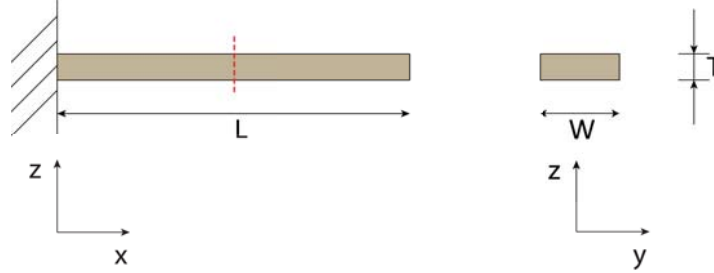


Figure 2.14: Solid cantilever side view and cross section

The following equation can be used to calculate the eigenfrequencies of a clamped-free beam.

$$\Omega_n = \frac{\lambda_n}{L^2} \sqrt{\frac{EI}{\rho A}} \quad (2.1)$$

In this equation the roots of the frequency formula are represented by λ (the value can be found in Appendix C) with a subscript n suggesting the mode number. The Young's modulus of the material is depicted with E and the moment of inertia is described by I ($I = \frac{WT^3}{12}$). Density is ρ and the cross sectional area is introduced via A ($A = WT$).

The inverse method is used to calculate the Young's modulus of the cantilever. The density of silicon can be assumed constant for each beam with a value of 2330 kg cm^{-3} . The $\pm 30 \text{ nm}$ aluminium layer is neglected. The resulting E is different for each beam. Experimentally derived resonance frequencies are used to solve Equation 2.1 over E . A Young's modulus is found for each mode shape. The mean value is used for further calculations.

2.5.2. Modal analysis of a cantilever beam with added polymer

An example for a situation of a cantilever with adhesive is shown in Figure 2.15. In this schematic, the added material is shown on an arbitrary location. Since the adsorbate's thickness (T_a) is a function of x along the length of the beam, the statements in this section hold for every situation. A subscript c is added to the symbols regarding the cantilever and a subscript a to symbols concerning the adsorbate.

The variables L_a , W_a , T_a and x_s are obtained by SEM pictures. W_a should have the same value as W_c . The flexural rigidity D of the system is changed due to the adhesive. Within this function, T_a is a function of x . Over the length of the beam it is zero, except for the location of the adhesive from x_s to $x_s + L_a$, where it is equal to T_a . Equation 2.2 [79] shows the relation of flexural rigidity to the system properties.

$$D(x) = \frac{W}{12} \frac{E_c^2 T_c^4 + E_a^2 T_a^4(x) + 2E_c E_a T_c T_a(x) (2T_c^2 + 2T_a^2(x) + 3T_c T_a(x))}{E_c T_c + E_a T_a(x)} \quad (2.2)$$

The effect of the adhesive on the resonator is investigated via Rayleigh's quotient. The potential and kinetic energy of the system per oscillation cycle are given by Equation 2.3 and 2.4 respectively [37]. The symbol α is a random value for the amplitude of the displacement. [38]

$$V = \frac{\alpha^2}{4} \int_0^L D(x) \left(\frac{\partial^2 \psi_n(x)}{\partial x^2} \right)^2 (x) dx \quad (2.3)$$

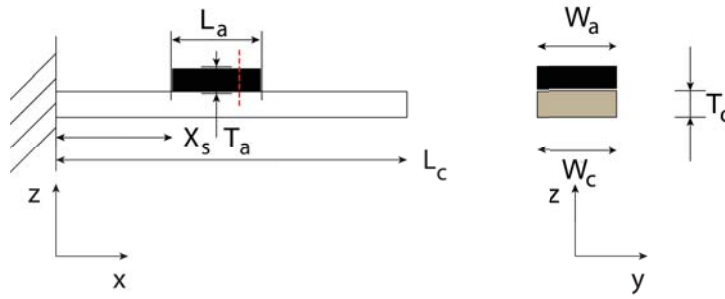


Figure 2.15: Solid cantilever with adsorbate side view and section

$$T = \frac{W a^2}{4} \int_0^L (\rho_c T_c + \rho_a T_a(x)) \psi_n^2(x) dx \quad (2.4)$$

The Rayleigh quotient can therefore be obtained as

$$\Omega_{add}^2 = \frac{\int_0^L D(x) \left(\frac{\partial^2 \psi_n(x)}{\partial x^2} \right)^2 dx}{\rho_c W T_c \int_0^L 1 + \frac{\rho_a T_a(x)}{\rho_c T_c} \psi_n^2(x) dx} \quad (2.5)$$

Via an optimization method, the density and Young's modulus are obtained by minimizing the error between experimentally derived resonance frequencies and theoretically determined eigenfrequencies. Chapter 3.4 elaborates on this.

3

Results

This chapter presents the experimentally derived results. Four different samples are examined: two with an adhesive near the tip and two with added material near the base of the cantilever. The frequency spectra are obtained with a resolution of ~ 1.22 Hz and show the mean value of 30 measurements.

3.1. Deposition of a polymer by various methods

3.1.1. Dipping

As is shown in Figure 3.1, the beam first pushed the droplet but did not enter immediately. In Figure 3.1 e. it is shown that the beam enters the droplet. When withdrawing, no water came along with the beam. It can be concluded that the beam was hydrophobic. To improve this setup, the chip should be cleaned with oxygen-plasma ¹(Air or Argon plasma treatment) before mounting it on the micro-robot. In this way, the surface could become slightly hydrophilic.

When applying an oxygen plasma treatment on the cantilever, organic bonds will break and it becomes more likely for contaminants to fall apart. The less impurities present on the surface, the more hydrophilic it becomes. However the passivation process will start again when the cantilever gets in contact with air and all its pollution. The preparation process takes time and the cantilever chips can easily be demolished. Additionally, it will be hard to control the added volume.

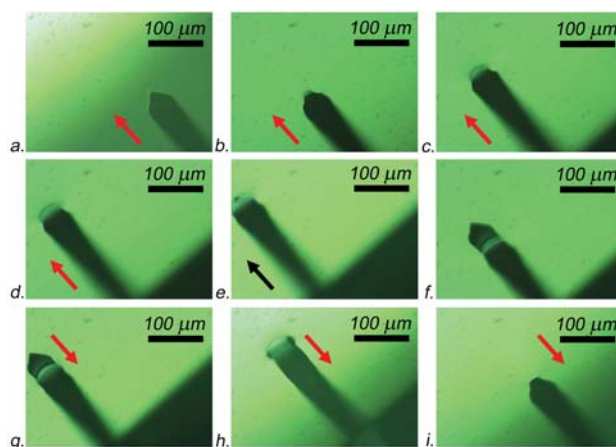


Figure 3.1: These pictures show how a cantilever is dipped into a droplet of water. Figure a. shows a cantilever that is approaching the edge of a droplet. It touches the droplet in b. and pushes against it in c. and d. In e. the cantilever has enough force to break through the surface stress and enter the droplet as shown in f. When retracting the cantilever from the droplet as visualised in g., h. and i., one can see that no liquid is withdrawn by the cantilever. The surface is hydrophobic.

¹O₂plasma treatment is explained in Chapter 2.2.3

3.1.2. Ink-jet printing of a water-soluble polymer

When placing a cantilever beam underneath the printhead, a lucky shot was needed to hit the cantilever with the droplets. One of the results, after many tries, is displayed in Figure 3.2. The first hit formed the added material near the clamped side of the cantilever. The second hit was located near the tip. This shows that it is difficult to deposit material on a precise location. Hence it is a challenge to control the added volume. Additionally, the amount of droplets that were placed can not be derived from this picture.

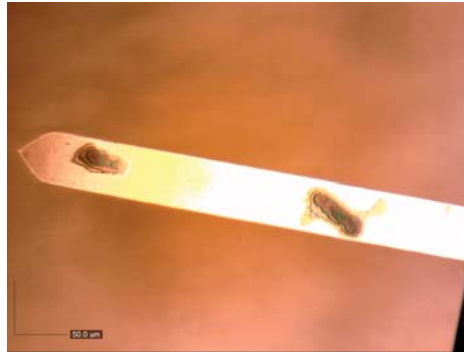


Figure 3.2: EPSON Stylus SX235W desktop printer.

A more accurate deposition of material was obtained with an EPSON XP-235 desktop printer with a stepper motor (see Appendix D) but the location was still hard to determine. Since the concentration of PEDOT:PSS is low, a lot of droplets are needed. These are too small and therefore not visible with the naked eye. This makes it hard to obtain and control a precise localization with the Drop-on-Demand system. Furthermore, the exact amount of printed droplets can not be seen in real time, which makes it difficult to obtain the added mass and it affects the repeatability of the method. On the other hand, the material properties of PEDOT:PSS are known and the substance is slightly conductive which makes an evaluation with an SEM possible. If camera's would be added to the printer for real life tracking of the droplets, the device would become even more promising for future research.

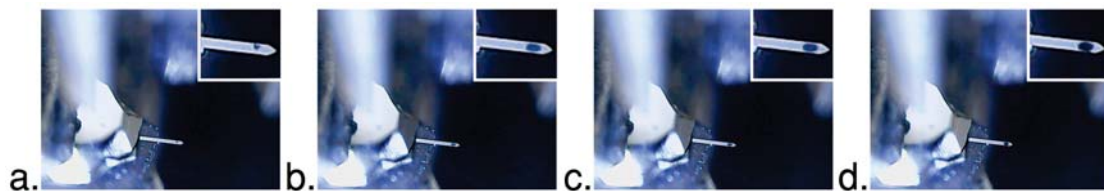


Figure 3.3: Droplets of a solution of PEDOT:PSS in water (1 mL PEDOT:PSS (1.3%wt) : 10 mL H₂O) are deposited on a cantilever. The most left picture a. shows the situation with one added droplet. Photos b., c. and d. show 4, 7 and 10 droplets respectively.

The usage of the ink-jet printer with one nozzle only [Quantified Air B.V.] resulted in the addition of a controlled number of droplets. The droplets have a volume of ± 15 pL. The determination of the location is more precise with this method. As can be seen from Figure 3.3a., the first droplet is deposited on the beam. Unfortunately it remained hard to add one droplet exactly on the centreline of the cantilever near the tip.

3.1.3. Two-photon polymerization

The first result derived with the Nanoscribe is shown in Figure 3.4. It can be seen that the added polymer is not laying exactly on the centreline. Figure 3.5 shows a camera view on the cantilever while it is inside the Nanoscribe system. Here, the localization of the added material is optimized and accurate.

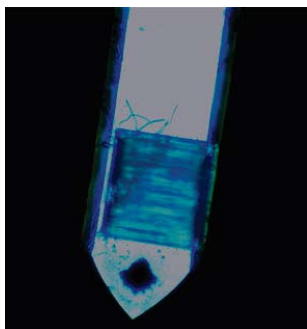


Figure 3.4: The first result derived via two-photon polymerization is shown in this figure, obtained via an optical microscope. A well shaped blue cube can be seen. The colour is due to the light of the microscope.

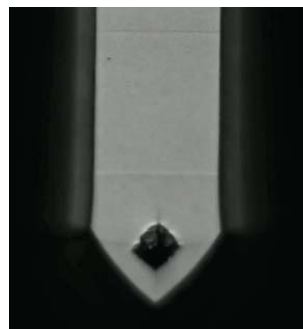


Figure 3.5: The Nanoscribe system contains a camera to enable sight on the writing process. This picture is taken with this camera after the polymerization process while the cantilever chip was in the system. The location and shape of the result are visible.

3.1.4. Discussion on deposition methods

Table 3.1 lists the advantages and disadvantages of the investigated deposition methods. Where dipping did not lead to usable results, the ink-jet method with one nozzle (Quantified Air B.V.) and the two-photon polymerization with the Nanoscribe both show promising results.

Since the experimental results have to be linked to a theoretical model, it is important to know the shape of the adhesive. Since any shape can be produced by the Nanoscribe, the approximation of it will be more precise than the droplet-like shape produced by the ink-jet technique.

The two-photon polymerization method involves risks. Within the many steps for the Nanoscribe, the cantilever has to be handled carefully. Cantilevers break easily. If this happens, it cost time and money.

To validate the method, the material properties of the adhesive need to be known. PEDOT:PSS is used for the ink-jet technique and IP-L 780 within the Nanoscribe. The properties of both materials can be found in the literature. The downside of IP-L 780 is that the properties depend on the used laser power. A polymerization process is sensitive to different factors: humidity, efficiency of the photoresist, the exposure time, the laser power and the temperature of the environment. Nanoscribe GmbH services state that there are no strong variations in the needed laser power as long as there is a stable surrounding temperature. Despite these promises, variations in all the factors should be kept to its minimum.

The cantilevers are clamped in a setup for the actuation. This clamping entails damping which influences the resonance frequency. The chip can remain clamped in the system when ink-jetting material on the cantilever. This minimizes the effect of the clamping on the measurements. For the addition of material with the Nanoscribe, the chip has to be taken out of the setup.



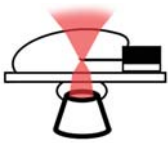
An important factor in science is the repeatability of an experiment. When each experiment differs a lot, it will be hard to draw conclusions from statistics. The concentration of PEDOT:PSS in the solution is very low resulting in a variation of concentration per droplet. When using the Nanoscribe system, an array of cantilevers can be attached on the glass plate. Multiple experiments could be performed under exactly the same conditions, contributing to the repeatability.

Additionally, the location of deposition of material is controlled manually for both methods. The ink-jet printer allows sight on the sample under an angle. This makes it difficult to determine whether the cantilever is underneath the nozzle or not. Although the resolution of the camera is good enough to accurately deposit material at a location, obtaining the exact wanted position is hard. The Nanoscribe allows to use a low laser power to localize the focus point of the laser beam. Hence the location can be obtained more accurately.

Altogether, the ink-jet method gives rise to easy and fast results. However, further testing was not feasible at the moment due to additional costs and also time constraints.

The use of the Nanoscribe is currently difficult because little research is done on the addition of the material on a cantilever at the TU Delft. The experiments will take more time in the beginning since much

Table 3.1: The advantages and disadvantages of the three experimentally investigated deposition methods are listed in this table. Because of the control of the shape and location of the polymerized structure, two-photon polymerization is chosen to be the method to continue with.

Method	Advantages	Disadvantages
	No results are obtained due to the hydrophobic surface of the cantilever.	
	<ul style="list-style-type: none"> • Easy & fast method • PEDOT:PSS is slightly conductive • Chip remains in the clamping of the setup 	<ul style="list-style-type: none"> • Risk on clogging • Risk on contamination
	<ul style="list-style-type: none"> • Shape control • Deposition location control 	<ul style="list-style-type: none"> • Material properties depending on laser intensity • Risk on damage due to many handling steps

knowledge has to be collected. Nevertheless, the controlled manufacturing of shapes and the need for large datasets make the usage of the Nanoscribe interesting. Without potentially having coupling between beams when using arrays of resonators [51], this method is promising for the investigation of mass and stiffness effects. Hence it has been chosen as the deposition method for this research. All presented results in the coming sections are derived with added polymers via two-photon polymerization.

3.2. Polymer location

Two different locations for the deposition of a two-photon polymerized layer are used in this research: near the tip and near the base. In total, four samples are investigated (tip_1 , tip_2 , base_1 and base_2)². A side- and topview of two samples are shown in Figures 3.6 and 3.7, and 3.6 and 3.7. All the pictures are taken by an SEM and the polymer has a fake yellow colour. The SEM pictures for other samples can be found in Appendix F.1.

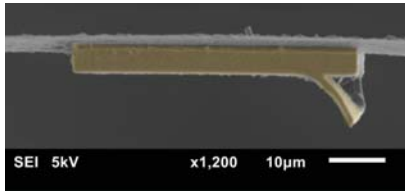


Figure 3.6: An SEM picture of the adsorbate on sample tip_1 . The cantilever tip is pointing to the right. It can be seen that delamination has occurred on the upper layer near the end.

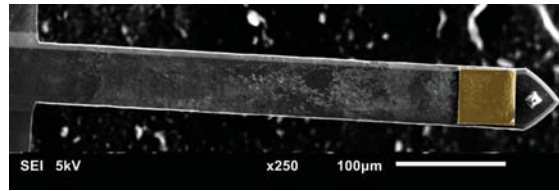


Figure 3.7: An SEM picture of sample tip_1 . The added polymer is located near the tip of the cantilever.

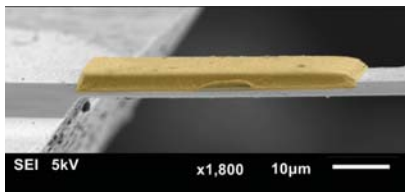


Figure 3.8: An SEM image from the side of the adsorbate on a coloured sample near the base (base_1).

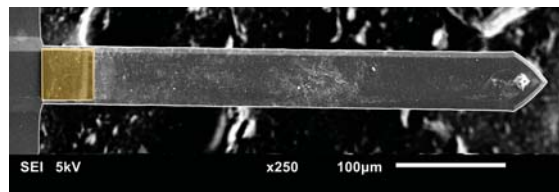


Figure 3.9: An SEM picture of sample base_1 . The added polymer is located near the base of the cantilever, highlighted with a yellow colour.

3.3. Modal analysis

Polymeric layer near the tip

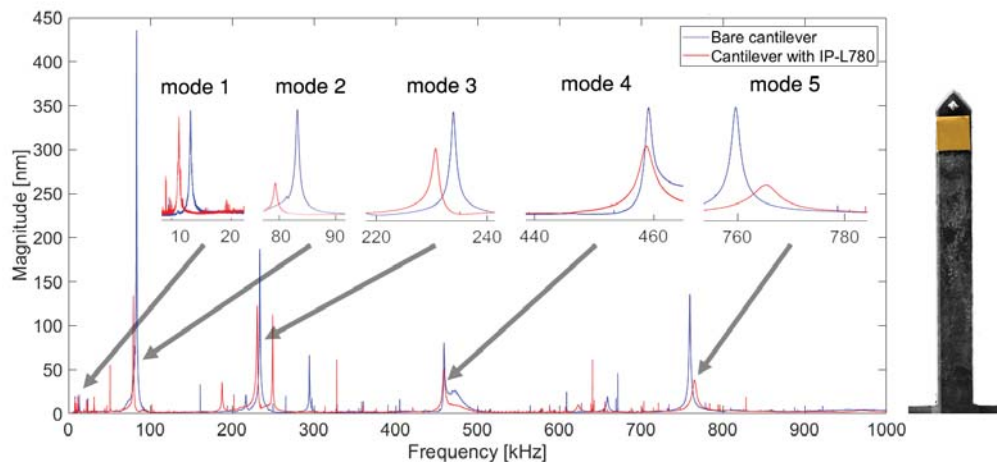


Figure 3.10: This figure shows the frequency response of a bare cantilever represented by the blue line. An added layer IP-L 780 ($\pm 50 \times 50 \times 3 \mu\text{m}$) is deposited near the tip, highlighted with colour. (sample tip_1)

²In the raw measurement data, tip_1 corresponds to sample 20.2, tip_2 to 20.10, base_1 to 20.4 and base_2 to 20.7.

Table 3.2: The values for the frequency shift of caused by a polymeric layer near the tip of a cantilever are listed in this table.

Mode number	1	2	3	4	5
f before [kHz]	13.13	83.23	233.9	459.1	759.7
f after [kHz]	11.21	79.34	230.7	458.7	765.3
Δf [kHz]	-1.92	-2.89	-3.2	-0.4	+5.6
Δf [%]	-14.62	-3.51	-1.37	-0.09	+0.74

From Figure 3.10 and Table 3.2 it can be seen that the addition of material near the tip results in a decrease of the resonance frequency for the first modes. However, the fifth mode shows a change in sign: a positive shift arises.

Polymeric layer near the base

According to literature, an adsorbate located near the base of a cantilever should result in a positive frequency shift. As can be seen from the graph in Figure 3.11 this holds for the first four modes when added a polymeric layer near the base. The fifth mode shows a decrease in resonance frequency.³

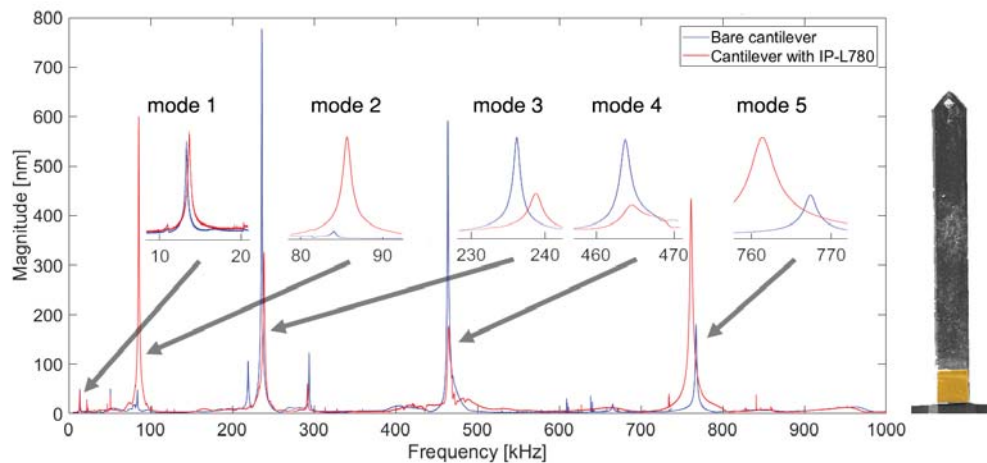


Figure 3.11: This figure shows the frequency response of a bare cantilever represented by the blue line. The picture on the right depicts the same cantilever with a false-coloured added cube IP-L 780 ($\pm 50 \times 50 \times 3 \mu\text{m}$) near the clamping. (sample base₁)

Table 3.3: Sample base₁

Mode number	1	2	3	4	5
f before [kHz]	13.31	84.07	236.1	463.7	767.4
f after [kHz]	13.7	85.62	238.7	464.4	761.1
Δf	+0.39	+1.55	+2.6	+0.7	-6.3
Δf [%]	+2.93	+1.84	+1.10	+0.15	-0.82

Comparison of observations on both locations

The added polymeric layer affects the frequency shift which is found to be mode related. The total shift comes from the combination of the influence on both kinetic and elastic energies. Ramos *et al.*[23] used the relation between the deposition location and the frequency shift contribution to assign different regions for the derivation of mass or stiffness. Figure 3.12 shows the relation between the deposition location and the shift in resonance frequency per mode, for an added polymeric layer. As can be seen, the contribution on the frequency shift per mode depends on the location of the added polymeric layer.

³The derived frequency shifts for other samples can be found in Appendix F.1

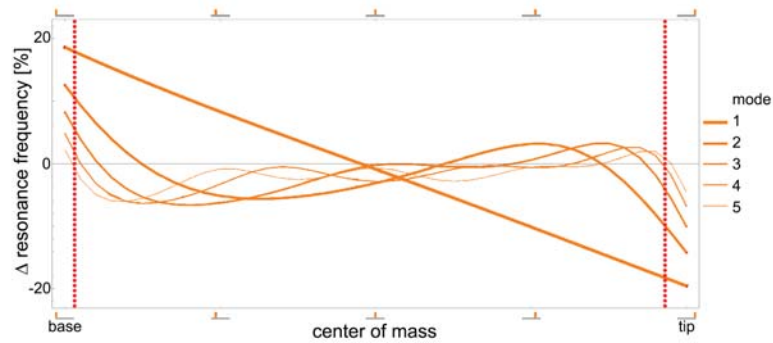


Figure 3.12: The relation between the deposition location and frequency shift per mode is shown in this graph. The thinner the line, the higher the mode. The dotted red lines represent the locations from the experiments of this research.

A deposition position near the clamping results in a large stiffness effect on the frequency shift for the first mode. The higher the mode, the lower this effect. This is similar for a location near the tip, but then the mass effect decreases at higher modes. This is exactly what was found for the samples introduced in the previous two sections. Their locations are highlighted with the dotted red lines. However, Figure 3.13 shows that the last anti-node at higher modes, move towards the location of the centre of mass from the polymer, introducing curvature. Consequently, the absolute stiffness effect is expected to increase at higher modes. The same holds for a polymer located near the base, as can be seen in Figure 3.14. In this case, both deflection and curvature increase at higher modes.

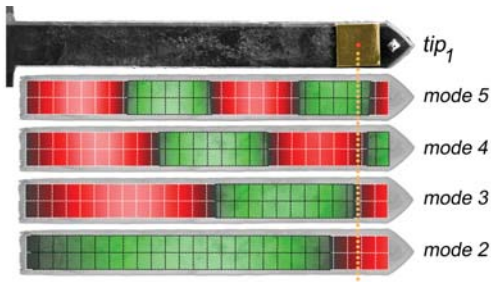


Figure 3.13: In this figure, the location of the centre of mass is compared with the operational deflection shape per mode for sample tip_1 .

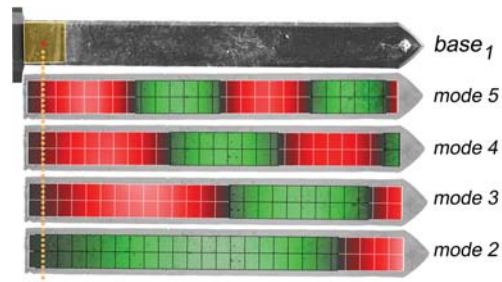


Figure 3.14: In this figure, the location of the centre of mass is compared with the operational deflection shape per mode for sample $base_1$.

By looking at the absolute values for the deflection and curvature of each mode shape (Figure 3.15 and 3.16, respectively), it can be seen that for any location, specific modes give rise to the largest absolute effect on mass or stiffness effect.

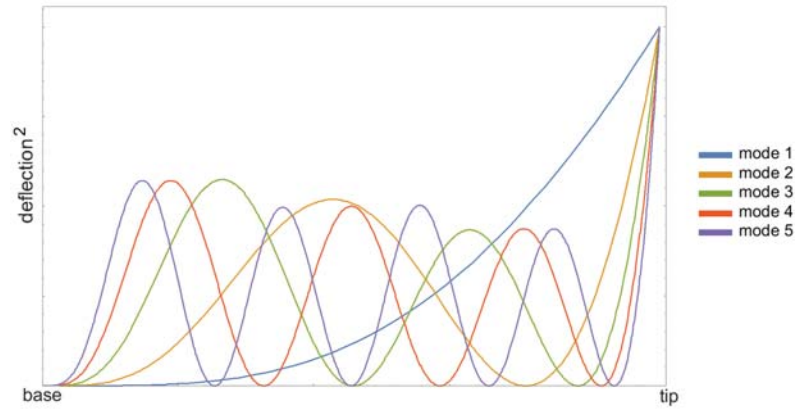


Figure 3.15: The squared deflection of mode shapes 1 to 5 is plotted against the location on a clamped cantilever in this figure. It can be seen that the deflection near the base increases at higher modes. The deflection near the tip decreases at higher modes.

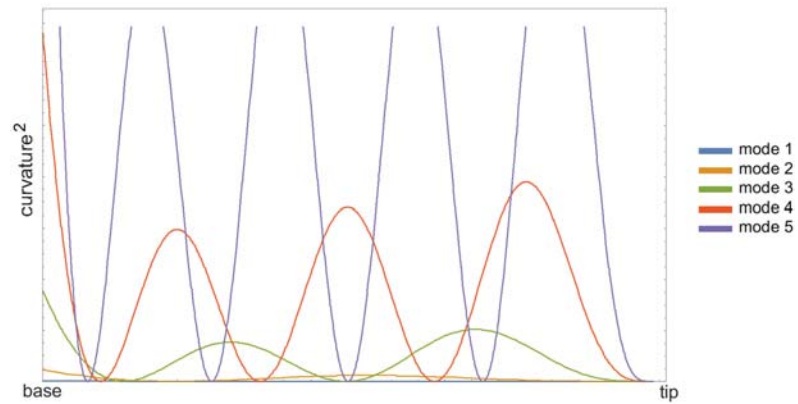


Figure 3.16: The squared curvature of mode shapes 1 to 5 is plotted against the location on a clamped cantilever in this figure. It can be seen that the curvature near the base increases at higher modes. Furthermore, higher modes induce a larger curvature on an added layer near the tip.

In summary, when investigating what mode needs to be used on a specific location for the derivation of mass or stiffness, the relation between the deposition location and the frequency shift contribution (like Ramos *et al.*[23]) or the relation between the deposition location and the absolute deflection or curvature can be used. The following section uses both approaches for the disentangling of mass and stiffness properties.

3.4. Disentangling of mass and stiffness

The shift in resonance frequencies due to the added polymer as found in the previous section, needs to be linked to theory to derive the density and Young's modulus of the polymeric layer. All the presented outcomes in this section are found by minimising the root mean square [RMS] error:

$$\text{RMS error} = \sqrt{\frac{1}{N} \sum_{i=1}^N (f_{\text{theoretical}_i} - f_{\text{experimental}_i})^2} \quad (3.1)$$

3.4.1. Validation

Within this research, theory and experiments are linked with the intention to decouple mass and stiffness effects of an adhesive. In the end, the results need to be validated. They need to be compared to mechanical properties of IP-L 780 from literature. Lemma *et al.* investigated the Young's modulus and density of this material [76].

The investigated polymer by Lemma *et al.* was produced with a scan speed of $100 \mu\text{m s}^{-1}$ and a laser power output differing from 8.8 to 16 mW. These settings deviated from the ones in this research. A scan speed of $10000 \mu\text{m s}^{-1}$ and a laser power output of 204.5 mW were used. The ratio of the intensity over exposure time from literature is 0.088 to 0.16, compared to 0.02045 in this research. These values are not similar. Not only do the laser intensity and scan speed influence the result: Humidity and temperature affect the polymerization process as well. Therefore, the results in the coming section will be compared to the whole range of 1 to 2 GPa for E and 1000 to 1200 kg m^{-3} for ρ .

3.4.2. Decoupling of mass and stiffness based on the frequency shift contribution

Ramos *et al.* [23] state that the mass of a material should be determined by a deposition at a location where a negative frequency shift occurs: near the free end of a cantilever. The stiffness properties should be quantified via a position where a positive change in frequency arises: near the base. Therefore, the density of the polymeric layer in this research is calculated from a given value as discussed in section 3.4.1 for the stiffness for a layer near the tip of a beam. Similarly, the Young's modulus of the added polymer is computed from a density value from literature for samples near the base. Figures 3.17 and 3.18 show that the first mode for a polymer located near the tip gives a density value that has a low sensitivity to the Young's modulus. The first mode for a cantilever with a polymeric layer near the base gives a Young's modulus that seems to have a low sensitivity to the density.⁴

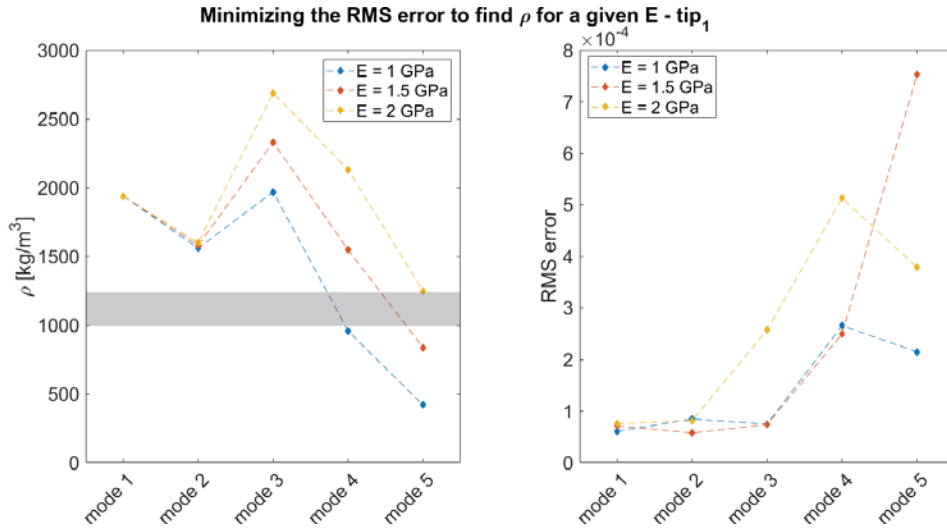


Figure 3.17: The left graph shows the ρ of the added material of sample tip₁ per mode, that corresponds to a Young's modulus of 1 (blue line), 1.5 (orange line) or 2 GPa (yellow line). The right graph shows the corresponding error between the experimental and theoretical values that is minimised. The grey area represents the values from literature. The dashed lines are added to guide the eye.

⁴The graphs for the other samples can be found in Appendix F.2

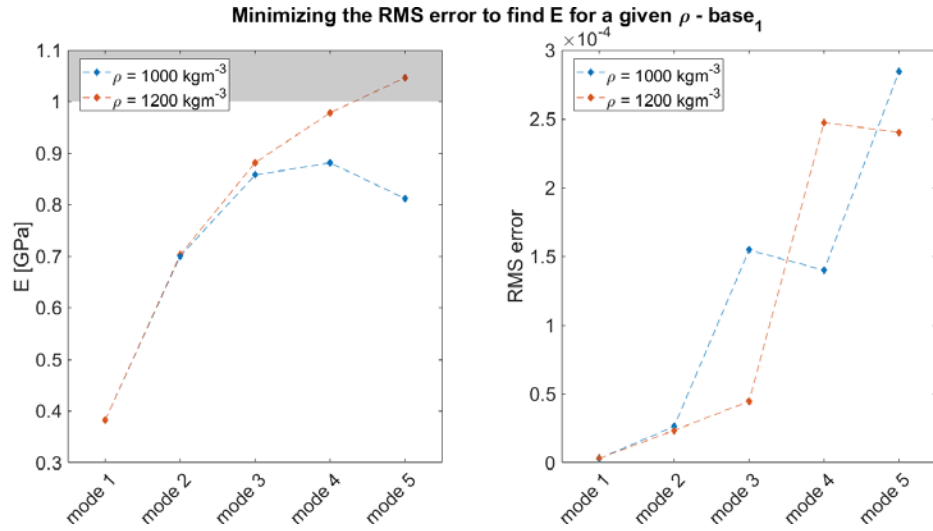


Figure 3.18: In the left graph, the values for E can be obtained from corresponding densities of 1000 kgm^{-3} (blue line) and 2000 kgm^{-3} (orange line) per mode. The grey area represents the values from literature. The minimum difference found on the experimental and theoretical values are shown in the graph on the right. The dashed lines are added to guide the eye.

3.4.3. Decoupling of mass and stiffness based on the absolute deflection and curvature

The relation between the deposition location and the absolute deflection or curvature can be translated into participation factors. They can be calculated for mass and stiffness per mode via the following equations, respectively:

$$\text{participation factor}_{\text{mass}} = \int_0^L T_a(x) \psi_n^2 dx \quad (3.2)$$

$$\text{participation factor}_{\text{stiffness}} = \int_0^L T_a(x) \left(\frac{\partial^2 \psi_n}{\partial x^2} \right)^2 dx \quad (3.3)$$

Since T_a is a function of x , the participation factors will change for different deposition locations.

Figure 3.19 shows the participation factor per mode for a polymeric layer deposited near the tip of the cantilever. The influence of the mass is largest for mode 1 and the stiffness affects the system the most at mode 5.

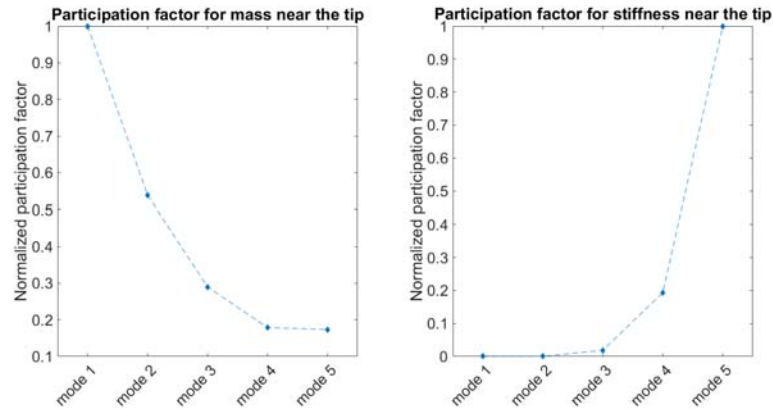


Figure 3.19: The two graphs show the normalized participation factors for sample tip₁ per mode. The left figure gives insight in the participation of mass and the graph on the right-hand side shows the influence of stiffness. The dashed lines are added to guide the eye.

Table 3.4 shows the outcomes of the combination of different modes for the determination of the density and Young's modulus. It can be seen that the combination of modes with a large participation factor, lead to more feasible results when comparing them to the literature.

Table 3.4: Two modes of sample tip₁ are used to derive the values in this table. The RMS error is minimized to find ρ from one and E from another mode. It can be seen that combinations of modes with a high participation factor give feasible results.

mode (ρ [kgm ⁻³])	mode (E)	ρ [kgm ⁻³]	E [Pa]
1	5	1939.18	2.85E+09
1	4	1938.57	1.83E+09
1	3	1938.03	9.57E+08
1	2	1943.84	1.15E+10
2	5	1618.41	2.45E+09
2	4	1581.27	1.53E+09
2	3	1535.17	4.08E+08
3	4	3570.89	3.26E+09
3	5	11462.4	1.66E+10
4	5	-247.176	3.76575
4	3	-247.17	1.00
4	2	-247.17	1.00
4	1	-247.17	1.0017
5	1	-430.97	1.00083
5	2	-430.97	1.00002
5	3	-430.97	1.00
5	4	-430.97	1.00

For an added polymer near the base of the clamped-free beam, the influence of both the mass and stiffness is the highest at mode 5. This is shown by Figure 3.20.

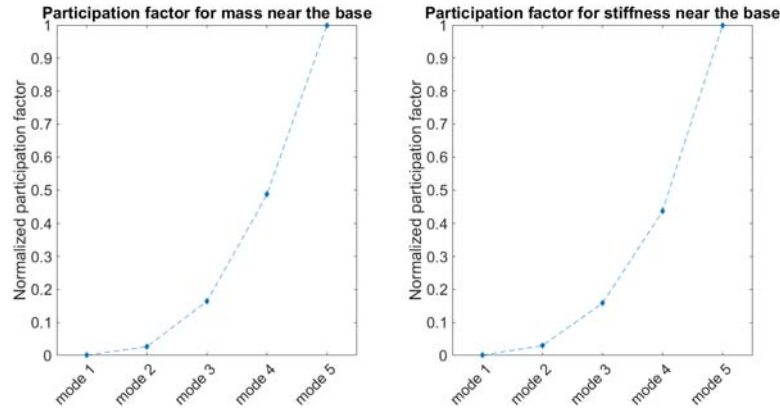


Figure 3.20: The two graphs show the normalized participation factors for sample base₁ per mode. The left figure gives insight in the participation of mass and the graph on the right-hand side shows the influence of stiffness. The dashed lines are added to guide the eye.

It can be seen from Table 3.5 that for all combinations, every mode for the determination of stiffness result in a Young's modulus that is not far off from literature values. However, higher modes do give a value that is more reasonable for the density.

Table 3.5: Two modes of sample base₁ are used to derive the values in this table. The RMS error is minimized to find ρ from one and E from another mode. It can be seen that combinations of modes with a high participation factor give feasible results.

mode (E)	mode (ρ)	ρ [kgm ⁻³]	E [Pa]
4	5	1101.21	9.31E+08
5	4	1101.19	9.31E+08
3	5	1043.58	8.63E+08
5	3	1043.58	8.63E+08
3	4	935.289	8.5E+08
4	3	935.289	8.50E+08
2	5	903.011	6.99E+08
2	4	614.322	6.95E+08
1	5	630.182	3.82E+08
2	3	2.00648	7.39E+08
1	4	2.00646	4.01E+08
1	3	1.33765	7.39E+08
1	2	5.35025	6.87E+08

3.4.4. Comparison between both approaches

The relation between the deposition location and the frequency shift contribution is used to obtain the mass and stiffness properties shown in Table 3.6. Table 3.7 presents the obtained Young's modulus and density per sample, using the relation between the deposition location and the absolute deflection or curvature. The outcomes are feasible, when comparing them to the values from literature. The densities that are found from the samples with a polymeric layer near the tip, are similar for both approaches. The Young's moduli for samples with an added polymer near the base differ.

Table 3.6: This table presents the resulting Young's modulus and density for an approach where the relation between the deposition location and the frequency shift contribution are used.

	tip ₁	tip ₂	base ₁	base ₂
E [GPa]			0.38	1.24
ρ [kgm ⁻³]	1939.18	1389.42		

Table 3.7: This table presents the resulting Young's modulus and density for an approach where the modes with the largest participation factor for mass and stiffness are combined per sample.

	tip ₁	tip ₂	base ₁	base ₂
E [GPa]	2.85	4.23	0.93	2.21
ρ [kgm ⁻³]	1939.18	1389.42	1101.21	2445.11

When inverting the procedure and filling in the outcomes from the above tables in the theoretical model, the shift in resonance frequency can be obtained. These theoretically obtained changes in frequencies are compared to the experimentally derived frequency shifts in Figure 3.21. It can be seen that there is an error between the outcomes for both methods, which seem to be smallest at the modes that are combined to derive the material properties.

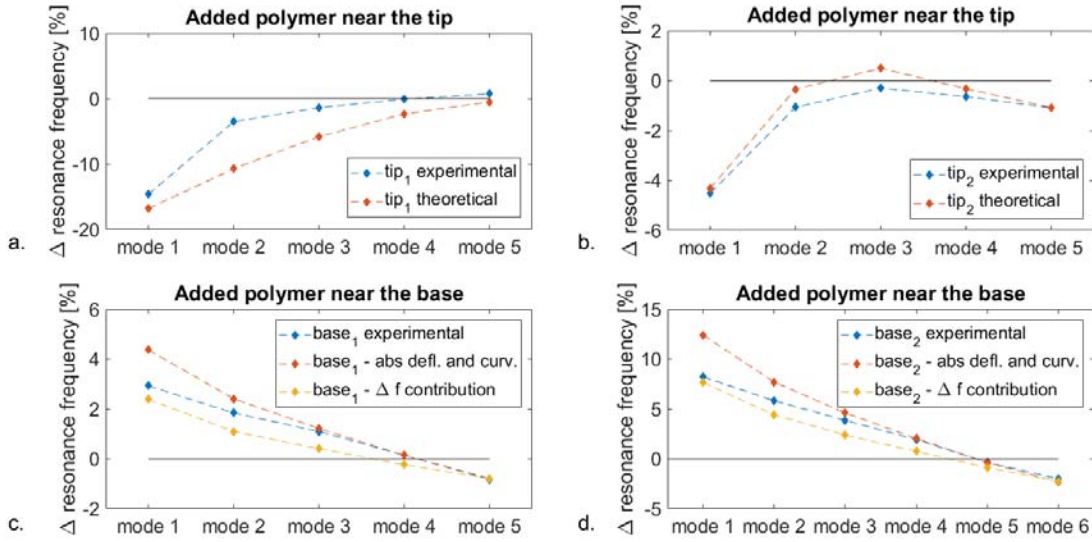


Figure 3.21: These graphs show experimentally and theoretically derived resonance frequency shifts per mode. The dashed lines are added to guide the eye. For subfigure a., the theoretical outcomes are obtained from a density of 1939.18 kgm^{-3} and a Young's modulus of 2.85 GPa . The outcomes shown in subfigure b. are derived via a ρ of 1389.42 kgm^{-3} and an E of 4.23 GPa . The samples with an added polymeric layer near the base showed different outcomes for both approaches: The density and Young's modulus via the modes with the largest absolute values for deflection and curvature (red points) in c. are 1101.21 kgm^{-3} and 0.93 GPa and in d. are 2445.11 kgm^{-3} and 2.21 GPa , respectively. The yellow points are based on modes with the largest frequency shift contribution and show the resulting change in frequency from a density of 630.18 kgm^{-3} and a Young's modulus of 0.38 GPa in subfigure c. and a density of 1623.91 kgm^{-3} and a Young's modulus of 1.24 GPa in subfigure d.

Therefore, a similar graph is made where more than two modes are combined for the derivation of the material properties. Figure 3.22 shows the results per sample when combining the first three, four or five flexural modes. The error does not decrease when increasing the amount of modes.

Table 3.8: This table presents the material properties of the polymeric layer for an approach where the RMS error for a combination of all the measured modes is minimised.

	tip ₁	tip ₂	base ₁	base ₂
E [GPa]	1.26211	1.17651	0.857667	2.00314
ρ [kgm^{-3}]	711.407	505.435	1031.62	2250.61

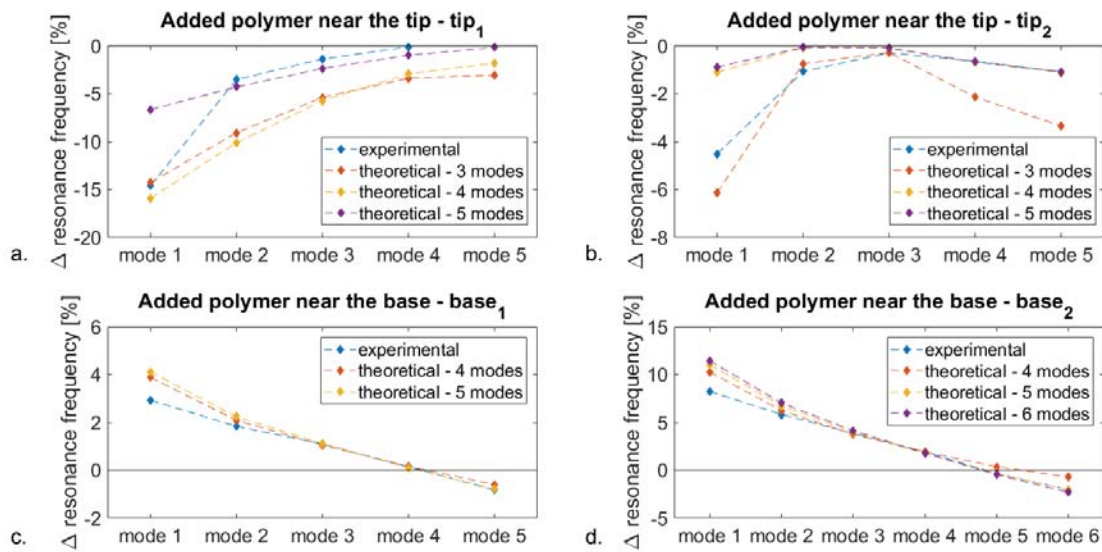


Figure 3.22: These figures show experimentally and theoretically derived resonance frequency shifts per mode. The theoretical values are obtained by combining the first three, four, five or six flexural modes. The lower modes resulted in infeasible values compared to the values from the literature. The dashed lines are added to guide the eye.

4

Discussion

During the experiments and the processing of the results, many obstacles were encountered. This chapter will debate on the used method and remarkable outcomes.

4.1. Deposition of a polymer

When investigating the deposited polymeric layer for all the four samples, it can be seen that delamination of layers and difficulties with the adhesion on the cantilever surface occurred.

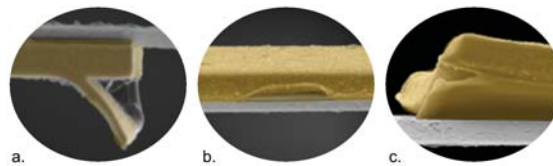


Figure 4.1: Delamination of layers occurred in sample tip_1 (a.), $base_1$ (b.) and $base_2$ (c.). It can even be seen that the polymeric layer is not fully adhered to the cantilever surface for sample $base_2$ (c.)

By fabricating the adhesive from lines drawn side by side, polymerized regions can be cross-linked. During the polymerization process, material slightly shrinks. Accordingly, cross-linking can cause an increase of in-plane shrinkage on the whole drawn structure, which can lead to residual stress causing an out-of-plane bending moment for multiple stacked layers. The writing process is followed by the developing process in PGMEA and di-propanol. Afterwards, while drying, the surface tension of the chemicals can be larger than the adhesive forces between the polymerized structure and the substrate. The fluids will stimulate delamination of the sheets. If this happens, the out-of-plane moment comes in. This effect can be seen from sample tip_1 as well (Figure 3.6 on page 33).

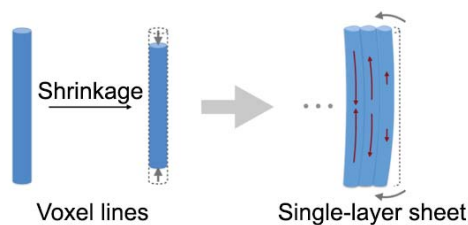


Figure 4.2: This image visualises the effect of shrinkage on voxel lines on the left-hand side. This causes a bending moment when multiple voxel lines are manufactured parallel and adjacent. [16]

Since an adsorbate induces surface stress to the resonator, it affects the resonance frequency [39]. For sample $base_2$, this surface stress will be lower because of the delamination.

4.2. Multi-modal analysis

4.2.1. Difference in amplitude of the peaks before and after deposition of material

The dynamic behaviour of microcantilever resonators is sensitive to many parameters. Deviations in the dimensions of the beam and impurities or cracks in the material will influence the results. Additionally, external aspects like the ambient temperature and pressure, and the humidity of the environment affect the performance of the system. As can be seen in the frequency response curves presented in Chapter 3, the amplitude of the peaks before and after deposition of material differ. Since the ambient temperature, pressure and moisture in the cleanroom of the TU Delft (SO class 7) are controlled, the affect is assumed to be negligible. The differences between peaks are explained through the effect of the clamping-induced damping and the laser spot orientation.

The magnitude that is measured depends on the cantilever slope in each mode. Therefore, the positioning of the laser is influencing the magnitude: when pointing the laser beam at the node of a flexural mode, the magnitude will be zero. This is showed experimentally in Figure 4.3. In the same manner, torsional modes will not be visible when measuring along the centreline of the cantilever as can be seen in Figure 4.4. The location of the peaks remained constant since the density of measured points on the cantilever surface was high enough and no aliasing occurred.

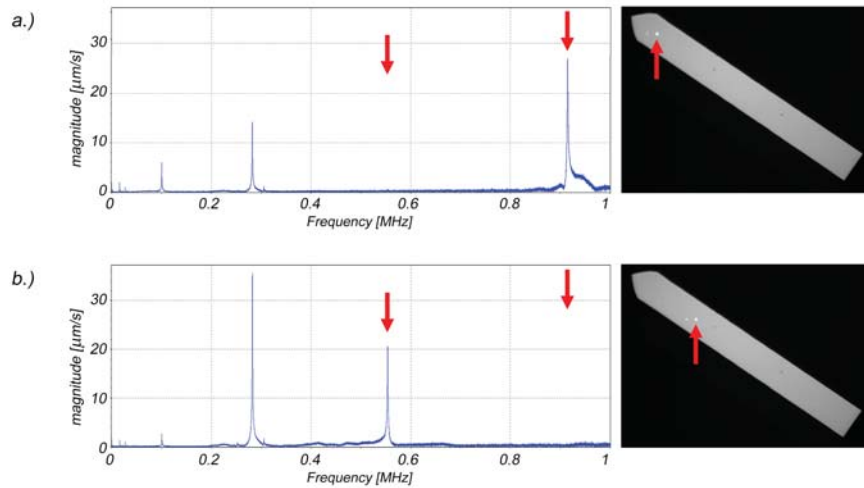


Figure 4.3: The location of the laser influences the results. As can be seen in picture a.), the fifth flexural mode is visible while the fourth flexural mode is not. Figure b.) on the other hand shows the fourth mode while the fifth mode is invisible. It can be concluded that the laser is pointed directly on a nodal point of an invisible node.

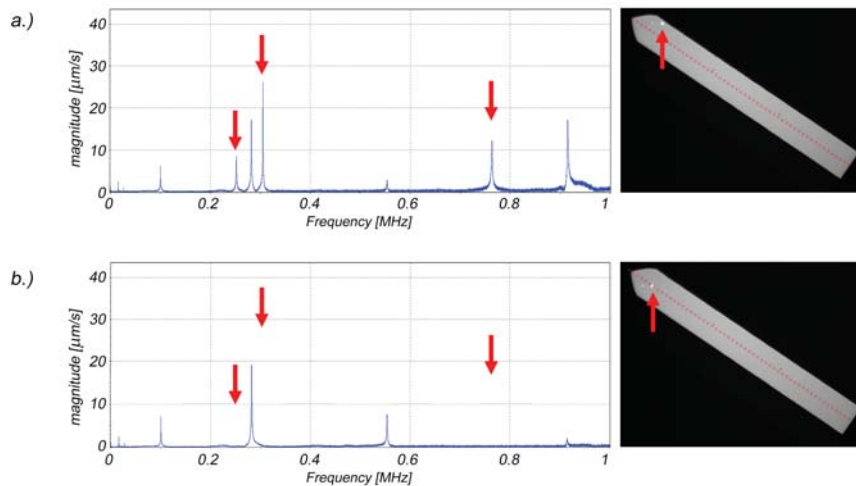


Figure 4.4: When the laser is not directed at the centreline of the cantilever, torsional modes will arise in the results. They are visible in picture a.). The difference with a measurement on the centreline is shown in picture b.). The peak that is pointed out with the most left red arrow is a combination of the first torsional mode and the second flexural mode. The red arrow in the middle shows the location of the first torsional mode and the most right arrow clarifies the second torsional mode.

While the laser spot orientation influenced the amplitude of the resonance peaks only, clamping leads to a shift of the peaks as well. This is due to an increase in damping, induced by the clamping. To investigate the impact of the clamping, one cantilever is clamped for ten times: the beam was clamped, measured and taken out of the setup for each time. The Q-factor is determined the PSV with software from Polytech: It curve-fits the selected peak with the -3 dB method¹. This enables the determination of the quality of the peak in a consequent way for all measurements.

The effect of the clamping is visualised with normal distribution plots of the deviation in Q-factor as shown in Figure 4.5. The deviations in Q-factor are low, indicating that the clamping entails a constant damping.

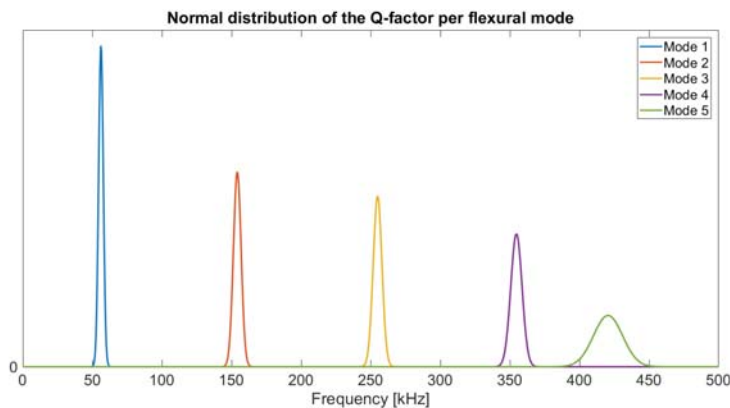


Figure 4.5: Tests on the clamping effect resulted in normal distributions of the Q-factor per mode as shown in this figure.

In this research, the variation in resonance frequency is important: it needs to be as low as possible. Figure 4.6 shows the normal distribution of the results from the clamping test. The standard deviation for the first resonance frequency is ~ 1.48 Hz. This amount increases when investigating higher flexural modes. Regardless of the variance in Q-factor for the second mode, the standard deviation of the resonance frequency is low. Comparing the variations to the measured frequency shifts in Chapter 3, the clamping effect was small compared to the changes in resonance frequency caused by an adsorbate.

¹The -3 dB method divides the resonance frequency, by the width of the frequency peak three decibels under the maximum peak height.

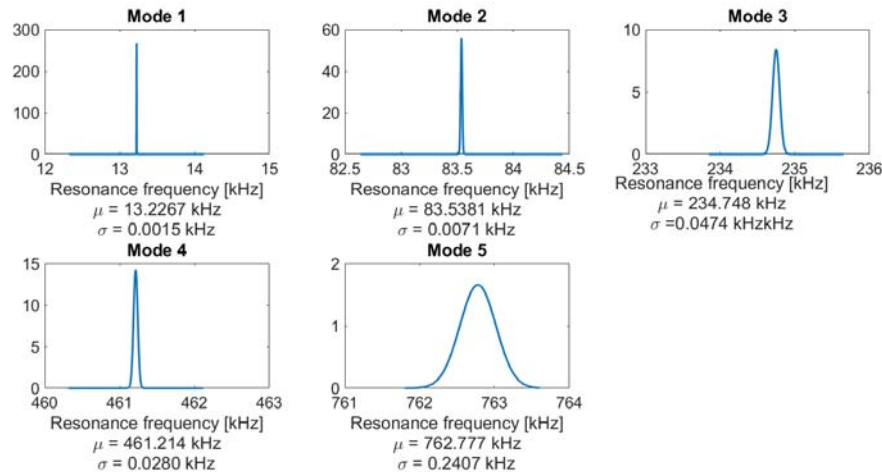


Figure 4.6: A normal distribution on the resonance frequency of a cantilever beam is shown for five bending modes. The variation increases for higher modes.

The raw data and whisker plots of the test can be found in Appendix I.

4.2.2. Differences in the resonance frequency shift between samples

Clear changes in the frequency response of the samples were measured. Figure 4.7 and 4.8 show the shift in frequency per mode for sample near the tip and base, respectively. It can be seen that the largest positive frequency shift contribution occur for thicker samples. A similar effect was shown by Sadeghian *et al.* [10] on uniform layers (Figure 1.8 on page 8), where the influence of the stiffness overshadows the mass effect for higher thickness ratios between the deposited layer and the cantilever.

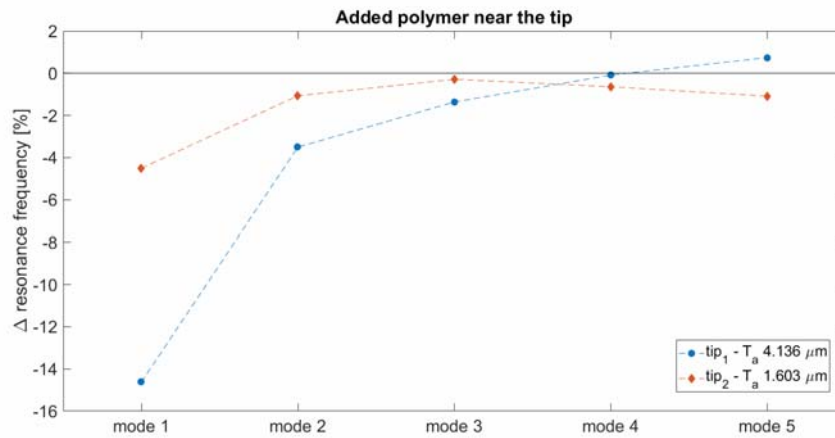


Figure 4.7: The frequency shift of two samples tip_1 and tip_2 caused by an adsorbate on similar locations but a different thickness are compared in this graph.

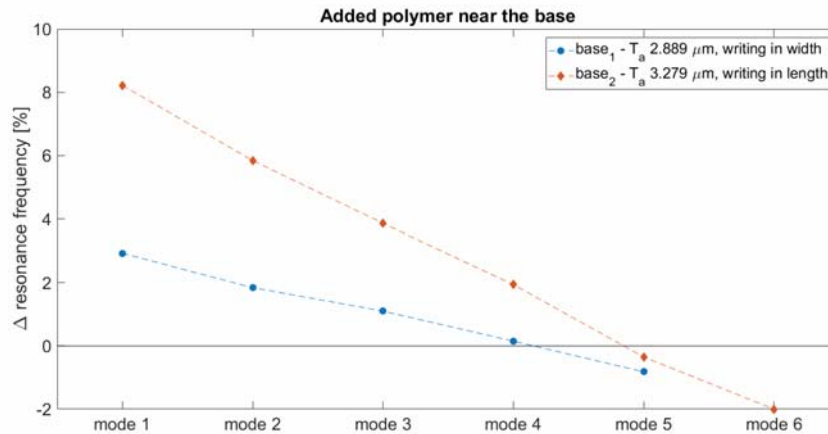


Figure 4.8: The frequency shift of samples base₁ and base₂ is shown in this figure. The changes caused by a polymer on similar locations, are compared in this graph.

The differences in stiffness effect for a polymeric layer located near the base, is influenced by the writing direction during the two-photon polymerization process as well. The adhesive in sample base₁ consists of voxel lines in the direction of the width of the cantilever, that make up the layers forming the adsorbate. In sample base₂, these strokes are directed in the length of the cantilever. When thinking of a mat which is used to roll sushi, one could imagine that it is easy to roll it in the direction perpendicular to the bamboo slats. The stiffness of the material does not affect the system. On the other hand, it would be hard to roll up the mat in the direction of the bamboo. This should be considered when comparing the results from sample base₁ and base₂.

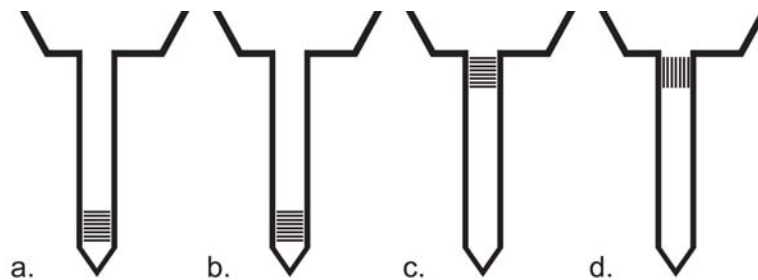


Figure 4.9: The writing directions during the two-photon polymerization process are shown in this graph. Sample tip₁ (a.), tip₂ (b.) and base₁ (c.) are written in the direction of the width of the cantilever. Sample base₂ (d.) is written along the length of the beam.

4.3. Theoretical model

In the model, it is assumed that the mode shapes do not differ after the addition of the polymeric layer. From Figure 6.43 it can be seen that the shapes slightly differ in amplitude. The nodes seem to be on the same location, but more points of the cantilever should be measured for a correct statement on this. From the available data it seems that the assumption on the mode shape will not affect the results considerably.²

²The mode shapes from other samples can be found in Appendix L

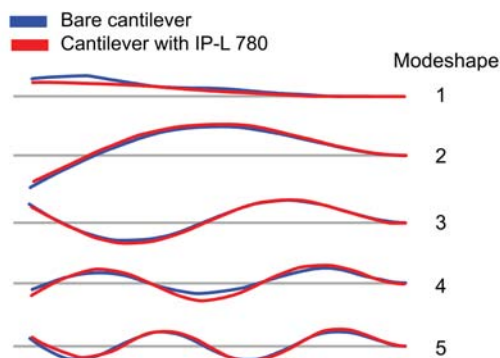


Figure 4.10: The experimentally derived mode shapes for sample tip_1 are shown in this figure. A blue coloured line represents the shape obtained for the bare cantilever and the red line shows the shape of the cantilever with a polymeric layer near the tip.

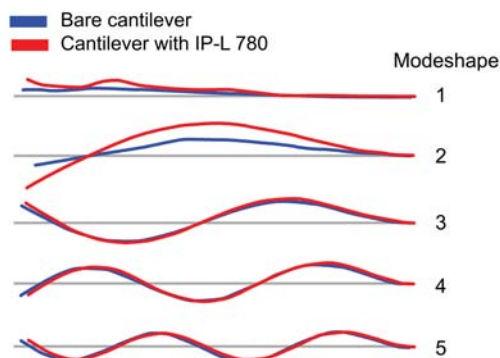


Figure 4.11: The experimentally derived mode shapes for sample $base_1$ are shown in this figure. A blue coloured line represents the shape obtained for the bare cantilever and the red line shows the shape of the cantilever with a polymeric layer near the base.

4.4. Decoupling of mass and stiffness

The disentanglement of mass and stiffness is done via three approaches: Via the frequency shift contribution of modes, via the absolute deflection and curvature of modes on the deposition location and via the combination of more than two modes. None of the methods resulted in a convergence to specific density and stiffness values. Although certain combinations of modes lead to infeasible results compared to the literature, a validation method for the exact properties of the samples is needed to make statements regarding the accuracy of the methods.

A research by Cross *et al.* was presented in the Introduction of this report. Within this research, the Young's modulus of multiple cells was determined via indentation: By indenting the samples a force, distance-curve is obtained, from which the Young's modulus can be obtained. In Appendix J, an experiment on obtaining a force-distance-curve on IP-L is described. Unfortunately, this did not lead to usable results.

All the derived material properties via the different methods, varied between the samples. External parameters as for instance temperature, humidity, laser intensity and exposure time, influence the two-photon polymerization process. The more the surrounding variables vary, the higher the likelihood for different power needs. Since the four introduced samples did not arise from the same batch, there is a chance of slight differences within the material properties. Furthermore, the difference between sample $base_1$ and $base_2$ can be explained through the writing direction as mentioned before. The effective stiffness is higher for a writing direction along the length of the cantilever. The effective stiffness is influenced by the adhesion as well. The theoretical model assumes a perfect contact between the polymeric layer and the cantilever surface. This cannot be quantified for the experimentally polymerized layers. Figure 4.12 shows possible configurations of the contact area, which influences the measured effective stiffness. Chen *et al.* [39] linked the adsorption-induced surface stress to the distortion in the cantilever's profile that arises when adding a substance. SEM pictures of the cantilever profiles before and after the deposition of the polymeric layer can be found in Appendix K.

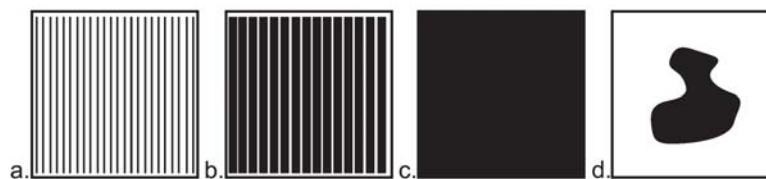


Figure 4.12: The quality of the adhesion of the polymeric layer on the cantilever surface is unknown. It could be the case that the layer is only adhered to the cantilever via the bottom of a voxel as shown in subfigure a. However, a contact area as shown in subfigure b. and c. are possible as well. Sample $base_2$ had shown detachment from the surface at many locations. Maybe the contact area will look like as sketched in subfigure d.?

5

Conclusion

The research question of this thesis is:

What is the effect of using multiple modes simultaneously for the decoupling of mass and stiffness, via a multi-modal analysis of a clamped-free micro-cantilever?

It can be concluded that the use of higher modes does affect the outcomes of the decoupling of mass and stiffness. Clear differences in feasible and infeasible results were obtained. What method will lead to an increase on accuracy, is yet elusive.

When reviewing the deposition method, it is shown that the usage of two-photon polymerization enables an accurate deposition location and control over the shape. However, the contact area is more difficult to control, due to the risk on delamination caused by cross-linking. The fabrication steps and the design of the structure can be adjusted such that the chance on delamination is minimised. Furthermore, little is known about the adhesion between silicon and IP-L 780.

The setup for the multi-modal vibration analysis combining piezoelectric actuation, clamping and laser Doppler vibrometry worked well. A high signal-to-noise ratio was obtained by using an average of 30 measurements. The clamping seemed to have a constant effect on the system: The variation in Q-factor and resonance frequency was small. The resolution of the measurements were small enough to certainly obtain the frequency shift induced by the polymeric layer.

The experimentally derived results were linked to theory to enable disentangling of mass and stiffness. A combination of an Euler-Bernoulli beam with Rayleigh's method was used for this. The outcomes gave a good indication of mass and stiffness properties compared to the values derived from the literature.

Since the resulting material properties can be linked to literature values only, no statements can be made regarding the accuracy of each combination of modes in various methods. Certain combinations of modes led to infeasible results such as negative density values. Therefore, higher modes definitely do have an affect on the disentanglement of mass and stiffness. Variations in thickness of samples, deposition locations on the cantilever and the quality of the adhesion between the added polymer layer and the cantilever surface have shown to influence the resonance frequencies.

6

Recommendations

After a thorough processing of the experimentally derived results, recommendations arose for further research.

First of all, the two-photon polymerization with the Nanoscribe has proven to be a promising method for material deposition on micro-resonators. The process steps are optimized and the results of this research has shown interesting effects. For stronger statements on the cause of the frequency shift, more data needs to be obtained. Hence, experiments with batches of cantilevers are recommended. When writing on multiple beams within a batch, the process parameters will be exactly the same, minimising the errors. The positioning and alignment are performed manually. When a simple holder can be developed that is attachable to the substrate, the alignment will be similar for each experiment.

As elaborated on in Chapter 4, delamination of the polymerized structure occurs if the adhesion force between the structure and the substrate is not large enough. By treating the substrate with chemicals, the adhesion can be improved. Nanoscribe GmbH recommends a treatment as described in Appendix M. On the other hand, this phenomenon could be used for other purposes as well. For example in a research of Bauhofer *et al.*[16] it is used for shape morphing. Biomimetic sheets *e.g.* for drag reduction can be produced in this way. Additionally, it would be interesting to investigate the adhesion force of a polymerised IP-L 780 structure on glass and silicon firstly, but other materials as well. This has not been quantified but could lead to insights useful for the fabrication of hydrophobic surfaces for example.

Furthermore it would be interesting to investigate the effect of the thickness ratio's on the frequency shift per mode. This is done for uniform layers only. Different lengths of layers will influence the frequency response as well, therefore further research in that area is recommended as well.

This research investigated the addition of material near the base and near the clamping of a resonator. What will the influence of other deposition locations be? Likewise, will similar effects occur when using different deposition materials? And an experiment on an added polymer with a writing direction along the length of the cantilever near the tip of the beam would be interesting. This would reveal more information about the accuracy of the measurements.

The indentation experiments did not lead to useful results. For stronger conclusions, a force, distance-curve needs to be obtained with an AFM probe with a blunt tip. The polymerization process is sensitive to many parameters. The values found in literature give an approximation on the order of magnitude of the material properties only, since the environmental parameters and the writing settings deviated from the parameters and settings for the experiments in this research. When obtaining the exact stiffness properties of the material that is added on the cantilever, statements can be made according to the accuracy of the method.

During the polymerization of IP-L 780, the double bonds from C=C bonds of the monomer are used for the cross-linking such that a polymer arises. RAMAN shifts give insight in amount of C=C bonds at 1635 cm^{-1} . Raman spectroscopy [80] uses the vibrational modes in a system to identify molecules. Red laser light is trained onto a material and interacts with the molecule. A change in the polarizability¹ of the molecule provokes a specific energy transaction, which correspond to the Raman bands. The energy level of the incident photon is shifted up or down with respect to the scattered photon. This energy shift in terms of wave numbers (cm^{-1}) is calculated through the wavelengths of the incident and Raman scattered photons. The energy

¹"Polarizability is an important fundamental property of particles. They determine dynamical response of a bound system to external perturbations, and provide valuable insight into internal strong interaction structure."[81]

transactions are induced by specific molecular vibrations and can therefore be used to identify molecules. The peak for a non-polymerized resin at this location will diminish after polymerization. Hence it forms a reference value [82] that could be used to compare different samples. Since a sputtered layer of conductive material is necessary for the examination on the dimensions of the added structure with an SEM, it is hard to compare the samples of this research. When using an ESEM, this option remains.

Appendix

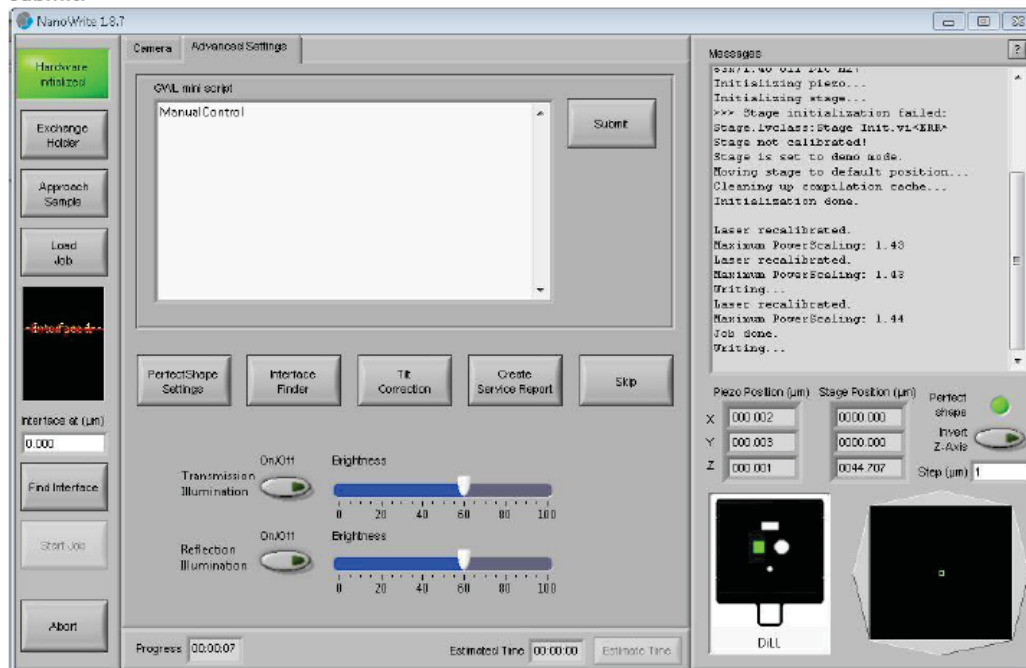
A. ManualControl Nanoscribe

How to use Manual Control

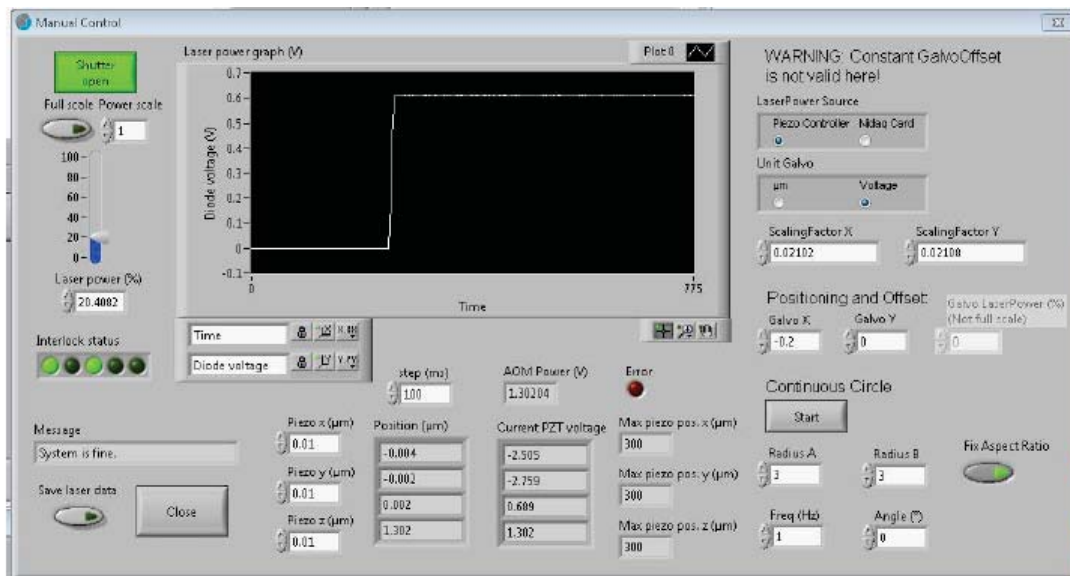
As preparation, please open NanoWrite and be sure the system is correctly initialized.

To use the interface finder in manual mode you can

- a) Go to the position where the interface is, this if you have observed in previous times where the interface position is.
 - b) Once on the region where the interface can be you can use the manual control window, described below.
- 1) Press on approach sample. This in case you haven't approached either manually or automatically.
 - 2) On the input window (mini script window) write the command ManualControl and click submit.



This will bring a window in which you will find a scale on the upper left side. This controls the laser power in percentage. At the same time, you also need to click on the button “Shutter Close/Open” to make it look green as on the next picture. You will see how on the black screen at the right side the diode voltage increases, if that happens then the laser is on and it is coming through to the substrate.



- a. Slowly increase the laser power until you see fluorescence. This could not happen if the focal point of the laser is inside the substrate. If that is the case, please move downwards with the microscope until seeing the fluorescence of the focal point.
- 3) Move the microscope up and down near to the interface position. You will notice that the fluorescence decreases and eventually disappears. This is because the laser spot is going in the substrate
 - a. That region where you are going in and out the substrate with the focal point is then the interface.
 - 4) leave the microscope in a position where the fluorescence starts to get strong, mainly just after getting out of the substrate.
 - 5) Delete all FindInterfaceAt commands from the script to be loaded.
 - 6) In this way, you can load any job and run it in the position you want.

B. Cantilever fabrication process

The fabrication process for the used cantilevers is as follows:

1. The AFM probes are produced from monocrystalline silicon wafers. [17] The material is built in a <100> plane.
2. An oxidation process is performed such that a layer of Silicon Dioxide (SiO_2) arises on both sides of the wafer.
3. A photoresist is deposited on one side.
4. Subsequently a photolithography process is started.
5. After developing the exposed photoresist, a mask is printed in the SiO_2 layer.
6. 7. 8. Thereafter the same procedure is performed on the other side of the wafer.
9. The SiO_2 that is not covered by the photoresist is removed via isotropic wet etching.
10. Afterwards, the photoresist is removed.
11. Anisotropic wet etching is performed to remove the parts of the silicon where it is not covered by the SiO_2 layer. This is done with potassium hydroxide (KOH) to obtain a high etch rate selectivity.
12. The wet etching step is performed until the SiO_2 for the tip forming falls down.
13. The SiO_2 that is left over is removed by isotropic wet etching.
14. One side of the formed cantilever, needs to be protected with a layer of Silicon Nitride (Si_3N_4).
15. The other side is anisotropic wet etched such that the required thickness of the cantilever can be acquired.
16. The layer of Si_3N_4 is removed by isotropic wet etching (16.).

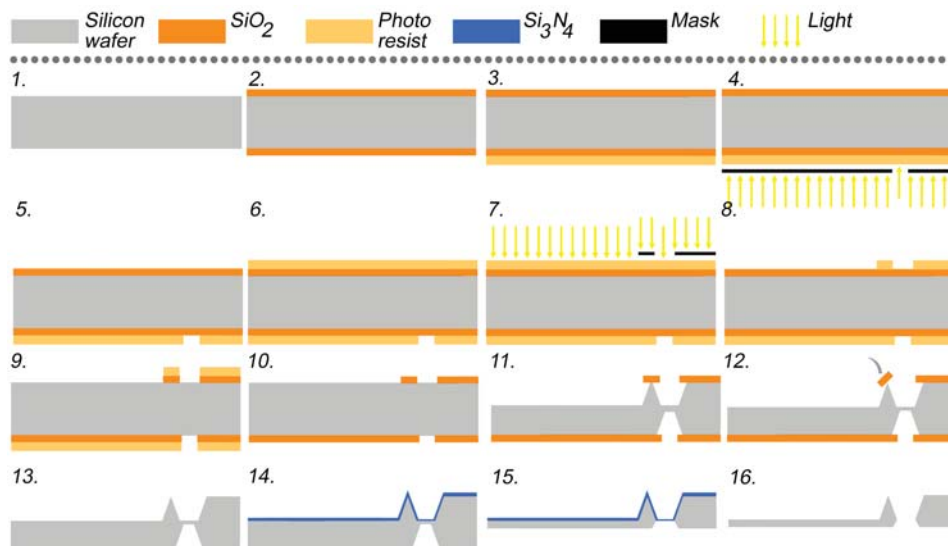


Figure 6.1: The process steps for the fabrication of AFM probes are shown in this figure. [17]

C. Determining mode shapes

The Euler-Bernoulli theory states that the equation of motion is as follows:

$$\rho A \frac{\partial^2 u(x, t)}{\partial t^2} + EI_y \frac{\partial^4 u(x, t)}{\partial x^4} = 0 \quad (6.1)$$

The material density is depicted as ρ , the cross sectional area is represented by A , E is the Young's modulus and I is the moment of inertia. The solution of this equation of motion,

$$u(x, t) = \sum_{n=1}^{\infty} \psi_n(x) \cos(\omega t), \quad (6.2)$$

is position and time dependent. In order to separate these variables, the Reduced Order Method [ROM] can be used. The method only takes a few solution into account, the eigenfrequencies in this case. Every eigenmode is depicted via modal number n , the frequency of motion is described by ω . The displacement function ($\psi_n(x)$) is formulated as

$$\psi_n(x) = \underbrace{a_n \cos(\beta_n x) + b_n \sin(\beta_n x)}_{\text{Represents standing waves in the beam centre}} + \underbrace{c_n \cosh(\beta_n x) + d_n \sinh(\beta_n x)}_{\text{Represents the influence of the clamping}}, \quad (6.3)$$

in which β_n represents the wavenumber. This is a distinct spatial shape of a certain vibrational mode. The frequency depends on this wavenumber.

$$\omega = \beta_n^2 \sqrt{\frac{EI_y}{\rho A}} \quad (6.4)$$

In order to calculate the wavenumber, the boundary conditions for a cantilever clamped at $x=0$ and free at $x=L$ have to be taken into account. These conditions are

$$\begin{aligned} \psi_n(0) = 0; \quad \frac{\partial}{\partial x} \psi_n(0) = 0 \\ \frac{\partial^2}{\partial x^2} \psi_n(L) = 0; \quad \frac{\partial^3}{\partial x^3} \psi_n(L) = 0, \end{aligned} \quad (6.5)$$

since the displacement and slope at the fixed end are vanished due to the clamping and there is no bending moment and shear force at the free end of the cantilever. When substituting the boundary conditions in the displacement function, a system of four equations will be the result:

$$\begin{bmatrix} 1 & 0 & 1 & 0 \\ 0 & 1 & 0 & 1 \\ -\cos(\beta_n L) & -\sin(\beta_n L) & \cosh(\beta_n L) & \sinh(\beta_n L) \\ \sin(\beta_n L) & -\cos(\beta_n L) & \sinh(\beta_n L) & \cosh(\beta_n L) \end{bmatrix} \begin{bmatrix} a \\ b \\ c \\ d \end{bmatrix} = \begin{bmatrix} 0 \\ 0 \\ 0 \\ 0 \end{bmatrix} \quad (6.6)$$

By setting the determinant to zero², a non-trivial solution will become:

$$\cos(\beta_n L) \cosh(\beta_n L) + 1 = 0 \quad (6.7)$$

When solving this equation, the roots of Equation 6.4 are

$$\lambda_n = \beta_n L = 1.8751, 4.6941, 7.8548, (2n-1)\pi/2. \quad (6.8)$$

From equation 6.3 and 6.5, the displacement function can be updated to

$$\psi_n(x) = a_n \left[\cos(\beta_n x) - \cosh(\beta_n x) - \frac{\cos(\beta_n L) + \cosh(\beta_n L)}{\sin(\beta_n L) + \sinh(\beta_n L)} (\sin(\beta_n x) - \sinh(\beta_n x)) \right]. \quad (6.9)$$

With this equation, the five first mode shapes can be plotted. They are presented in Figure 6.2. The more precise the mode shapes can be computed, the smaller will the error of the resulting eigenfrequencies be.

²Trigonometry: $\cosh^2(x) - \sinh^2(x) = 1$ [83]

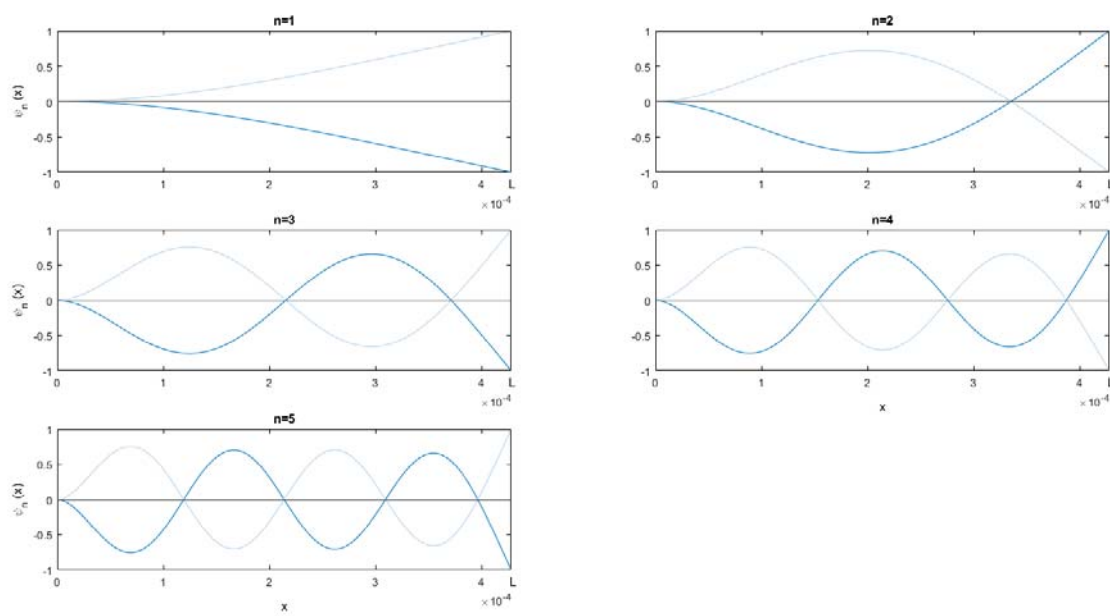


Figure 6.2: The $U_n(x), x$ -graphs represent a side-view of the first five mode shapes (n) of a cantilever. The cantilever is clamped at $x=0$ and has a length L .

D. Results desktop printer

Initial experiments were performed with polystyrene beads with a diameter of $5\ \mu\text{m}$. It can be stated that the used beads are rather big compared to the opening of the nozzle. When making small droplets of a concentration of 1% polystyrene beads in water, with the usage of a syringe (needle with a diameter of $0.15\ \text{mm}$) on a glass plate, it became visible that beads agglomerate. This can be seen in Figure 6.3. This is due to the evaporation of the water which causes a so-called coffee stain effect. Since the particles are spread quite well, there is a chance that the particles were correctly mixed with the water. Unfortunately when printing the solution of beads, the nozzle clogged. This could be due to particles that sediment out of the solution, a too high concentration of particles or a too large size of the beads.

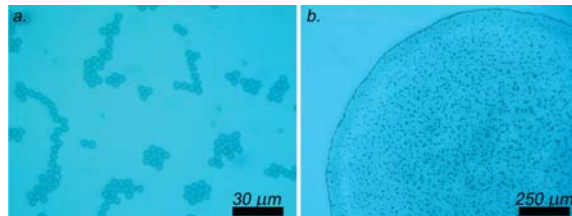


Figure 6.3: Polystyrene beads of $\sim 5\ \mu\text{m}$ in a water droplet. The agglomeration of beads is clearly visible a. within the droplet and b. on the edge of the droplet. The agglomeration on the side is caused by the evaporation of the water. The amount of evaporation over the surface of the droplet is equal, which causes the droplet to shrink. Accordingly, the outer particles are pushed to the inside, resulting in the 'coffee stain effect'.

Figure 6.4 shows the result of 40 small sized droplets of the solution printed on a specific location using an EPSON desktop ink-jet printer [Epson Stylus SX235W].

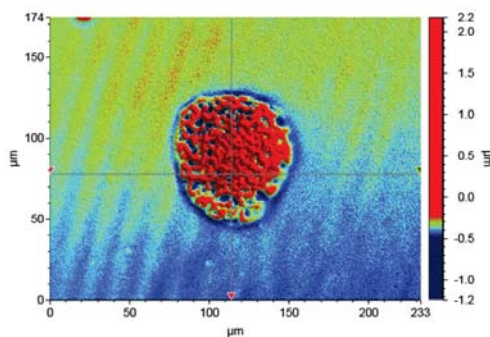


Figure 6.4: A white light interferometer picture of 40 small-sized droplets of PEDOT:PSS printed on glass with an EPSON Stylus SX235W desktop printer.

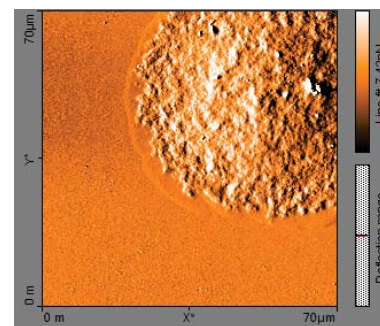


Figure 6.5: An AFM picture of 40 small-sized droplets of PEDOT:PSS printed on glass with an EPSON Stylus SX235W desktop printer.

Since the desktop printer is a black box, the difference between small, medium and large droplets are unknown but clear differences are detected. Logically, a variation in current that drives the piezoelectric nozzles is the cause of the difference in size but the amount of current is unrevealed. A horizontal and vertical spread of $\pm 80\ \mu\text{m}$ is visible. The height is not trustworthy because of the use of a white light interferometer for the evaluation of PEDOT:PSS which is slightly see-through: both the bottom and the top of the droplets are detected, which distorts the measurement. The same problem was obtained earlier with the polystyrene beads. An AFM measurement resulted in a height difference of $\pm 0.4\ \mu\text{m}$ (Figure 6.5). The droplets shown in the two figures are from the same batch of droplets. The batch is shown in Figure 6.6.

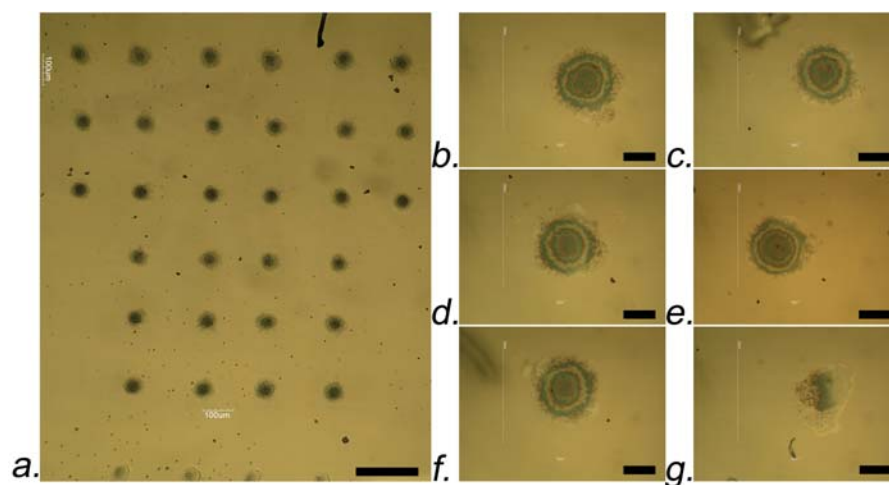


Figure 6.6: Results obtained when printing 40 small sized droplets of PEDOT:PSS in water printed on a specific location using an EPSON desktop ink-jet printer [Epson Stylus SX235W]. The scale-bar in picture a. depicts a length of 200 μm, for b. to g. it represents 30 μm.

The result for 150 medium-sized droplets deposited on glass using an EPSON desktop printer [EPSON XP-235], can be seen in Figure 6.7. Compared to the previous printer, the deposition was slightly more precise with a variation of $\pm 60 \mu\text{m}$.

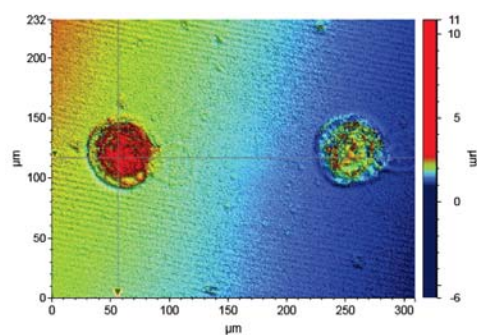


Figure 6.7: A white light interferometer picture of 150 medium-sized droplets of PEDOT:PSS printed on glass with an EPSON XP-235 desktop printer.

E. Results Nanoscribe

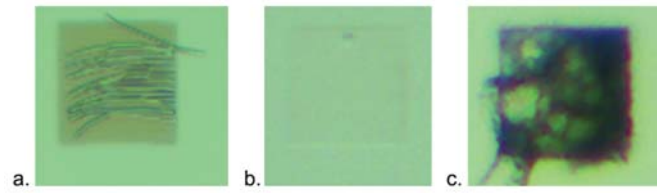


Figure 6.8: This figure shows three different results when writing cubes of $50 \times 50 \mu\text{m}$ with different settings on a glass substrate. Subfigure a. has too large hatching and slicing distances. Separate voxel lines are visible. Subfigure b. and c. have a too low and too high laser power, respectively.

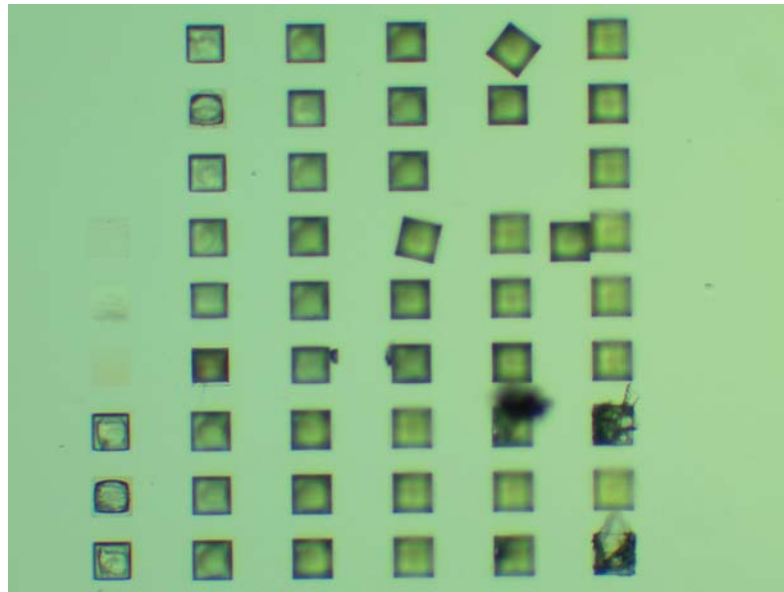


Figure 6.9: For the investigation on the right settings, print jobs like the one in this figure were performed. The columns show an increase in laser power, the rows an increase in scan speed.

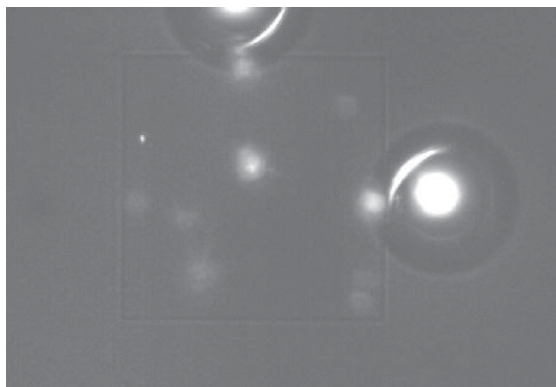


Figure 6.10: When writing over a polymerized part, bubbles arise as shown in this figure. By stopping the process, the bubbles often disappear. The picture is taken by a camera within the Nanoscribe system.

F. Optimization results

F.1. Modal analysis

Polymeric layer near the tip



Figure 6.11: An SEM image of a second sample with a polymeric layer near the tip of a cantilever can be seen in this figure. Its thickness is smaller than that of the cantilever. Contamination on the bottom side of the cantilever is revealed by this picture.

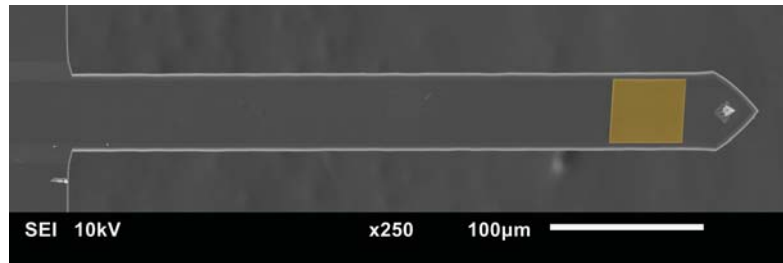


Figure 6.12: An SEM picture of sample tip₂. The added polymer is located near the tip of the cantilever.

A different sample with added material near the tip shows the results as can be looked into via Figure 6.13 and Table 6.1. The decrease in resonance frequencies clearly show the mass effect of the adhesive.

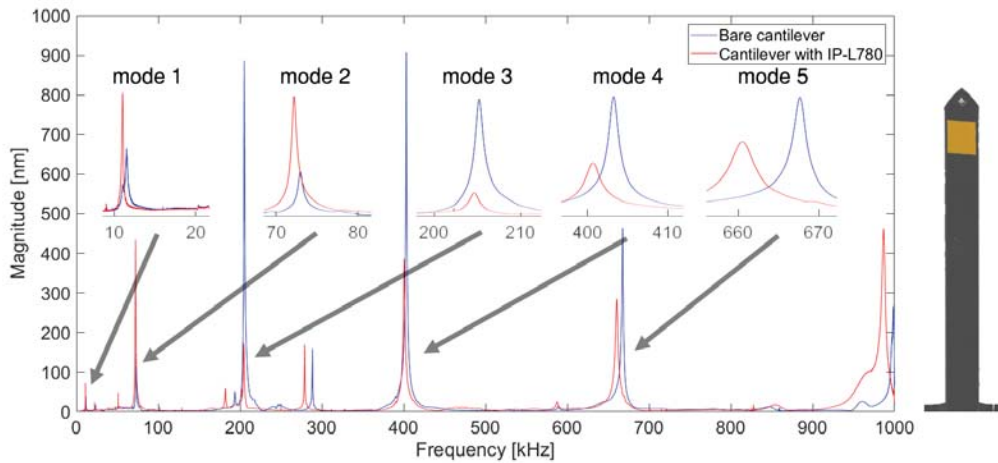


Figure 6.13: The blue line in this figure represents the frequency response of a bare cantilever. A fake coloured orange cube IP-L 780 ($\pm 50 \times 50 \times 3 \mu\text{m}$) is added near the tip. (sample tip₂)

Polymeric sample near the base

Another sample with an adhesive near the clamping shows a clear stiffness effect as well. Clear shifts are shown in Figure 6.17 and Table 6.2. And likewise in sample base₂, a change in sign arises at the fifth mode.

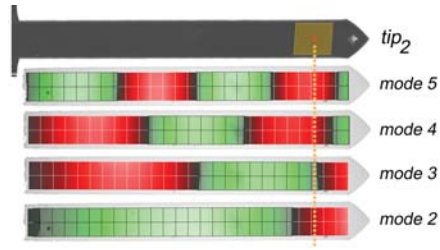


Figure 6.14: In this figure, the location of the centre of mass is compared with the operational deflection shape per mode for sample tip₂.

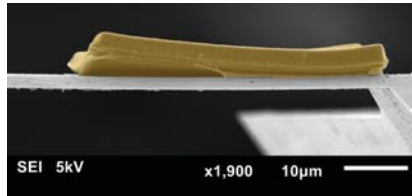


Figure 6.15: This picture shows the side of the added material on the cantilever (sample base₂). As can be seen, the adhesive forces between the added layer and the cantilever were not strong enough, resulting in a release of material at multiple locations.

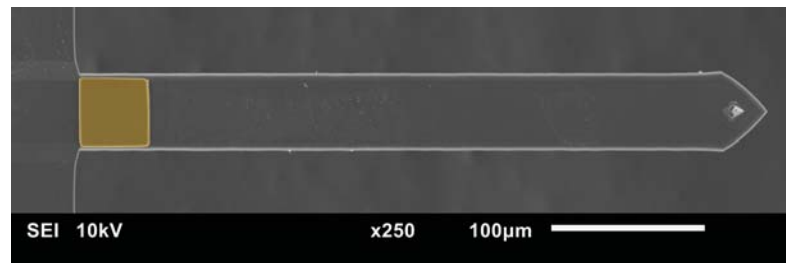


Figure 6.16: An SEM picture of sample base₂. The added polymer is located near the base of the cantilever.

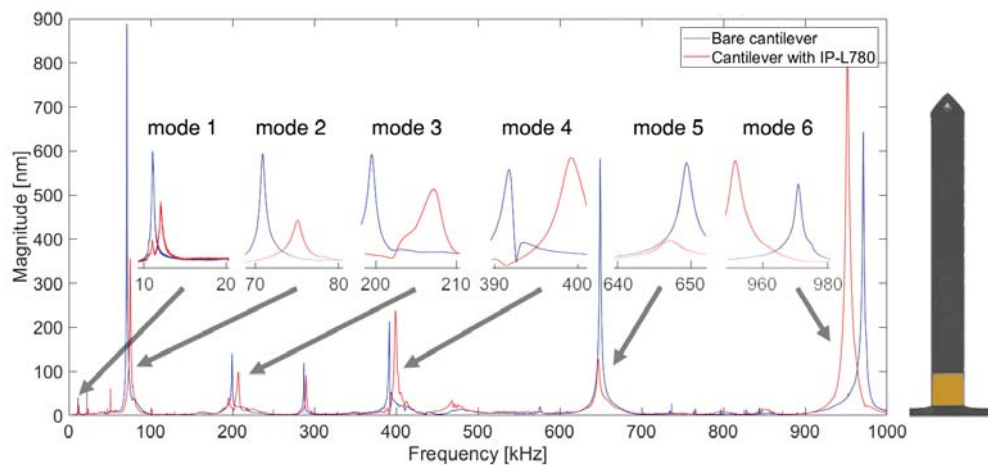


Figure 6.17: This graph figures the frequency response of a bare cantilever represented by the blue line. The added cube IP-L 780 ($\pm 50 \times 50 \times 3 \mu\text{m}$) is deposited near the clamping and highlighted with a fake colour (orange). The material is deposited in lines over the length of the cantilever. (sample base₂)

Table 6.1: The measured frequencies of sample (sample tip₂) before and after the deposition of material on beam tip₂ and the exact change and the difference in percentage.

Mode number	1	2	3	4	5
f before [kHz]	11.52	72.99	205.2	403.3	667.7
f after [kHz]	11	72.21	204.6	400.7	660.4
Δf [kHz]	-0.52	-0.78	-0.6	-2.6	-7.3
Δf [%]	-4.51	-1.07	-0.29	-0.64	-1.09

Table 6.2: sample base₂

Mode number	1	2	3	4	5	6
f before [kHz]	11.19	70.92	199.5	391.7	649.4	970.98
f after [kHz]	12.11	75.06	207.2	399.3	647.1	951.55
Δf [kHz]	+0.92	+4.14	+7.7	+7.6	-2.3	-19.43
Δf [%]	+8.22	+5.84	+3.86	+1.94	-0.35	-2.00

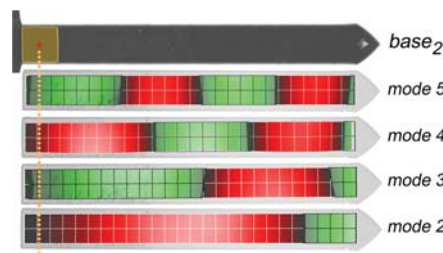


Figure 6.18: In this figure, the location of the centre of mass is compared with the operational deflection shape per mode for sample base₂.

F.2. Single-mode approach by using literature values

Ramos *et al.* [47] state that the mass of a material should be determined by a deposition near the free end of a cantilever. The stiffness properties should be quantified via a position near the base. Therefore, the density of the polymeric layer in this research is calculated from a given value as discussed in section 3.4.1 for the stiffness for a layer near the tip of a beam. Similarly, the Young's modulus of the added polymer is computed from a density value from literature for samples near the base.

Figure 3.17 shows the corresponding densities of a polymer near the tip for each mode when inserting a Young's modulus of 1, 1.5 or 2 GPa in the model. It can be seen that the sensitivity on the first two modes is rather small. A robust density is found in the first mode. Furthermore, no consistent value for the density can be obtained when looking at other modes. No specific value for the Young's modulus can be obtained.

Samples base₁ and base₂ are examined by substituting values of 1000 and 2000 kgm⁻³ for ρ , the corresponding Young's moduli can be obtained. The results for sample base₁ are shown in Figure 3.18 and the outcomes for specimen base₂ in Figure 6.22. For both cases, the sensitivity of E on ρ increases for higher modes. The obtained Young's moduli for beam base₁ tend to a decrease after mode 4. It is interesting to see this happening for the results of sample base₂ after the third mode, linearly. Although this trend is not as clear for sample base₁, the blue curve for a ρ of 1000 kgm⁻³ tends to decrease as well.

wat is deze tekst

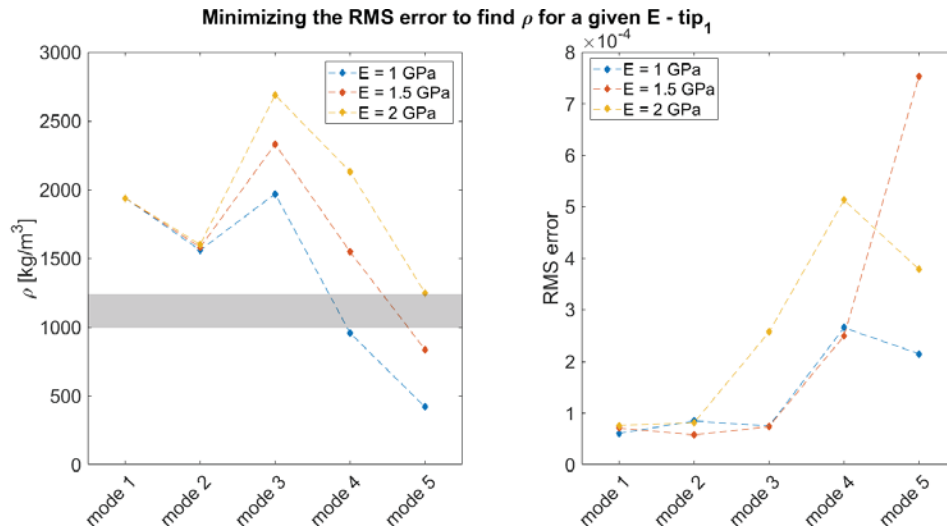


Figure 6.19: The left graph shows the ρ of the added material of sample tip₁ per mode, that corresponds to a Young's modulus of 1 (blue line), 1.5 (orange line) or 2 GPa (yellow line). The right graph shows the corresponding error between the experimental and theoretical values that is minimised. The grey area represents the values from literature.

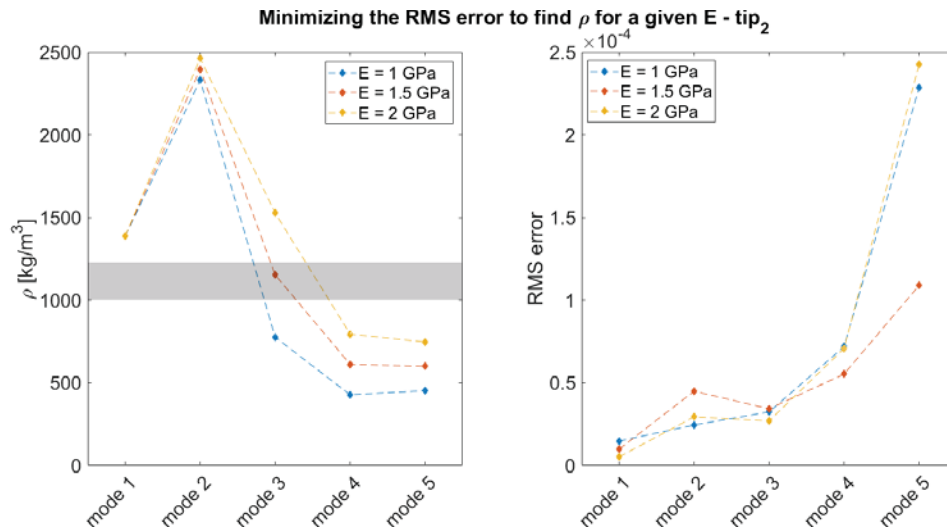


Figure 6.20: The ρ of the adsorbate of sample tip₂ that corresponds to a Young's modulus of 1 (blue line), 1.5 (orange line) or 2 GPa (yellow line) per mode is shown in the left graph. The grey area represents the values from literature. The right graph gives information on the corresponding error between the experimental and theoretical values that is minimised.



Figure 6.21: In the left graph, the values for E can be obtained from corresponding densities of 1000 kgm^{-3} (blue line) and 2000 kgm^{-3} (orange line) per mode. The grey area represents the values from literature. The minimum difference found on the experimental and theoretical values are shown in the graph on the right.

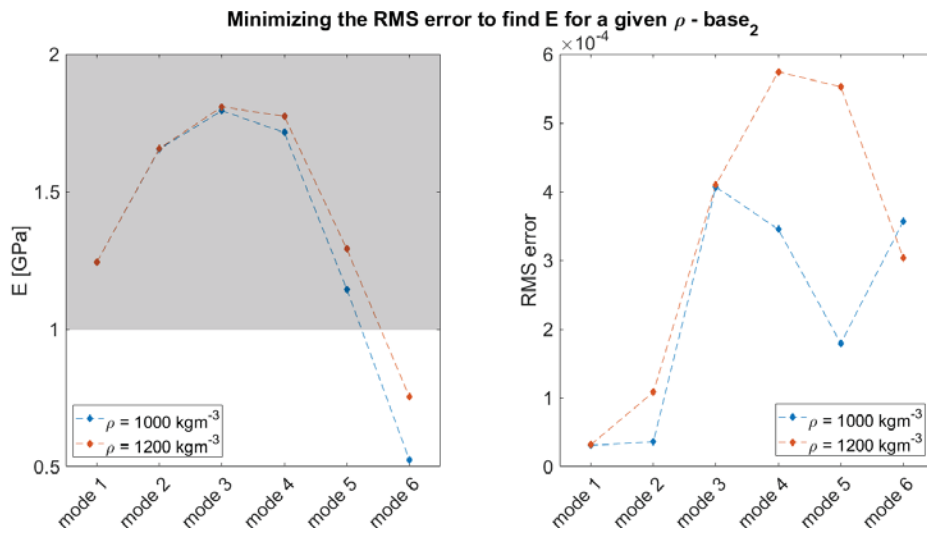


Figure 6.22: The Young's moduli that are related to densities of 1000 kgm^{-3} (blue line) and 2000 kgm^{-3} (orange line) per mode are shown in the left graph. The minimum variation found on the experimental and theoretical values are shown in the graph on the right. The grey area represents the values from literature.

E3. Single-mode approach by combining different locations

When using experimentally derived values only, a sample with a polymeric layer near the tip needs to be combined with a cantilever with a polymer near the base. Figure 6.23 shows fluctuating outcomes as a result.

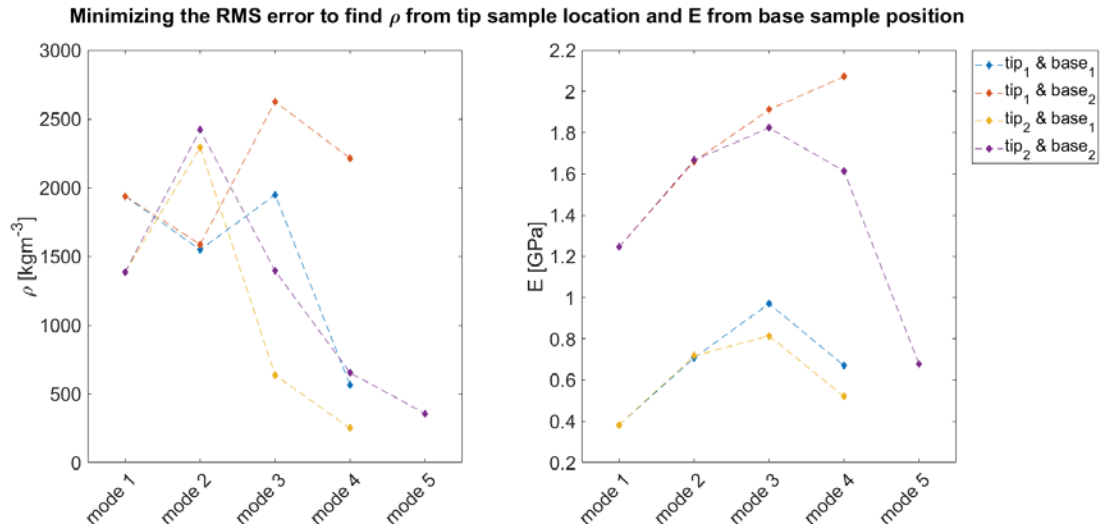


Figure 6.23: The outcomes from the combination of samples with a polymeric layer near the tip and samples with an added polymer near the base are shown in this Figure. The graph on the left-hand side shows the density values per mode, where the graph on the right shows the corresponding Young's moduli. No convergence was obtained when minimizing the RMS error for three combinations on mode 5 and are therefore missing.

F.4. Multi-mode approach by using literature values

The single-mode approach gave reasonable values when comparing them to literature. However, the outcomes still fluctuated and no conclusion can be made regarding the correct values. It is interesting to see what happens if multiple modes were investigated simultaneously. Figure 6.24 combines modes like was done by Amabili *et al.*. When looking at mode 1 and at a combination of the first five bending modes (mode 1-2-3-4-5), the density has a low sensitivity towards the Young's modulus and reaches a value close to the theoretical value. Unfortunately, the density values are not similar.³

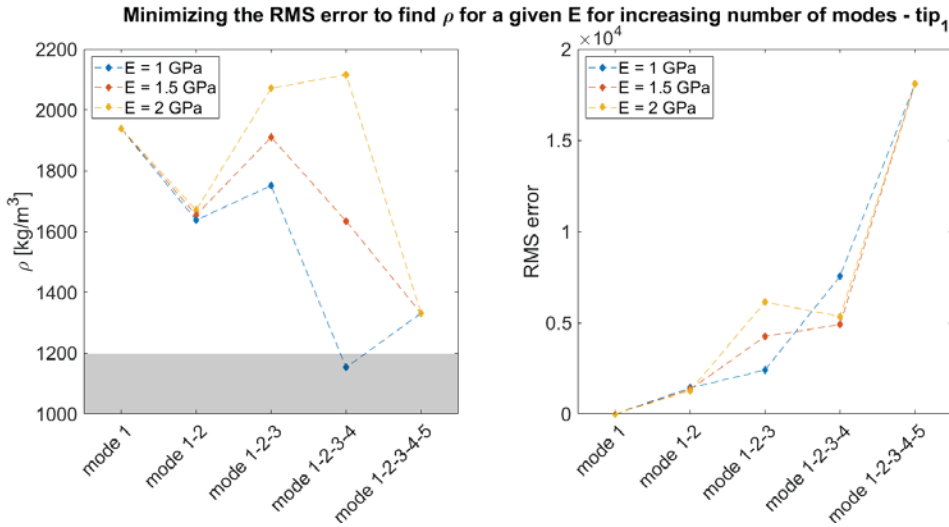


Figure 6.24: This graphs show the results of a multi-mode approach for sample tip₁. Young's moduli of 1 (blue line), 1.5 (orange line) or 2 GPa (yellow line) are used to obtain the density of the added polymer (graph on the left-hand side) and the corresponding RMS error (graph on the right-hand side). The grey area corresponds to the values for ρ from literature.

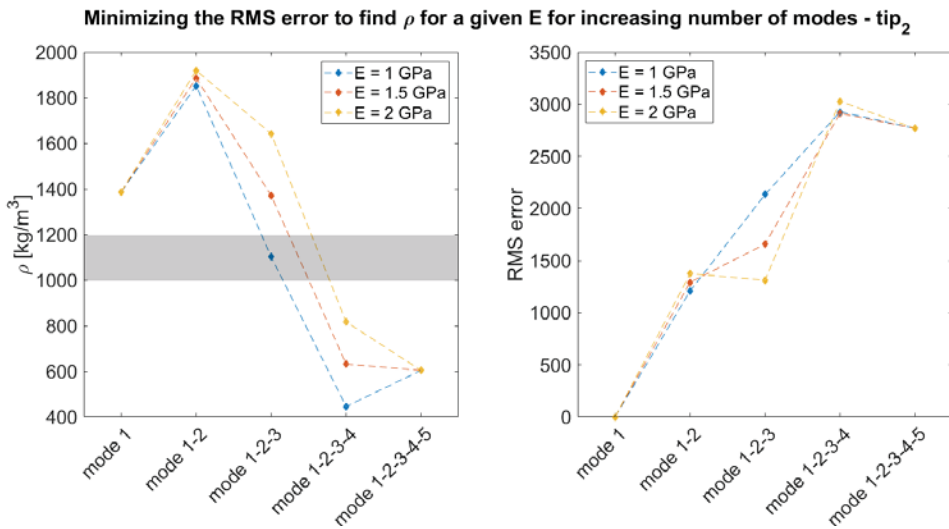


Figure 6.25: A multi-mode approach for sample tip₂ resulted in densities as shown on the left and RMS errors as presented on the left side of the figure. Young's moduli of 1 (blue line), 1.5 (orange line) or 2 GPa (yellow line) are used.

³The results from this approach for other samples can be found in Appendix F.3

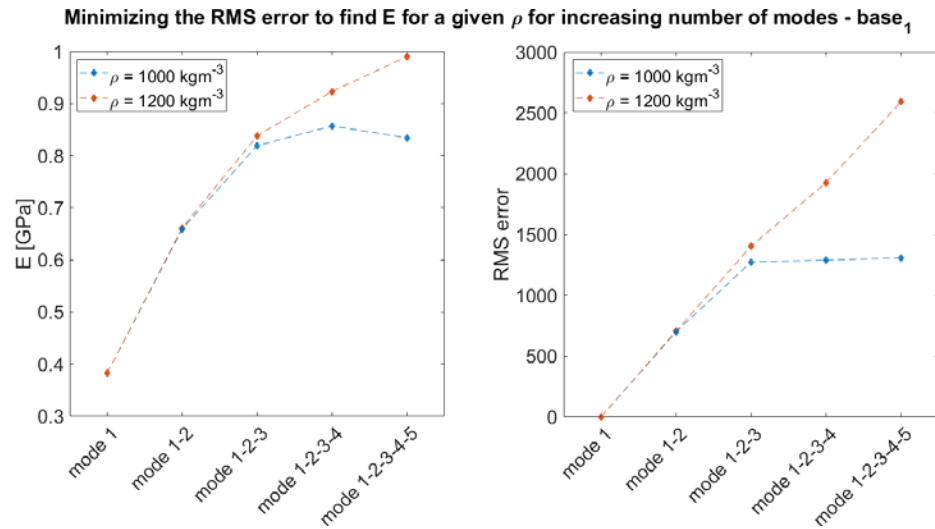


Figure 6.26: The graph on the left of this figure shows the Young's moduli corresponding to densities of 1000 (blue line) and 2000 kgm^{-3} (orange line). The second graph shows the RMS error.

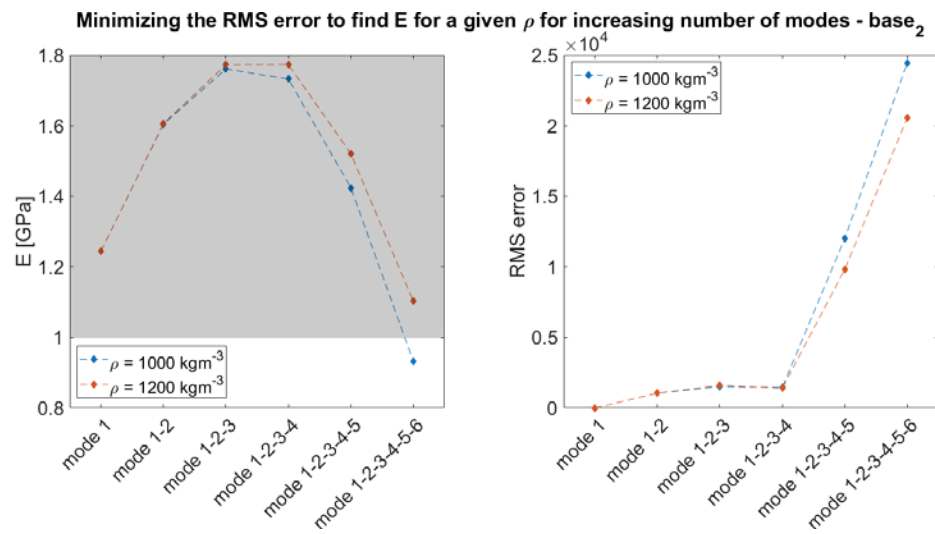


Figure 6.27: Densities of 1000 (blue line) and 2000 kgm^{-3} (orange line) are used for the obtaining of the Young's moduli. The corresponding RMS errors are plotted on the right-hand side. The grey area represents the values for E from literature.

E.5. Multi-mode approach by combining different locations

The Young's moduli were obtained from samples with an adhesive near the base and densities were acquired via tests with added material near the tip in a study of Ramos *et al.* [47]. Therefore, a different approach is introduced where the Young's moduli from beam base₁ or base₂ are combined with densities from sample tip₁ or tip₂ by minimising the RMS error. The results can be seen in Figure 6.28.

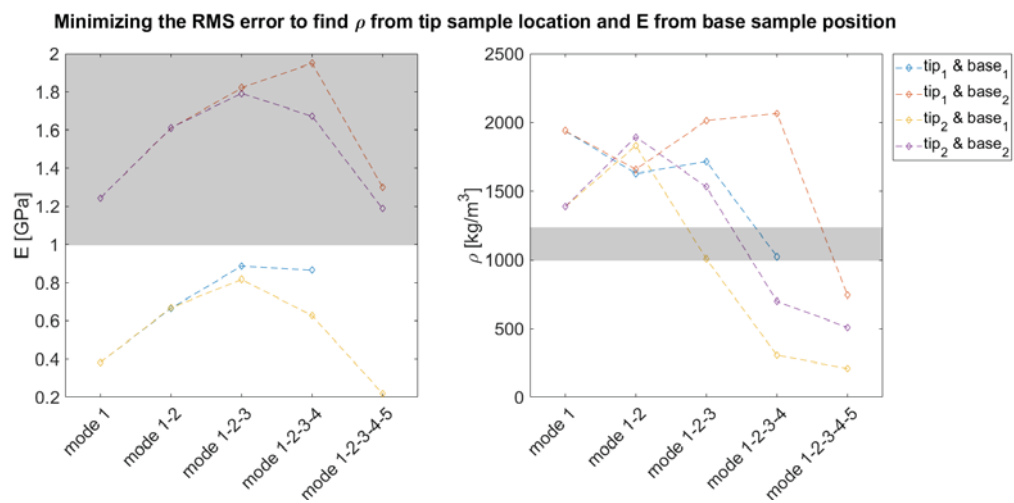


Figure 6.28: A recursive approach between two different samples has led to Young's moduli and values for the density of the added polymer. All the combinations are shown in this figure where the graph on the left shows the values for E and the most right graph shows the values for ρ . The grey areas represent the literature values.

E.6. Raw data of single- and multi-mode approach

Table 6.3: The raw data of single- and multi-mode method for sample tip₁ is presented in this table. The RMS value is minimized to find ρ for a given E .

		MULTIMODE METHOD - tip ₁					
		Minimizing the RMS value to find ρ for a given E					
mode	E=1GPa		E=1.5GPa		E=2GPa		
	rho	error	rho	error	rho	error	
1	1938,06	6,06176E-05	1938,36	7,11115E-05	1938,67	7,58763E-05	
2	1559,66	8,45413E-05	1580,09	5,74874E-05	1600,26	8,13589E-05	
3	1969,12	7,47398E-05	2330,98	7,38474E-05	2688,45	0,000257206	
4	956,303	0,000265429	1546,96	0,00024956	2130,44	0,000513102	
5	418,802	0,000214853	835,865	0,000752687	1247,86	0,000378489	
1&2	1637,64	1423,56	1653,81	1345,38	1669,8	1268,44	
1&3	1962	110,264	2244,08	1355,78	2527,98	2520,53	
1&4	1035,8	4278,73	1576,07	1593,09	2117,24	732,669	
1&5	402,766	7087,87	854,029	4900,83	1258,62	2909,69	
2&3	1745,6	2855,01	1922,73	5205,32	2099,15	7500,08	
2&4	1100,31	6289,87	1554,75	338,311	2007,5	5307,97	
2&5	402,766	13175,5	876,846	8674,18	1267,23	4028,18	
3&4	1160,18	9230,01	1705,51	7073,89	2243,79	4985,71	
3&5	402,766	14797,8	901,993	14689,2	1312,8	14051,3	
4&5	501,211	14454,1	946,488	18864,8	1387,07	23106,1	
1&2&3	1750,9	2405,42	1910,21	4247,89	2070,97	6133,84	
1&2&4	1067,74	5801,73	1559,36	1242,33	2053,9	4208,82	
1&2&5	439	11804,3	848,865	7672,76	1254,17	3833,48	
1&3&4	1091,09	7807,25	1642,06	5641,06	2189,91	3991,28	
1&3&5	437,631	13048,2	853,196	11932,6	1263,96	11056,6	
1&4&5	460,959	12479,1	890,414	15130,1	1315,53	18119,7	
2&3&4	1137,15	8315,03	1628,73	5580,86	2119,34	6140	
2&4&5	472,044	15107	897,257	15946,4	1318,05	18179,3	
3&4&5	470,959	16114	901,549	18309,2	1327,46	20756,1	
1&2&3&4	1153,11	7555,7	1634,1	4904,76	2116,58	5337,4	
1&2&3&5	453,481	14378,6	863,337	11775,6	1268,6	9912,16	
1&3&4&5	474,471	14700,8	903,73	16153,1	1328,6	18057,7	
2&3&4&5	485,333	16401,4	910,377	16706,2	1330,96	18094,5	
1&2&3&4&5	1330,96	18094,5	1330,96	18094,5	1330,96	18094,5	

Table 6.4: The raw data of single- and multi-mode method for sample tip₂ is presented in this table. The RMS value is minimized to find ρ for a given E .

		MULTIMODE METHOD - tip ₂					
		Minimizing the RMS value to find ρ for a given E					
		E=1GPa		E=1.5GPa		E=2GPa	
mode		rho	error	rho	error	rho	error
1		1386,87	1,48347E-05	1387,27	9,91E-06	1387,67	5,27022E-06
2		2330,81	0,000024451	2397,1	4,48977E-05	2462,97	2,93856E-05
3		776,399	3,23809E-05	1153,02	3,42922E-05	1527,21	2,69138E-05
4		427,901	7,18646E-05	611,99	5,52931E-05	794,888	7,07982E-05
5		452,088	0,000228337	599,878	0,000108879	746,712	0,000242386
1&2		1852,28	1209,07	1885,82	1291,98	1919,23	1374,15
1&3		947,431	1086,83	1217,59	411,552	1489,39	241,939
1&4		453,74	2014,68	632,679	1610,21	810,536	1217,22
1&5		460,297	1935,24	606,753	1615,03	752,276	1302,7
2&3		1180,55	2610,36	1476,31	2083,41	1770,25	1562,76
2&4		402,766	3565,58	653,998	3381,2	834,346	3154,17
2&5		466,379	3514,44	613,652	3357,51	759,958	3201,94
3&4		450,094	1453,56	646,645	2251,83	842,069	3041,64
3&5		458,996	1348,73	611,751	2296,54	763,589	3235,06
4&5		446,227	683,405	602,82	340,223	758,436	1345,57
1&2&3		1102,33	2133,9	1371,29	1657,89	1642,28	1312,25
1&2&4		439,468	3202,44	622,229	2901,6	803,84	2620,39
1&2&5		454,157	3160,74	601,77	2935,45	748,43	2723,79
1&3&4		438,407	1911,98	624,997	2126,5	810,482	2516,49
1&3&5		453,925	1847,02	602,334	2189,61	749,803	2714,02
1&4&5		449,066	1621,84	602,303	1295,93	754,595	1470,97
2&3&4		440,917	3009,86	628,062	3133,94	814,052	3374,03
2&4&5		449,461	2829,26	602,778	2658,27	755,146	2730,36
3&4&5		449,274	1191,2	603,254	1800,12	756,295	2710,03
1&2&3&4		445,297	2927,36	631,501	2912,68	816,596	3026,86
1&2&3&5		455,188	2882,18	603,555	2972,71	750,981	3207,2
1&3&4&5		449,953	1677,34	603,814	1905,38	756,739	2504,43
2&3&4&5		450,347	2615,75	604,288	2768,86	757,289	3199,05
1&2&3&4&5		604,288	2768,86	604,288	2768,86	604,288	2768,86

Table 6.6: The raw data of single- and multi-mode method for sample base₂ is presented in this table. The RMS value is minimized to find E for a given ρ .

		MULTIMODE METHOD - base ₂			
		Minimizing the RMS value to find E for a given ρ			
		$\rho=1000$		$\rho=1200$	
mode		E	error	E	error
1		1,24E+09	3,1E-05	1,24E+09	3,18E-05
2		1,65E+09	3,6E-05	1,66E+09	0,000108
3		1,79E+09	0,00041	1,81E+09	0,00041
4		1,71E+09	0,00035	1,77E+09	0,000574
5		1,14E+09	0,00018	1,29E+09	0,000552
6		5,25E+08	0,00036	7,54E+08	0,000304
1&2		1,6E+09	1050,56	1,61E+09	1054,57

1&3	1,77E+09	1433,49	1,78E+09	1470,18
1&4	1,7E+09	1229,03	1,76E+09	1379,14
1&5	1,15E+09	265,21	1,29E+09	122,635
2&3	1,75E+09	1373,74	1,77E+09	1498,68
2&4	1,7E+09	635,901	1,75E+09	1237,37
2&5	1,22E+09	5689,22	1,34E+09	4059,7
3&4	1,75E+09	1411,58	1,79E+09	624,88
3&5	1,34E+09	12795	1,44E+09	10154,2
4&5	1,37E+09	14287,9	1,49E+09	12024,4
1&6	1,22E+09	4,44E+04	1,22E+09	2,97E+04
2&6	1,65E+09	7,15E+04	1,65E+09	5,66E+04
3&6	1,79E+09	8,03E+04	1,81E+09	6,61E+04
4&6	1,71E+09	7,54E+04	1,77E+09	6,40E+04
5&6	1,14E+09	3,97E+04	1,29E+09	3,40E+04
1&2&3	1,76E+09	1519,35	1,77E+09	1608,41
1&2&4	1,71E+09	1062,43	1,76E+09	1424,43
1&2&5	1,18E+09	4423,3	1,31E+09	3458,1
1&3&4	1,74E+09	1522,3	1,78E+09	1202,61
1&3&5	1,28E+09	10251,4	1,4E+09	8141,99
1&4&5	1,35E+09	11617,1	1,46E+09	9785,6
2&3&4	1,73E+09	1357,46	1,78E+09	1199,66
2&4&5	1,36E+09	11917,6	1,47E+09	9917,3
3&4&5	1,42E+09	13712,1	1,52E+09	11275
1&2&6	5,6E+08	10252,7	7,82E+08	8109,85
1&3&6	6,62E+08	21720,4	8,68E+08	17919
1&4&6	7,58E+08	27502,7	9,55E+08	23376,2
1&5&6	7,13E+08	17957,2	9,17E+08	15387,2
2&3&6	6,87E+08	23445	8,89E+08	19231,3
2&4&6	7,79E+08	28634,8	9,71E+08	24189,6
2&5&6	7,32E+08	19820,5	9,32E+08	16729,2
3&4&6	8,48E+08	32755,9	1,03E+09	27553,3
3&5&6	7,96E+08	25919,5	9,86E+08	21718,6
4&5&6	8,57E+08	29797,8	1,04E+09	25382,2
1&2&3&4	1,73E+09	1455,26	1,77E+09	1392,96
1&2&3&5	1,3E+09	9305,8	1,42E+09	7304,59
1&2&4&5	1,36E+09	10323	1,47E+09	8598,07
1&3&4&5	1,42E+09	11898,9	1,52E+09	9776,16
2&3&4&5	1,42E+09	12012,2	1,52E+09	9821,92
1&2&3&6	6,88E+08	20329,3	8,89E+08	16667,1
1&2&4&6	7,79E+08	24812,8	9,72E+08	20954,6
1&2&5&6	7,32E+08	17190,3	9,33E+08	14498,8
1&3&4&6	8,49E+08	28376,5	1,03E+09	23865
1&3&5&6	7,96E+08	22461,7	9,86E+08	18814,6
1&4&5&6	8,58E+08	2,58E+04	1,04E+09	21984,6
2&3&4&6	8,66E+08	29046,6	1,04E+09	24344,8
2&3&5&6	8,12E+08	23417,2	9,99E+08	19507,9
2&4&5&6	8,71E+08	26536,7	1,05E+09	22487,6
3&4&5&6	9,20E+08	29394,9	1,09E+09	24791,3
1&2&3&4&5	1,42E+09	12012,2	1,52E+09	9821,92
1&2&3&4&6	8,66E+08	25987,3	1,04E+09	21777,1
1&2&3&5&6	8,12E+08	20956,7	9,99E+08	17452,9
1&2&4&5&6	8,72E+08	23742,8	1,05E+09	20115,9
1&3&4&5&6	9,20E+08	26296,8	1,09E+09	22175,4

2&3&4&5&6	9,32E+08	26780,6	1,10E+09	22511,8
1&2&3&4&5&6	9,32E+08	24451,5	1,10E+09	20551,4

Table 6.5: The raw data of single- and multi-mode method for sample base₁ is presented in this table. The RMS value is minimized to find E for a given ρ .

MULTIMODE METHOD - base ₁ Minimizing the RMS value to find E for a given ρ				
mode	$\rho=1000$		$\rho=1200$	
	E	error	E	error
1	3,82E+08	2,9E-06	3,82E+08	3,09E-06
2	7E+08	2,6E-05	7,03E+08	2,34E-05
3	8,58E+08	0,00015	8,82E+08	4,46E-05
4	8,82E+08	0,00014	9,78E+08	0,000247
5	8,12E+08	0,00028	1,05E+09	0,00024
1&2	6,59E+08	700,454	6,61E+08	706,053
1&3	8,3E+08	1070,82	8,52E+08	1123,54
1&4	8,63E+08	1124,1	9,56E+08	1338,51
1&5	8,01E+08	966,915	1,03E+09	1483,78
2&3	8,11E+08	1270,46	8,29E+08	1440,16
2&4	8,44E+08	1569,93	9,21E+08	2381,13
2&5	7,96E+08	1011,69	9,96E+08	3089,47
3&4	8,72E+08	331,147	9,41E+08	1352,6
3&5	8,26E+08	709,955	9,98E+08	2541,45
4&5	8,4E+08	1360,25	1,02E+09	1323,26
1&2&3	8,19E+08	1274,6	8,38E+08	1403,97
1&2&4	8,57E+08	1489,27	9,42E+08	2113,1
1&2&5	8,03E+08	1078,12	1,02E+09	2646,56
1&3&4	8,71E+08	896,843	9,43E+08	1471,16
1&3&5	8,2E+08	954,639	1,01E+09	2308,83
1&4&5	8,35E+08	1359,29	1,02E+09	1546,51
2&3&4	8,59E+08	1235,9	9,26E+08	2014,17
2&4&5	8,3E+08	1467,05	1,01E+09	2506,56
3&4&5	8,39E+08	1139,84	1E+09	2106
1&2&3&4	8,57E+08	1289,82	9,23E+08	1926,85
1&2&3&5	8,14E+08	1106,85	9,93E+08	2739,2
1&3&4&5	8,38E+08	1204,92	1E+09	2048,34
2&3&4&5	8,34E+08	1308,38	9,9E+08	2590,42
1&2&3&4&5	8,34E+08	1308,38	9,9E+08	2590,42

Table 6.7: This table presents the outcomes of a recursive method between samples tip_1 and $base_1$. The values for the density are derived from sample tip_1 and the Young's modulus from $base_1$.

RECURSIVE METHOD - tip_1 & $base_1$			
Minimizing the RMS value to find ρ from tip_1 and E from $base_1$			
mode	ρ	E	error
1	1937,67	382638000	3,01E-05
2	1547,6	707542000	8,45309E-05
3	1947,84	970792000	0,000193883
4	563,366	670755000	0,000314928
5	No convergence within range		
1&2	1626,74	666252000	2194,45
1&3	1924,71	933604000	1375,77
1&4	No convergence within range		
1&5	No convergence within range		
2&3	1700,44	872813000	4112,25
2&4	935,118	818632000	9834,75
2&5	No convergence within range		
3&4	1031,91	883315000	10237,3
3&5	No convergence within range		
4&5	No convergence within range		
1&2&3	1715,15	887152000	3766,26
1&2&4	876,338	804153000	8963,15
1&2&5	No convergence within range		
1&3&4	914,99	840537000	9389,9
1&3&5	No convergence within range		
1&4&5	No convergence within range		
2&3&4	998,035	858606000	10662
2&4&5	No convergence within range		
3&4&5	No convergence within range		
1&2&3&4	1023,46	864772000	9918,75
1&2&3&5	No convergence within range		
1&3&4&5	No convergence within range		
2&3&4&5	No convergence within range		
1&2&3&4&5	No convergence within range		

Table 6.8: This table presents the outcomes of a recursive method between samples tip_1 and $base_2$. The values for the density are derived from sample tip_1 and the Young's modulus from $base_2$.

RECURSIVE METHOD - tip_1 & $base_2$			
Minimizing the RMS value to find ρ from tip_1 and E from $base_2$			
mode	ρ	E	error
1	1938,21	1,245E+09	4,25E-05
2	1586,55	1,66E+09	0,000254632
3	2625,33	1,911E+09	0,000441721
4	2212,87	2,071E+09	0,000303559
5	No convergence within range		
1&2	1657,32	1,609E+09	2392,24
1&3	2450,66	1,864E+09	3910,64
1&4	2142,39	2,023E+09	2914,47
1&5	No convergence within range		
2&3	2032,2	1,81E+09	8652,28
2&4	1939,98	1,925E+09	7934,57
2&5	313,587	789000000	27057,2
3&4	2250,06	2,006E+09	8433,17
3&5	578,049	1,11E+09	33607,4
4&5	674,436	1,194E+09	34187,6
1&2&3	2013,01	1,82E+09	7439,86
1&2&4	2027,61	1,973E+09	7237,54
1&2&5	No convergence within range		
1&3&4	2189,97	2E+09	7025,97
1&3&5	362,08	909713000	30359,7
1&4&5	528,945	1,079E+09	28854,8
2&3&4	2073,91	1,954E+09	9427,96
2&4&5	586,64	1,134E+09	31326,8
3&4&5	699,935	1,265E+09	34656,3
1&2&3&4	2065,78	1,949E+09	8380,94
1&2&3&5	452,048	997561000	29292,3
1&3&4&5	705,109	1,268E+09	30435,9
2&3&4&5	739,225	1,298E+09	31361,4
1&2&3&4&5	743,621	1,3E+09	28363,8

Table 6.9: This table presents the outcomes of a recursive method between samples tip_2 and $base_1$. The values for the density are derived from sample tip_2 and the Young's modulus from $base_1$.

RECURSIVE METHOD - tip_2 & $base_1$			
Minimizing the RMS value to find ρ from tip_2 and E from $base_1$			
mode	ρ	E	error
1	1386,37	382487000	2,74083E-05
2	2293,14	717318000	4,40976E-05
3	636,188	814688000	8,23338E-05
4	250,065	520063000	7,37943E-05
5	No convergence within range		
1&2	1829,97	668574000	1877,39
1&3	846,941	812919000	2375,83
1&4	284,946	530979000	2757
1&5	No convergence within range		
2&3	1072,3	817780000	4135,8
2&4	319,827	582272000	5007,48
2&5	No convergence within range		
3&4	305,95	635145000	4102,97
3&5	No convergence within range		
4&5	158,151	88321100	15454,6
1&2&3	1005,59	817448000	4135,8
1&2&4	273,709	549237000	4623,96
1&2&5	No convergence within range		
1&3&4	295,076	617926000	4616,8
1&3&5	No convergence within range		
1&4&5	No convergence within range		
2&3&4	300,502	626879000	5699,27
2&4&5	No convergence within range		
3&4&5	198,128	191021000	15189,8
1&2&3&4	305,846	627493000	5367,57
1&2&3&5	No convergence within range		
1&3&4&5	199,485	192547000	13863,2
2&3&4&5	207,429	217202000	14842,3
1&2&3&4&5	208,728	218569000	13651

Table 6.10: This table presents the outcomes of a recursive method between samples tip_2 and $base_2$. The values for the density are derived from sample tip_2 and the Young's modulus from $base_2$.

RECURSIVE METHOD - tip_2 & $base_2$			
Minimizing the RMS value to find ρ from tip_2 and E from $base_2$			
mode	ρ	E	error
1	1387,07	1,244E+09	2,50183E-05
2	2419,08	1,666E+09	0,000071409
3	1394,74	1,823E+09	8,46838E-05
4	653,663	1,614E+09	0,000693843
5	356,125	677078000	0,000376499
1&2	1893,24	1,611E+09	2378,73
1&3	1375,46	1,791E+09	1531,17
1&4	670,504	1,606E+09	2506,79
1&5	372,458	701645000	3630,32
2&3	1646,62	1,789E+09	3558,74
2&4	701,948	1,633E+09	3583,46
2&5	424,372	857982000	13984,1
3&4	719,845	1,687E+09	5065,25
3&5	475,939	1,055E+09	21230,1
4&5	471,919	1,082E+09	20846,9
1&2&3	1529,28	1,792E+09	3192,7
1&2&4	665,476	1,619E+09	3650,61
1&2&5	382,728	759212000	11705,7
1&3&4	668,378	1,671E+09	4555,14
1&3&5	440,767	955823000	18061,4
1&4&5	461,435	1,04E+09	18212,4
2&3&4	692,01	1,672E+09	5342,58
2&4&5	471,237	1,071E+09	20161
3&4&5	500,298	1,165E+09	21241,3
1&2&3&4	697,252	1,672E+09	4924,12
1&2&3&5	456,138	999842000	17739,8
1&3&4&5	502,496	1,166E+09	18920,2
2&3&4&5	509,17	1,187E+09	20172
1&2&3&4&5	508,638	1,187E+09	18293,6

E.7. Participation factors

Table 6.11: The participation factors for mass, per mode, for all samples. The numbers are normalised with respect to the largest value.

	Tip ₁	Tip ₂	Base ₁	Base ₂
Mode 1	1	1	0,000838	4,50E-04
Mode 2	0,53916687	0,131975	0,026234	1,44E-02
Mode 3	0,28969517	0,101607	0,16393	9,17E-02
Mode 4	0,17844911	0,393984	0,48654	2,79E-01
Mode 5	0,17339689	0,565632	1	5,92E-01
Mode 6	-	-	-	1

Table 6.12: The participation factors for stiffness, per mode, for all samples. The numbers are normalised with respect to the largest value.

	Tip ₁	Tip ₂	Base ₁	Base ₂
Mode 1	3,3659E-07	1,34E-06	0,001131	0,000524
Mode 2	0,00039346	0,00125	0,029499	0,014147
Mode 3	0,01822561	0,043946	0,158422	0,07812
Mode 4	0,19367958	0,319268	0,437553	0,216802
Mode 5	1	1	1	0,477374
Mode 6	-	-	-	1

F.8. Combining modes with the largest participation factor

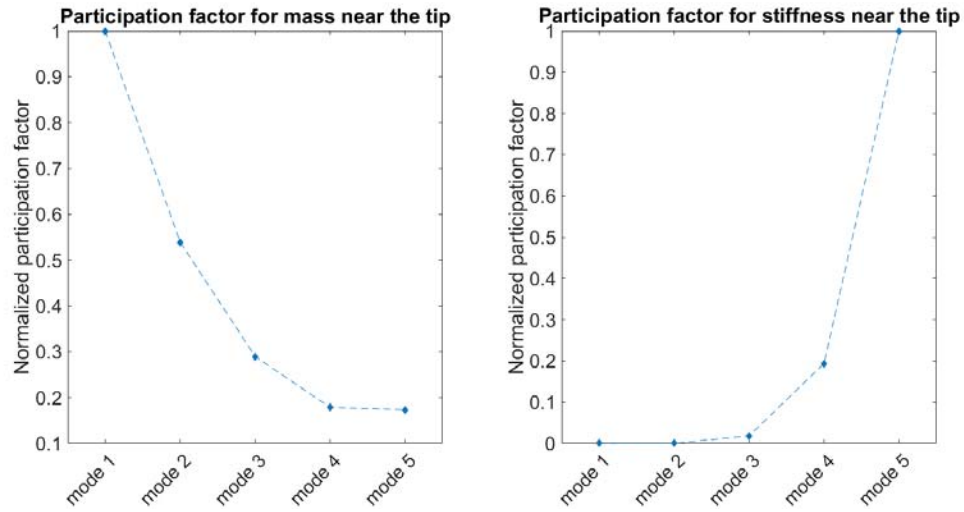


Figure 6.29: The participation factors for sample tip₁, normalised with respect to the largest value, are shown in these graphs. The figure on the left-hand sides shows the weighting factors regarding the mass and the figure on the right shows the participation factors per mode regarding the stiffness. The dashed lines are added to guide the eye.

Table 6.13: A recursive approach between two modes of sample tip₁ is used to derive the values in this table. The RMS error is minimized to find ρ from the lower and E from the higher mode.

		RECURSIVE METHOD - modes tip ₁	
		Minimizing the RMS value to find ρ from lower and E from higher mode	
mode (ρ)	mode (E)	ρ [kgm ⁻³]	E [Pa]
1	5	1939.18	2.85E+09
1	4	1938.57	1.83E+09
1	3	1938.03	9.57E+08
1	2	1943.84	1.15E+10
2	5	1618.41	2.45E+09
2	4	1581.27	1.53E+09
2	3	1535.17	4.08E+08
3	4	3570.89	3.26E+09
3	5	11462.4	1.66E+10
4	5	-247.176	3.76092

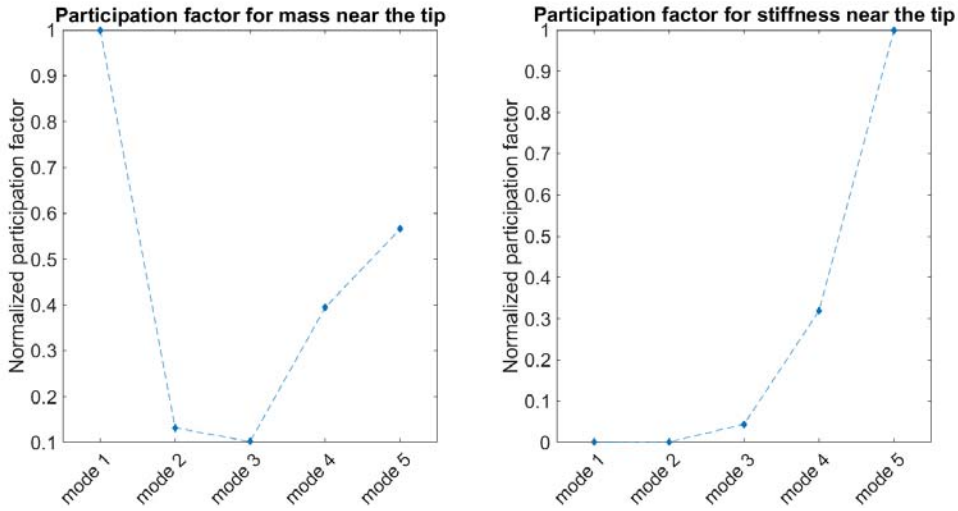


Figure 6.30: The participation factors for sample tip₂, normalised with respect to the largest value, are shown in these graphs. The figure on the left-hand sides shows the weighting factors regarding the mass and the figure on the right shows the participation factors per mode regarding the stiffness. The dashed lines are added to guide the eye.

Table 6.14: A recursive approach between two modes of sample tip₂ is used to derive the values in this table. The RMS error is minimized to find ρ from the lower and E from the higher mode.

		RECURSIVE METHOD - modes tip ₂	
		Minimizing the RMS value to find ρ from lower and E from higher mode	
mode (ρ)	mode (E)	ρ [kgm ⁻³]	E [Pa]
1	5	1389.42	4.23E+09
1	4	1388.97	3.65E+09
1	3	1387.52	1.81E+09
1	2	1386.06	1.00077
2	5	3859.01	1.34E+10
2	4	3401.71	9.5E+09
2	3	2662.86	3.54E+09
3	4	15.6538	1.00007
4	3	56.0951	5.27E+07
3	5	15.6053	1.00085
5	3	242.637	2.97E+09
4	5	56.0925	1.00002
5	4	550.417	1.33E+09

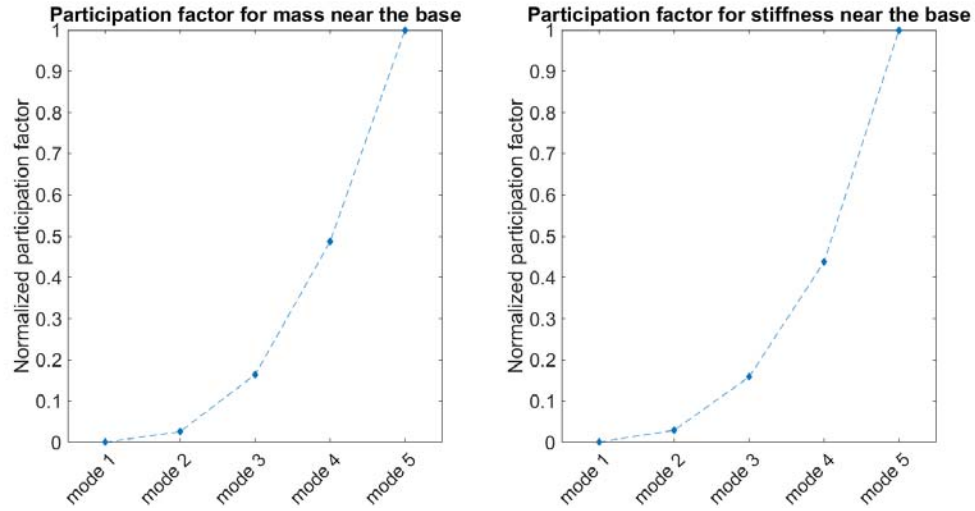


Figure 6.31: The participation factors for sample base₁, normalised with respect to the largest value, are shown in these graphs. The figure on the left-hand sides shows the weighting factors regarding the mass and the figure on the right shows the participation factors per mode regarding the stiffness. The dashed lines are added to guide the eye.

Table 6.15: A recursive approach between two modes of sample base₁ is used to derive the values in this table. The RMS error is minimized to find E from the lower and ρ from the higher mode.

		RECURSIVE METHOD - modes base ₁	
		Minimizing the RMS value to find E from lower and ρ from higher mode	
mode (ρ)	mode (E)	ρ [kgm ⁻³]	E [Pa]
4	5	1101.21	9.31E+08
5	4	1101.19	9.31E+08
3	5	1043.58	8.63E+08
5	3	1043.58	8.63E+08
3	4	935.289	8.5E+08
4	3	935.289	8.50E+08
2	5	903.011	6.99E+08
2	4	614.322	6.95E+08
1	5	630.182	3.82E+08
2	3	2.00648	7.39E+08
1	4	2.00646	4.01E+08
1	3	1.33765	7.39E+08
1	2	5.35025	6.87E+08

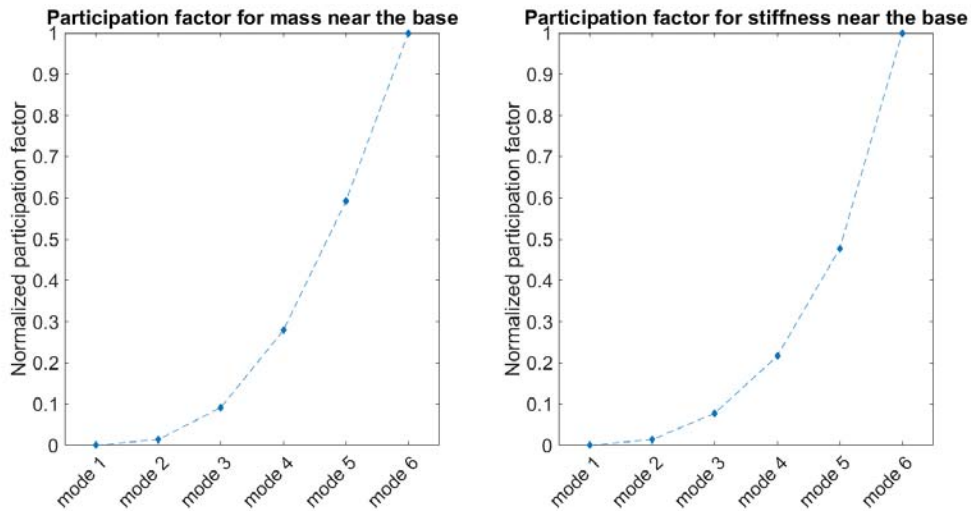


Figure 6.32: The participation factors for sample base₂, normalised with respect to the largest value, are shown in these graphs. The figure on the left-hand sides shows the weighting factors regarding the mass and the figure on the right shows the participation factors per mode regarding the stiffness. The dashed lines are added to guide the eye.

Table 6.16: A recursive approach between two modes of sample base₂ is used to derive the values in this table. The RMS error is minimized to find E from the lower and ρ from the higher mode.

		RECURSIVE METHOD - modes base ₂	
		Minimizing the RMS value to find E from lower and ρ from higher mode	
mode (ρ)	mode (E)	ρ [kgm ⁻³]	E [Pa]
5	6	2445.11	2.21E+09
4	6	2363.77	2.12E+09
4	5	2283.65	2.09E+09
3	6	2163.59	1.88E+09
3	5	1978.12	1.86E+09
3	4	1359.24	1.82E+09
2	6	1981.33	1.66E+09
2	5	1702.61	1.66E+09
2	4	788.983	1.65E+09
2	3	-1189.74	1.64E+09
1	6	1623.91	1.24E+09
1	5	1136.61	1.24E+09
1	4	-617.796	1.24E+09
1	3	-6713.58	1.24E+09
1	2	-50769.9	1.24E+09

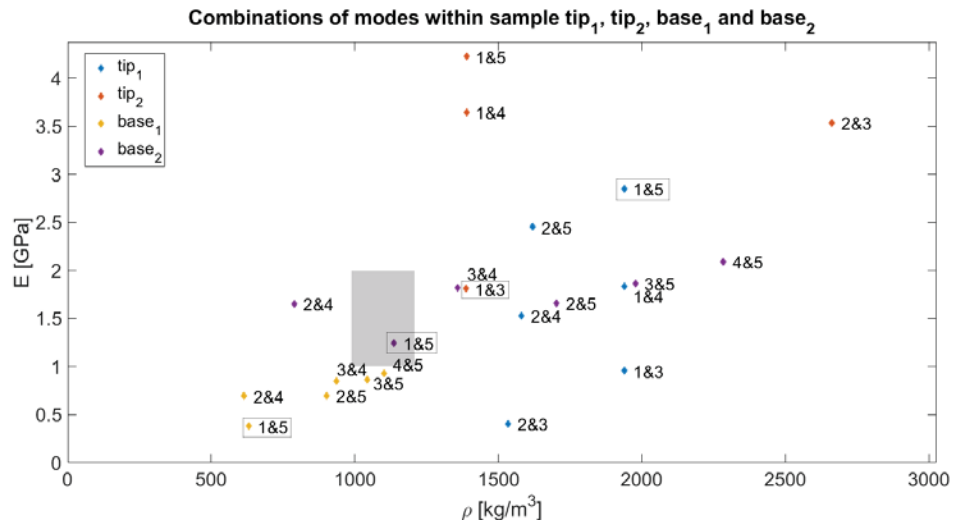


Figure 6.33: The results for the combination of two modes from one sample are shown in this scatter plot. The samples with a polymer near the tip derived ρ from the lower and E from the higher modes. Conversely, the samples with base-located polymers used lower modes to find E and higher modes to find ρ . The grey area represents the literature values. For the mode combinations within a square, the modes with a largest mass and largest stiffness effects are combined.

Table 6.17: This table gives a list of statistic values from combinations of two modes from one sample. The mean value, variance and standard deviation are given for E and ρ per sample.

		tip ₁	tip ₂	base ₁	base ₂
mean	E [GPa]	2.45	3.94	0.77	1.74
	ρ [kg/m ³]	1938.57	2026.14	919.15	1530.925
standard deviation	E [GPa]	5.27	4.07	0.18	0.26
	ρ [kg/m ³]	3027.095	1020.925105	187.8894895	505.11

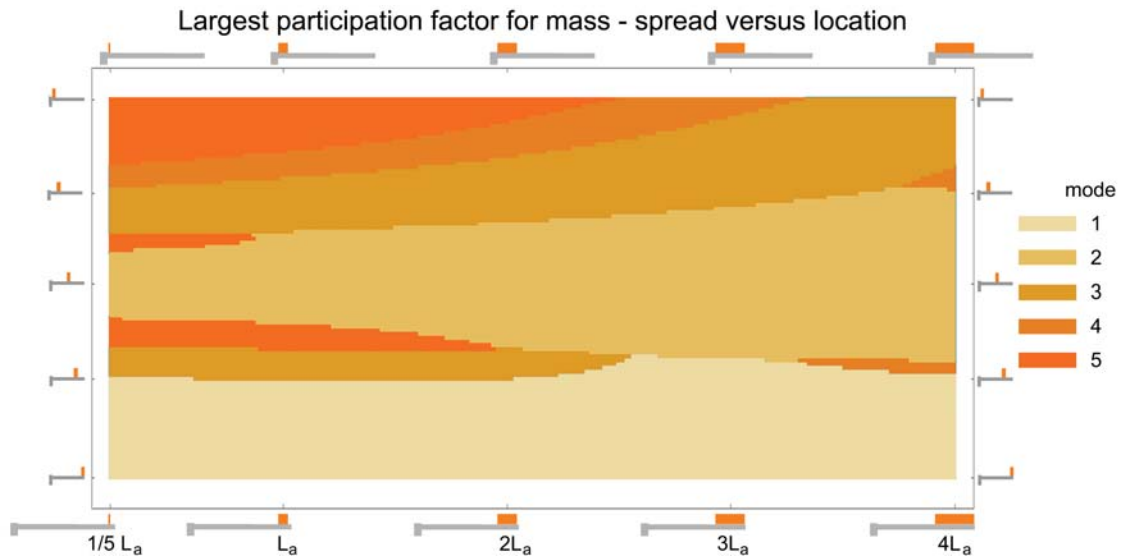


Figure 6.34: The participation factor based on mass depends on the location and spread of the added polymer. This graph shows the modes with the highest participation factors for different locations and lengths. The properties of base₂ are used to freeze the other variables.

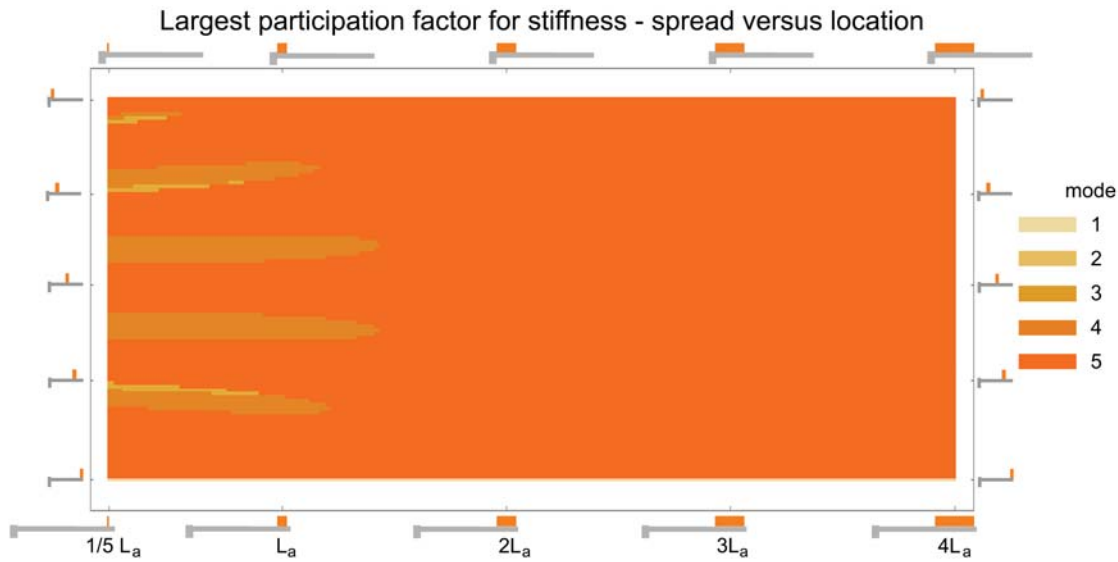


Figure 6.35: The participation factor based on stiffness depends on the location and spread of the added polymer. This graph shows the modes with the highest participation factors for different locations and lengths. The properties of base₂ are used to freeze the other variables.

G. Differences between two approaches

Table 6.18: Sample tip₁ gives the listed results for a density of 1939.18 kgm⁻³ and a Young's modulus of 2.85 GPa.

Mode number	1	2	3	4	5
f before [kHz]	13.13	83.23	233.9	459.1	759.7
f after experimentally [kHz]	11.21	79.34	230.7	458.7	765.3
f after theoretically [kHz]	10.922	74.336	220.30	448.35	755.89
Δf experimentally [%]	-14.62	-3.51	-1.37	-0.09	+0.74
Δf theoretically	-16.82	-10.69	-5.81	-2.34	-0.50

Table 6.19: Sample tip₂ gives the listed results for a density of 1389.42 kgm⁻³ and a Young's modulus of 4.23 GPa.

Mode number	1	2	3	4	5
f before [kHz]	11.52	72.99	205.2	403.3	667.7
f after experimentally [kHz]	11	72.21	204.6	400.7	660.4
f after theoretically [kHz]	11.023	72.745	206.22	402.02	660.52
Δf experimentally [%]	-4.51	-1.07	-0.29	-0.64	-1.09
Δf theoretically [%]	-4.31	-0.34	+0.50	-0.32	-1.08

Table 6.20: Sample base₁ gives the listed results for a density of 1101.21 kgm⁻³ and a Young's modulus of 0.93 GPa.

Mode number	1	2	3	4	5
f before [kHz]	13.31	84.07	236.1	463.7	767.4
f after experimentally [kHz]	13.7	85.62	238.7	464.4	761.1
f after theoretically [kHz]	13.892	86.093	238.98	464.40	761.33
Δf experimentally [%]	+2.93	+1.84	+1.10	+0.15	-0.82
Δf theoretically [%]	+4.37	+2.41	+1.22	+0.15	-0.79

Table 6.21: Sample base₂ gives the listed results for a density of 2445.11 kgm⁻³ and a Young's modulus of 0.21 GPa.

Mode number	1	2	3	4	5	6
f before [kHz]	11.19	70.92	199.5	391.7	649.4	970.98
f after experimentally [kHz]	12.11	75.06	207.2	399.3	647.1	951.55
f after theoretically [kHz]	12.58	76.39	208.69	399.73	647.03	948.32
Δ f experimentally [%]	+8.22	+5.84	+3.86	+1.94	-0.35	-2.00
Δ f theoretically [%]	+12.42	+7.71	+4.61	+2.05	-0.36	-2.33

Table 6.22: Sample base₁ gives the listed results for a density of 630.18 kgm⁻³ and a Young's modulus of 0.38 GPa.

Mode number	1	2	3	4	5
f before [kHz]	13.31	84.07	236.1	463.7	767.4
f after experimentally [kHz]	13.7	85.62	238.7	464.4	761.1
f after theoretically [kHz]	13.628	84.997	237.06	462.63	761.32
Δ f experimentally [%]	+2.93	+1.84	+1.10	+0.15	-0.82
Δ f theoretically [%]	+2.39	+1.10	+0.41	-0.23	-0.79

Table 6.23: Sample base₂ gives the listed results for a density of 1623.91 kgm⁻³ and a Young's modulus of 1.24 GPa.

Mode number	1	2	3	4	5	6
f before [kHz]	11.19	70.92	199.5	391.7	649.4	970.98
f after experimentally [kHz]	12.11	75.06	207.2	399.3	647.1	951.55
f after theoretically [kHz]	12.047	74.053	204.27	394.68	643.68	949.37
Δ f experimentally [%]	+8.22	+5.84	+3.86	+1.94	-0.35	-2.00
Δ f theoretically [%]	+7.66	+4.42	+2.39	+0.76	-0.88	-2.23

H. Combining multiple modes

Table 6.24: This table lists the resulting material properties when combining multiple modes and minimising the RMS error.

mode	tip ₁		tip ₂		base ₁		base ₂	
	ρ [kgm ⁻³]	E [GPa]	ρ [kgm ⁻³]	E [GPa]	ρ [kgm ⁻³]	E [GPa]	ρ [kgm ⁻³]	E [GPa]
1	1937,43	0,001003	1386,06	0,00100191	407726	0,494343	1533470	1,51456
1-2	1943,84	11,5426	1784,06	1,00002E-09	-23860,5	0,375545	-50769,9	1,23531
1-2-3	1588,77	0,486107	1896,37	2,46582	-666,833	0,660618	1	1,66263
1-2-3-4	1810,09	1,68249	558,705	1,30417	807,705	0,793386	1143,6	1,76166
1-2-3-4-5	711,407	1,26211	505,435	1,17651	1031,62	0,857667	2024,6	1,91912
1-2-3-4-5-6							2250,61	2,00314

I. Clamping effect

Table 6.25: This table lists the measured Q-factors for the first five modes of ten different tests. For each test a cantilever is clamped in the setup.

Q-factor	Mode 1	Mode 2	Mode 3	Mode 4	Mode 5
Test 1	57,06715	149,6125	252,2812	362,574	420,6389
Test 2	56,70226	157,256	254,1931	355,5145	425,6562
Test 3	56,83816	155,216	259,9775	358,6656	414,1227
Test 4	54,77715	154,5822	248,5249	354,9169	426,3193
Test 5	56,23142	155,0537	255,0452	350,8531	422,8005
Test 6	54,42461	154,4033	254,1803	350,5205	396,9588
Test 7	55,09614	155,4265	256,5395	353,4208	423,7558
Test 8	56,02891	154,8685	254,0294	355,4258	427,7197
Test 9	60,10372	148,72957	257,3773	355,8983	434,5111
Test 10	54,81182	156,2643	257,2454	349,064	412,5177

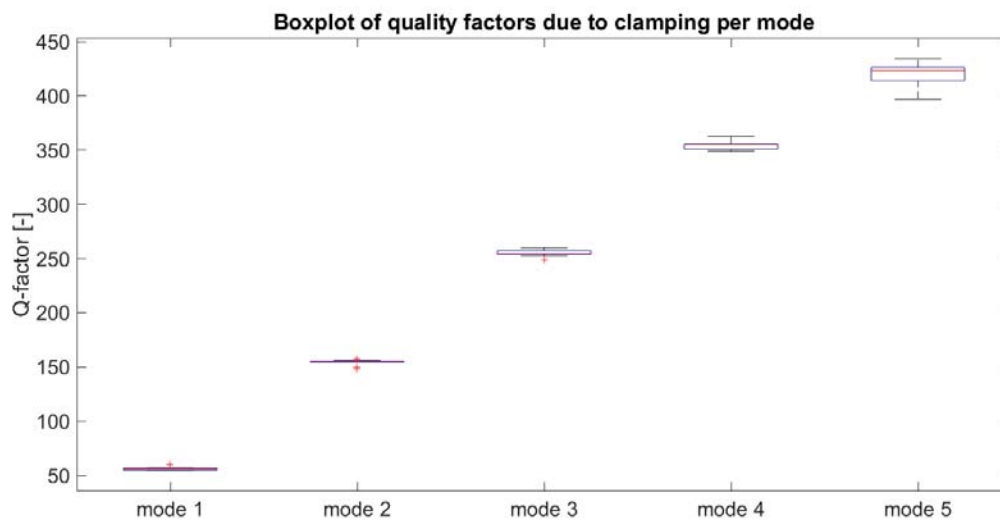


Figure 6.36: This box plot shows the influence of the clamping on the Q-factor for the first five flexural modes. One beam was clamped, measured and taken out of the set-up for ten times. The Q-factor was determined by Polytech software which is based on a curve fit of one peak and subsequently using the -3 dB method.

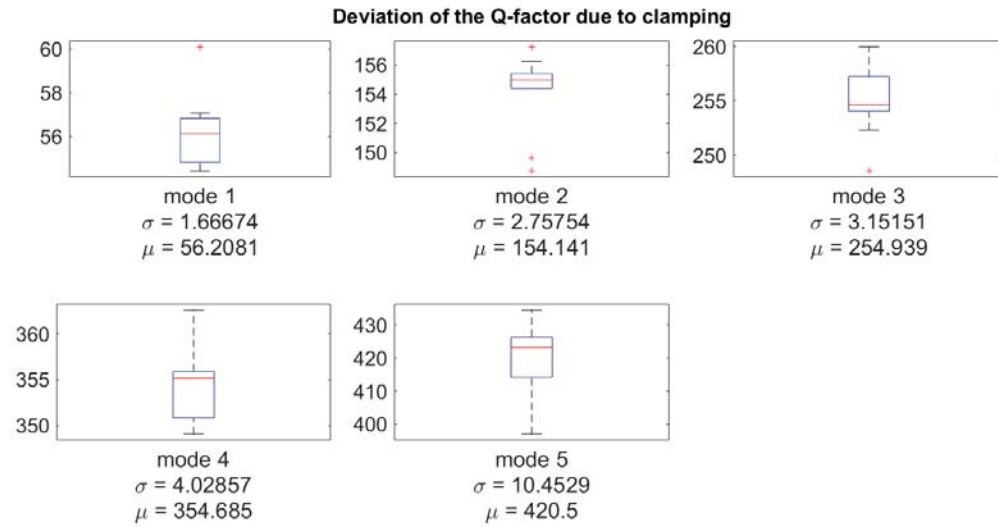


Figure 6.37: The box plots in this figure clarify the deviations in the Q-factor, due to the clamping. One beam was clamped, measured and taken out of the set-up for ten times. The Q-factor was determined by Polytech software which is based on a curve fit of one peak and subsequently using the -3 dB method.

Table 6.26: The resonance frequencies of the first five modes are measured for a cantilever in ten different tests. For each test, the cantilever was clamped in the setup. The results are listed below.

Resonance frequency	Mode 1	Mode 2	Mode 3	Mode 4	Mode 5
Test 1	13225,8	83538,8	234774,6	461178,6	762800,8
Test 2	13226,9	83546,2	234733,8	461234,4	762873,2
Test 3	13227,9	83534,1	234660,4	461198,5	762122,7
Test 4	13224,7	83537,3	234703,6	461229,4	762797,7
Test 5	13225,8	83538,5	234734,1	461180,6	762751,9
Test 6	13227,4	83533,8	234732	461268,2	763001,4
Test 7	13227,5	83544,1	234834,1	461226,5	762829,4
Test 8	13228,9	83535,2	234782,8	461190,4	762845,6
Test 9	13224,3	83524,1	234771,7	461206,5	762822,8
Test 10	13227,6	83548,9	234753,8	461222,8	762927,5

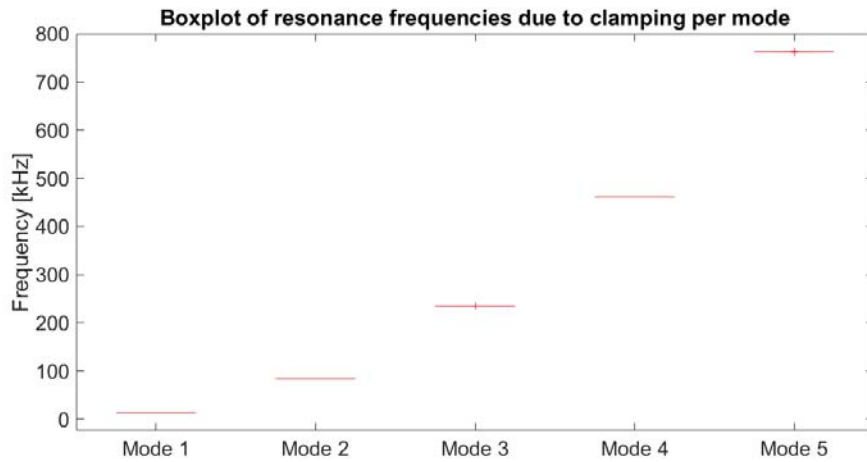


Figure 6.38: From this figure it can be seen that the deviation in resonance frequencies due to clamping is low. The spread of the whisker plots are small. One beam was clamped, the resonance frequency for each mode was measured and afterwards the cantilever chip was taken out of the set-up for ten times in a row.

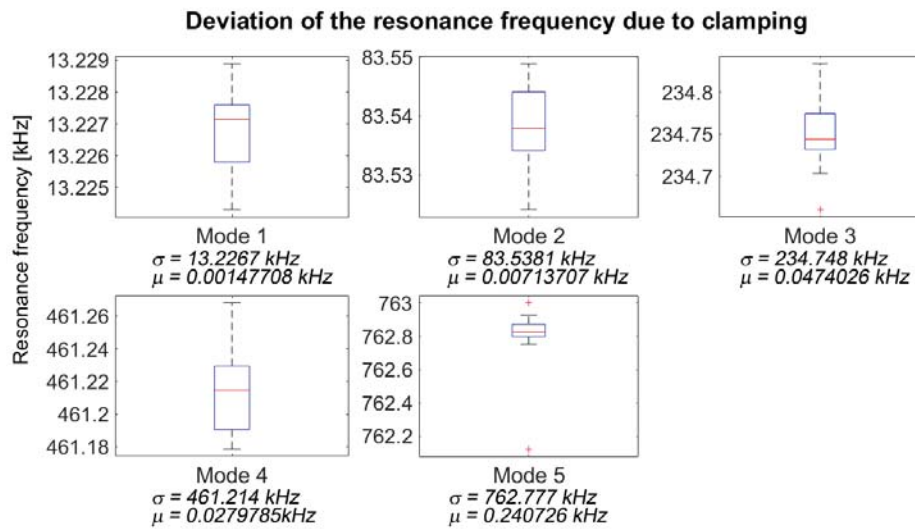


Figure 6.39: This whisker plots show the effect of the clamping on the resonance frequency of the cantilever. One beam was clamped, measured and taken out of the set-up for ten times in a row.

J. Validation for the Young's modulus via an indentation method

Within this research, theory en experiments are linked with the intention to decouple mass and stiffness effects of an adhesive. In the end, the results need to be validate. A research by Cross *et al.* was presented in the Introduction (??) of this report. Within this research, the Young's modulus of multiple cells was determined via indentation: By indenting the samples a force,distance-curve is obtained, from which the Young's modulus can be obtained. Layers of approximately $3 \mu\text{m}$ thick were fabricated on the cantilever substrate, in the same way as the samples were produced. These layers were indented using an AFM system (Nanosurf FlexAFM) with a contact mode cantilever with integrated tip (NanoWorld, CONTR, $\sim 13 \text{ kHz}$). The stiffness of the cantilever was calibrated using the inbuilt thermal tune method which is based on brownian motion. The obtained force,distance-curve during the retraction of the cantilever is shown in Figure 6.40. The Young's modulus of the sample can be obtained by fitting the orange part of the curve to a theoretical model described by Equation 6.10.

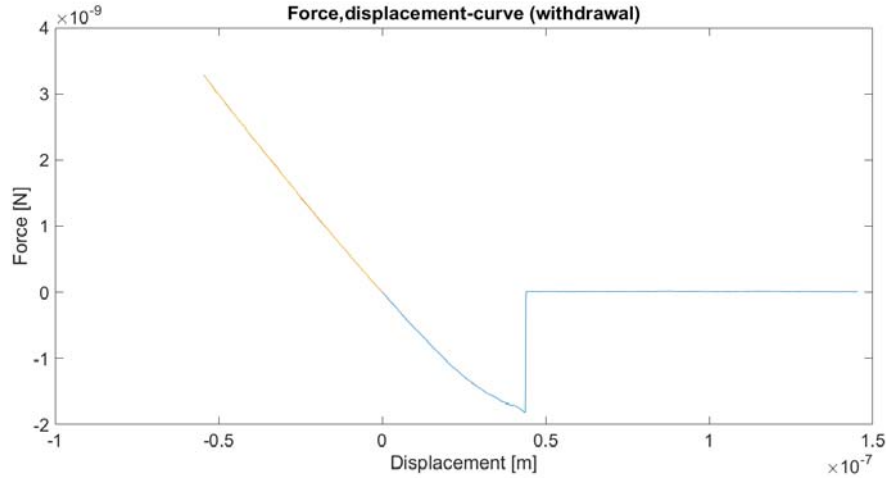


Figure 6.40: This graph represents the experimental results of an AFM indentation experiment. The orange part of the curve can be evaluated using the Hertz model. In this way, the Young's modulus of the sample can e determined.

$$F_{\text{Hertz}}(\delta) = \frac{4}{3} E^* \sqrt{R}(\delta)^{3/2} \quad (6.10)$$

R is the radius of the indenter, δ represents the indentation depth. The distributor of the cantilevers promises a tip radius of 12 nm as a maximum. Such dimensions are too small to measure with an SEM. Therefore, this value is taken as an approximation for R .

$$\frac{1}{E^*} = \frac{1 - \nu_{\text{tip}}^2}{E_{\text{tip}}} + \frac{1 - \nu_{\text{sample}}^2}{E_{\text{sample}}} \quad (6.11)$$

E_{tip} represents the Young's modulus of the indenter. The cantilevers point in the $\langle 110 \rangle$ direction, corresponding to a Young's modulus of 169 GPa . The Poisson ratio ν_{tip} for silicon is 0.22 and from literature ν_{sample} for IP-L 780 is 0.49 [76].

Figure 6.41 shows the experimentally derived force,distance-curves and the curves in which the theoretical stiffness values are substituted for experiments with IP-L 780 and MICA. It can be seen that the mica is much stiffer than the IP-L 780, but they are both a factor 100 off from the theoretical values. For soft materials a parabolic relation (or at least non-linear at the start) between F and d is expected. however, this curve is straight, indicating that the measurements are not correct.

The experiment on MICA was obtained with a non-contact mode AFM cantilever, which is stiffer than a contact mode AFM cantilever, entailing uncertainties and a lower sensitivity. Furthermore, it was experienced that MICA sticks to the probe resulting in a less accurate measurement (the silicon properties of the tip become incorrect).

When indenting the IP-L with the probe, a lower stiffness was detected as well. This could be explained since the probe of the AFM cantilever is hard and sharp. The probe will pierce through the material. Besides

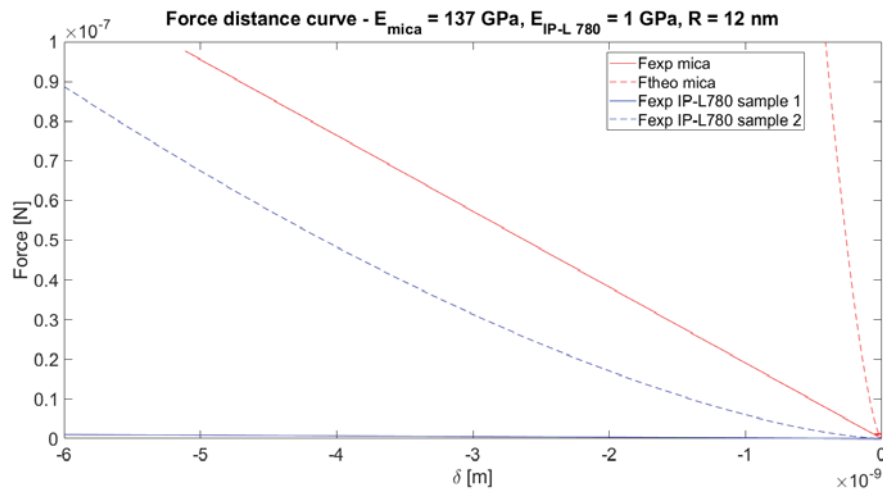


Figure 6.41: Theoretically and experimentally derived force, distance-curves are plotted in this figure. The red coloured lines represent the results for a MICA sample, the blue lines show the results for the IP-L 780 sample. Dashed lines give information on theoretical values.

that, the material was build up of voxel lines. There is a chance as well that a pushed in between these, instead of exactly on it. The use of a blunt tip would have been more useful.

Both samples have a lot of uncertainties and can not be used for the validation of the material properties of IP-L.

K. Cantilever profile

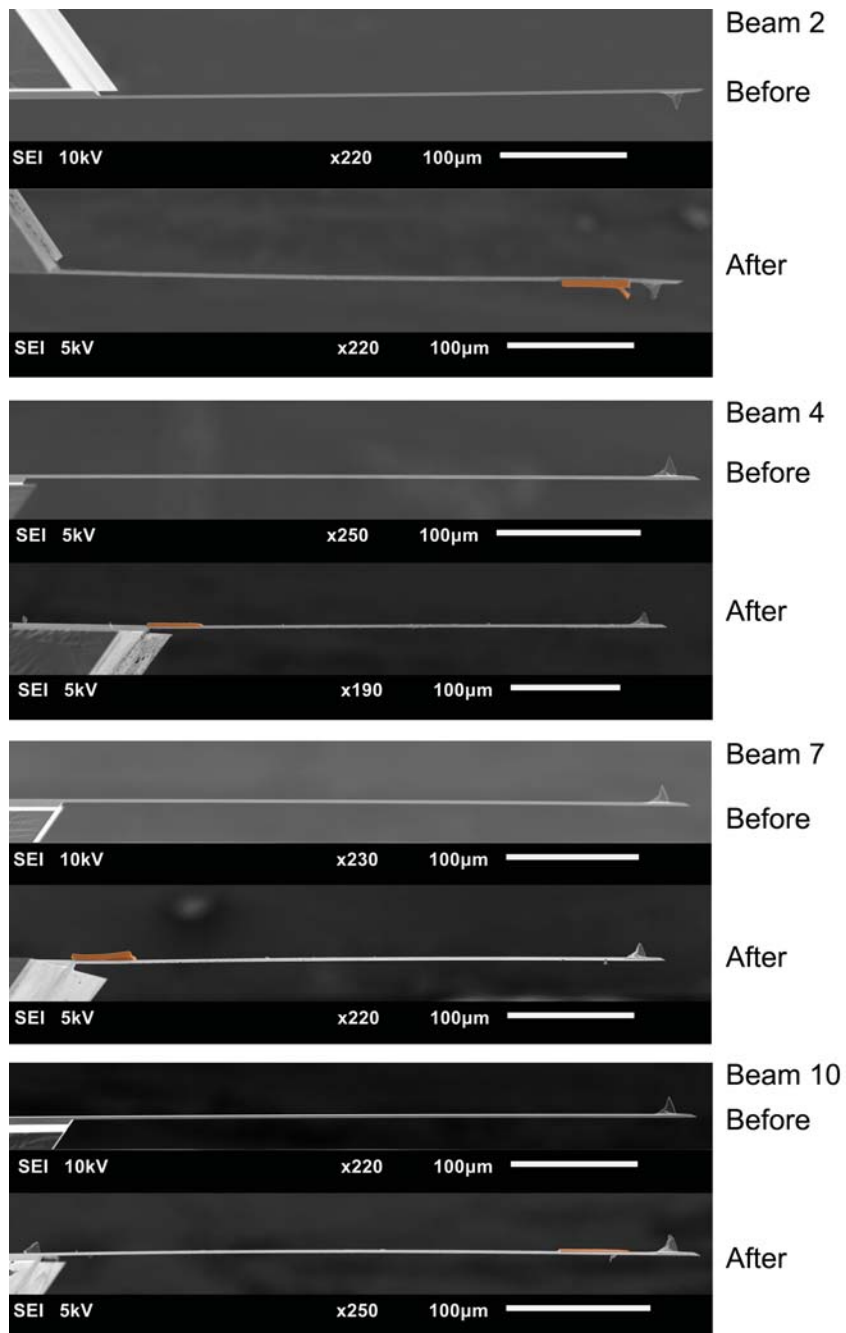


Figure 6.42: The profiles of the cantilevers before and after the deposition of a polymeric layer are shown in this figure. They are derived with an SEM. Beam 2 is sample tip₁, beam 4 sample base₁, beam 7 sample base₂ and beam 10 sample tip₂. Only beam 2 shows a small distortion due to the polymer.

L. Experimentally derived mode shapes

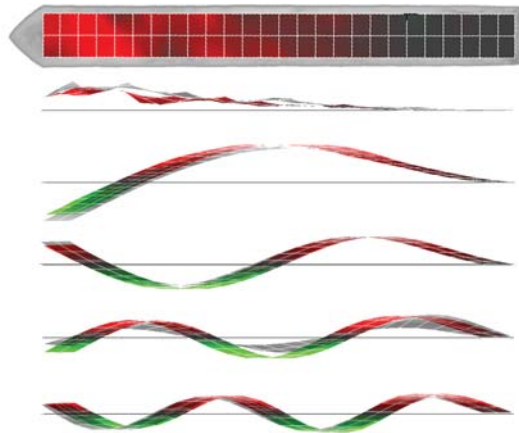


Figure 6.43: The experimentally derived mode shapes for sample tip₁ are shown in this figure. The coloured shapes on the foreground are after the deposition of a polymeric layer. A red colour relates to a positive displacement of the measured point and the green colour represents a negative displacement. The grey shapes on the background are obtained from the bare cantilever.

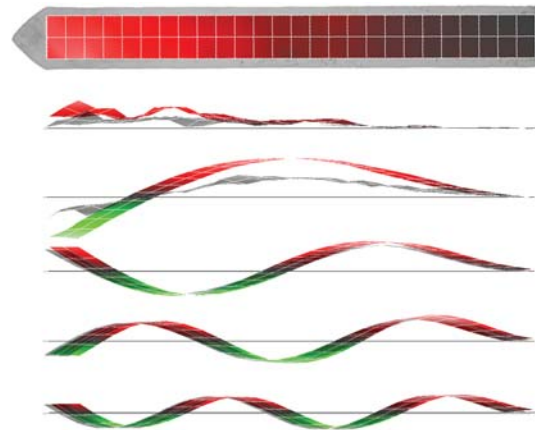


Figure 6.44: The experimentally derived mode shapes for sample base₁ are shown in this figure. The coloured shapes on the foreground are after the deposition of a polymeric layer. A red colour relates to a positive displacement of the measured point and the green colour represents a negative displacement. The grey shapes on the background are obtained from the bare cantilever.

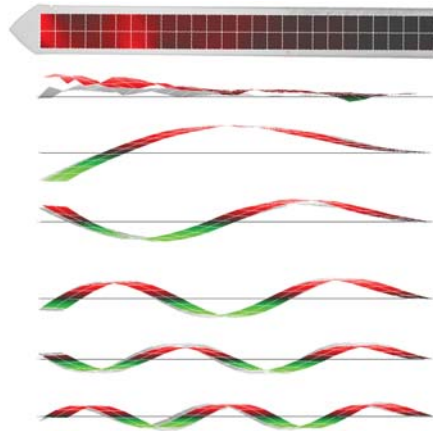


Figure 6.45: The experimentally derived mode shapes for sample base₂ are shown in this figure. The coloured shapes on the foreground are after the deposition of a polymeric layer. A red colour relates to a positive displacement of the measured point and the green colour represents a negative displacement. The grey shapes on the background are obtained from the bare cantilever.

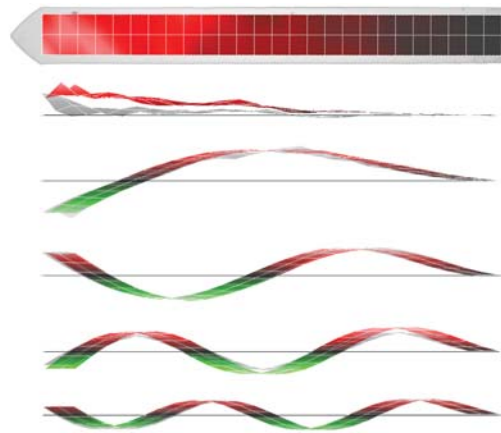


Figure 6.46: The experimentally derived mode shapes for sample tip₂ are shown in this figure. The coloured shapes on the foreground are after the deposition of a polymeric layer. A red colour relates to a positive displacement of the measured point and the green colour represents a negative displacement. The grey shapes on the background are obtained from the bare cantilever.

M. Improve adhesion

Adhesion to the substrate



In case you have difficulties with adhesion of your structures please carefully read and follow this short guide.

Making your structures stick

In general you should first make sure, that your structures are programmed such that they have sufficient contact to the substrate surface due to the writing process. Typically you can do that by increasing the FindInterfaceAt value. If your structure starts at $z=0$, values between 0.2 and 1.0 are recommended, depending on the size of your structure and the tilt of your substrate.

Additionally make sure you are using the correct approach. If you write through a glass substrate, then InvertZaxis needs to be off and in most cases your structures should start at $z=0$ (for rigid resists like IP-G this may differ).

However, if you write on the lower side of the substrate, that is in DiLL mode, then InvertZaxis needs to be on and again your structures should be written bottom-up (starting at $z=0$).

In many cases one of the above corrections is necessary if you see that lines move during the writing process (if the reason is not the layer distance).

Furthermore it is important that your structures have enough mechanical stability. Especially for very open structures with thin connections it is often necessary to use a higher dose to ensure stability, i.e., increase LaserPower value, writing several lines instead of just one or decrease writing speed. For a non-GT system try to use PerfectShapeQuality instead of intermediate or fast. Additionally please make sure that your layer (or slicing) distance is not too big.

Steps to improve adhesion

If software parameters did not help, you can try 3 different process steps. Start with the first and add them up if necessary.

Step 1: Clean your substrates using plasma or chemicals

On some substrates like silicon it may be beneficial to add plasma etching to the process of substrate cleaning. On substrates like glass it may help to clean very thoroughly using Piranha solution. Please take good care when using aggressive cleaning solutions and ask your safety officer for proper handling of chemicals.

CONTACT

Nanoscribe GmbH
Hermann-von-Helmholtz-Platz 1
76344 Eggenstein-Leopoldshafen
Germany

Tel +49 721 60 82 88 14
Fax +49 721 60 82 88 48
E-Mail service@nanoscribe.de

www.nanoscribe.de
www.facebook.com/nanoscribe
www.youtube.com/nanoscribe

Adhesion to the substrate



Step 2: Silanization of substrate surface

A very successful way in case of IP resists and with respect to glass and silicon substrates in our experience has been Silanization. It is supposed to help for metal-oxide substrates as well. It renders the surface hydrophobic and leads to a chemical bond between resist and substrate.

Process solution for IP-Resists: Silanization

1. Clean the substrates with a wiper and IPA (you can use acetone before as well)
2. (optional) Subsequently clean them with a plasma etcher (O₂ or air)
3. Then the substrates need to be submerged in an ethanol (can also be acetone) solution. About 25ml ethanol mixed with 4 drops of 3-(Trimethoxysilyl)propyl methacrylate. To avoid evaporation, please remember cover the beaker/petri-dish, e.g., with Parafilm.
4. Leave them submerged for at least 5 minutes, but more times usually yields better adhesion results. We recommend to leave the substrates submerged for several hours, but overnight is fine, too.
5. After that the substrates should be rinsed under tap water (or distilled / deionized water). You should observe, that the surface is hydrophobic and therefore the water will not stick to it.
6. Immediately afterwards blow dry them with nitrogen or air.

Continue with your normal process: glue them onto the sample holder and add a drop of oil / resist, etc.

A silanized substrate can be used even after a couple of days storage. Just make sure that it will not be contaminated with dust or moisture.

3-(Trimethoxysilyl)propyl methacrylate (CAS: 2530-85-0) can be purchased from Sigma Aldrich with the order number M6514 or Polysciences Inc catalog number 02476-250. The 25ml bottle is about 50€. It should be stored in a fridge.

Please read the material safety data sheet of 3-(Trimethoxysilyl)propyl methacrylate before using it!

Step 3: Adhesion layer of substrate surface

For very problematic large-area cases, we recommend spin-coated adhesion layers, e.g., TI-prime that is the commonly used as adhesion layer for positive-tone AZ resists. Please refer to readily available documentation on process details.

http://www.microchemicals.com/products/adhesion_promotion/ti_prime.html

As another option for such cases we recommend to spin a very thin layer of SU-8, process it, and flood expose it. Don't forget the post exposure bake, development is not needed though. Make sure to correct for the layer thickness when finding the interface. SU-8 was found to be very sticky to all IP-resist.

Bibliography

- [1] Thomas P Burg, Michel Godin, Scott M Knudsen, Wenjiang Shen, Greg Carlson, John S Foster, Ken Babcock, and Scott R Manalis. Weighing of biomolecules, single cells and single nanoparticles in fluid. *nature*, 446(7139):1066–1069, 2007.
- [2] Sarah E Cross, Yu-Sheng Jin, Julianne Tondre, Roger Wong, JianYu Rao, and James K Gimzewski. Afm-based analysis of human metastatic cancer cells. *Nanotechnology*, 19(38):384003, 2008.
- [3] Chin Wee Shong, Chorng Haur Sow, and Andrew TS Wee. *Science at the nanoscale: an introductory textbook*. Pan Stanford Publishing, 2010.
- [4] Marina Puig-de Morales-Marinkovic, Kevin T Turner, James P Butler, Jeffrey J Fredberg, and Subra Suresh. Viscoelasticity of the human red blood cell. *American Journal of Physiology-Cell Physiology*, 293(2):C597–C605, 2007.
- [5] Ming Dao, Chwee Teck Lim, and Subra Suresh. Mechanics of the human red blood cell deformed by optical tweezers. *Journal of the Mechanics and Physics of Solids*, 51(11):2259–2280, 2003.
- [6] Jochen Guck, Stefan Schinkinger, Bryan Lincoln, Falk Wottawah, Susanne Ebert, Maren Romeyke, Dominik Lenz, Harold M Erickson, Revathi Ananthakrishnan, Daniel Mitchell, et al. Optical deformability as an inherent cell marker for testing malignant transformation and metastatic competence. *Biophysical journal*, 88(5):3689–3698, 2005.
- [7] OpenStax. *Chemistry*. OpenStax, 30 March 2015. <<http://cnx.org/content/col11760/latest/>>.
- [8] Murali Krishna Ghatkesar, Hans-Peter Lang, Christoph Gerber, Martin Hegner, and Thomas Braun. Comprehensive characterization of molecular interactions based on nanomechanics. *PloS one*, 3(11): 1–6, 11 2008. doi: 10.1371/journal.pone.0003610. URL <https://doi.org/10.1371/journal.pone.0003610>.
- [9] O Malvar, JJ Ruz, PM Kosaka, CM Domínguez, E Gil-Santos, M Calleja, and J Tamayo. Mass and stiffness spectrometry of nanoparticles and whole intact bacteria by multimode nanomechanical resonators. *Nature communications*, 7:13452, 2016.
- [10] H Sadeghian, JFL Goosen, A Bossche, and F Van Keulen. A mechanistic model for adsorption-induced change in resonance response of submicron cantilevers. In *MOEMS-MEMS 2008 Micro and Nanofabrication*, pages 68850E–68850E. International Society for Optics and Photonics, 2008.
- [11] Javier Tamayo, Priscila M Kosaka, José J Ruz, Álvaro San Paulo, and Montserrat Calleja. Biosensors based on nanomechanical systems. *Chemical Society Reviews*, 42(3):1287–1311, 2013.
- [12] Søren Dohn, W Svendsen, Anja Boisen, and Ole Hansen. Mass and position determination of attached particles on cantilever based mass sensors. *Review of Scientific Instruments*, 78(10):103303, 2007.
- [13] Ramazan Erdem, Mustafa İlhan, and Erhan Sancak. Analysis of emse and mechanical properties of sputter coated electrospun nanofibers. *Applied Surface Science*, 380:326–330, 2016.
- [14] Fabian Kohler. 3d micro-printing by direct laser writing, January 2017. Photonic Professional GT, Technology introduction and workflow.
- [15] M.L.C. De Laat. In situ stiffness adjustment for afm probes. Master’s thesis, Delft University of Technology, Mechanical, Maritime and Materials Engineering, Precision and Microsystems Engineering, Micro and Nano Engineering, February 2016.
- [16] Anton A Bauhofer, Sebastian Krödel, Jan Rys, Osama R Bilal, Andrei Constantinescu, and Chiara Daraio. Harnessing photochemical shrinkage in direct laser writing for shape morphing of polymer sheets. *Advanced Materials*, 2017.

- [17] Phil Russell. *AFM Probe Manufacturing*. NanoWorld Services GmbH, November 2008.
- [18] Nanoscribe GmbH. Ip photoresists overview. <https://www.nanoscribe.de/en/products/ip-photoresists>, retrieved June 2017.
- [19] AG NanoWorld. Contact mode - reflex coating, retrieved May 2017. <http://www.nanoworld.com/contact-mode-reflex-coated-pointprobe-afm-tip-contr>.
- [20] M Selim Hanay, Scott I Kelber, Cathal D O'Connell, Paul Mulvaney, John E Sader, and Michael L Roukes. Inertial imaging with nanomechanical systems. *Nature nanotechnology*, 10(4):339–344, 2015.
- [21] Murali Krishna Ghatkesar, Viola Barwich, Thomas Braun, Jean-Pierre Ramseyer, Christoph Gerber, Martin Hegner, Hans Peter Lang, Ute Drechsler, and Michel Despont. Higher modes of vibration increase mass sensitivity in nanomechanical microcantilevers. *Nanotechnology*, 18(44):445502, 2007.
- [22] Søren Dohn, Silvan Schmid, Fabien Amiot, and Anja Boisen. Position and mass determination of multiple particles using cantilever based mass sensors. *Applied Physics Letters*, 97(4):044103, 2010.
- [23] D Ramos, J Tamayo, J Mertens, M Calleja, LG Villanueva, and A Zaballos. Detection of bacteria based on the thermomechanical noise of a nanomechanical resonator: origin of the response and detection limits. *Nanotechnology*, 19(3):035503, 2007.
- [24] M Amabili, S Carra, L Collini, R Garziera, and A Panno. Estimation of tensile force in tie-rods using a frequency-based identification method. *Journal of Sound and Vibration*, 329(11):2057–2067, 2010.
- [25] Warren Carl Oliver and George Mathews Pharr. An improved technique for determining hardness and elastic modulus using load and displacement sensing indentation experiments. *Journal of materials research*, 7(06):1564–1583, 1992.
- [26] Jinju Chen. Nanobiomechanics of living cells: a review. *Interface focus*, 4(2):20130055, 2014.
- [27] Manfred Radmacher, Monika Fritz, Claudia M Kacher, Jason P Cleveland, and Paul K Hansma. Measuring the viscoelastic properties of human platelets with the atomic force microscope. *Biophysical journal*, 70(1):556, 1996.
- [28] JA Hildebrand and D Rugar. Measurement of cellular elastic properties by acoustic microscopy. *Journal of microscopy*, 134(3):245–260, 1984.
- [29] Robert M Hochmuth. Micropipette aspiration of living cells. *Journal of biomechanics*, 33(1):15–22, 2000.
- [30] Wilbur A Lam, Michael J Rosenbluth, and Daniel A Fletcher. Chemotherapy exposure increases leukemia cell stiffness. *Blood*, 109(8):3505–3508, 2007.
- [31] Satoshi Igawa, Izumi Hayashi, Naohiko Tanaka, Hiromi Hiruma, Masataka Majima, Tadashi Kawakami, Minoru Hirose, Noriyuki Masuda, and Hirosuke Kobayashi. Nitric oxide generated by inos reduces deformability of lewis lung carcinoma cells. *Cancer science*, 95(4):342–347, 2004.
- [32] Barbara Spagnolo, Leonardo Sileo, Enrico Domenico Lemma, Virgilio Brunetti, Elisa De Luca, Teresa Pellegrino, Godefroy Lemenager, Pier Paolo Pompa, Massimo De Vittorio, and Ferruccio Pisanello. Nanofabricated 3d cage-like structures for cancer cell discrimination. In *Nanotechnology (IEEE-NANO), 2015 IEEE 15th International Conference on*, pages 1414–1417. IEEE, 2015.
- [33] H Sadeghian, CK Yang, JFL Goosen, E Van Der Drift, A Bossche, PJ French, and F Van Keulen. Characterizing size-dependent effective elastic modulus of silicon nanocantilevers using electrostatic pull-in instability. *Applied Physics Letters*, 94(22):221903, 2009.
- [34] Hans-Dieter Beckey. *Principles of Field Ionization and Field Desorption Mass Spectrometry: International Series in Analytical Chemistry*. Elsevier, 2016.
- [35] Takahito Ono, Xinxin Li, Hidetoshi Miyashita, and Masayoshi Esashi. Mass sensing of adsorbed molecules in sub-picogram sample with ultrathin silicon resonator. *Review of scientific instruments*, 74(3):1240–1243, 2003.

- [36] Julien Chaste, A Eichler, J Moser, G Ceballos, R Rurali, and A Bachtold. A nanomechanical mass sensor with yoctogram resolution. *Nature nanotechnology*, 7(5):301–304, 2012.
- [37] Javier Tamayo, Daniel Ramos, Johan Mertens, and Montserrat Calleja. Effect of the adsorbate stiffness on the resonance response of microcantilever sensors. *Applied physics letters*, 89(22):224104, 2006.
- [38] Daniel Ramos, Montserrat Calleja, Johann Mertens, Ángel Zaballos, and Javier Tamayo. Measurement of the mass and rigidity of adsorbates on a microcantilever sensor. *Sensors*, 7(9):1834–1845, 2007.
- [39] GY Chen, T Thundat, EA Wachter, and RJ Warmack. Adsorption-induced surface stress and its effects on resonance frequency of microcantilevers. *Journal of Applied Physics*, 77(8):3618–3622, 1995.
- [40] Michel Godin, Vincent Tabard-Cossa, Yoichi Miyahara, Tanya Monga, PJ Williams, LY Beaulieu, R Bruce Lennox, and Peter Grutter. Cantilever-based sensing: the origin of surface stress and optimization strategies. *Nanotechnology*, 21(7):075501, 2010.
- [41] Johann Mertens, Mar Álvarez, and J Tamayo. Real-time profile of microcantilevers for sensing applications. *Applied Physics Letters*, 87(23):234102, 2005.
- [42] Pin Lu, HP Lee, C Lu, and SJ O’shea. Surface stress effects on the resonance properties of cantilever sensors. *Physical Review B*, 72(8):085405, 2005.
- [43] Yin Zhang. Detecting the stiffness and mass of biochemical adsorbates by a resonator sensor. *Sensors and Actuators B: Chemical*, 202:286–293, 2014.
- [44] Søren Dohn, Rasmus Sandberg, Winnie Svendsen, and Anja Boisen. Enhanced functionality of cantilever based mass sensors using higher modes. *Applied Physics Letters*, 86(23):233501, 2005.
- [45] LB Sharos, A Raman, S Crittenden, and R Reifenberger. Enhanced mass sensing using torsional and lateral resonances in microcantilevers. *Applied Physics Letters*, 84(23):4638–4640, 2004.
- [46] NC Perkins and CD Mote. Comments on curve veering in eigenvalue problems. *Journal of Sound and Vibration*, 106(3):451–463, 1986.
- [47] Daniel Ramos, Javier Tamayo, Johann Mertens, Montserrat Calleja, and A Zaballos. Origin of the response of nanomechanical resonators to bacteria adsorption. *Journal of Applied Physics*, 100:106105, 2006.
- [48] Eduardo Gil-Santos, Daniel Ramos, Javier Martínez, Marta Fernández-Regúlez, Ricardo García, Álvaro San Paulo, Montserrat Calleja, and Javier Tamayo. Nanomechanical mass sensing and stiffness spectrometry based on two-dimensional vibrations of resonant nanowires. *Nature nanotechnology*, 5(9):641–645, 2010.
- [49] Yi Cui, Lincoln J Lauhon, Mark S Gudixsen, Jianfang Wang, and Charles M Lieber. Diameter-controlled synthesis of single-crystal silicon nanowires. *Applied Physics Letters*, 78(15):2214–2216, 2001.
- [50] RR Grüter, Z Khan, R Paxman, JW Ndieyira, B Dueck, BA Bircher, JL Yang, U Drechsler, M Despont, RA McKendry, et al. Disentangling mechanical and mass effects on nanomechanical resonators. *Applied physics letters*, 96(2):023113, 2010.
- [51] Daniel Ramos, Maria Arroyo-Hernandez, Eduardo Gil-Santos, Hien Duy Tong, Cees Van Rijn, Montserrat Calleja, and Javier Tamayo. Arrays of dual nanomechanical resonators for selective biological detection. *Analytical chemistry*, 81(6):2274–2279, 2009.
- [52] Eduardo Gil-Santos, Daniel Ramos, Anirban Jana, Montserrat Calleja, Arvind Raman, and Javier Tamayo. Mass sensing based on deterministic and stochastic responses of elastically coupled nanocantilevers. *Nano letters*, 9(12):4122–4127, 2009.
- [53] MS Hanay, S Kelber, AK Naik, D Chi, S Hentz, EC Bullard, E Colinet, L Duraffourg, and ML Roukes. Single-protein nanomechanical mass spectrometry in real time. *Nature nanotechnology*, 7(9):602–608, 2012.

- [54] Stephen M Heinrich and Isabelle Dufour. Toward higher-order mass detection: Influence of an adsorbate's rotational inertia and eccentricity on the resonant response of a bernoulli-euler cantilever beam. *Sensors*, 15(11):29209–29232, 2015.
- [55] Silvan Schmid, Luis Guillermo Villanueva, and Michael Lee Roukes. *Fundamentals of Nanomechanical Resonators*. Springer, 2016.
- [56] Daniel J. Rixen. Engineering dynamics. Delft University of Technology - Faculty of Mechanical, Maritime and Materials Engineering - Section of Engineering Dynamics, Sept 2008.
- [57] Singiresu S Rao and Fook Fah Yap. *Mechanical vibrations*. Pearson Education South Asia Pte Ltd, 5 edition, 2011.
- [58] M Gürçöze. On the eigenfrequencies of a cantilever beam with attached tip mass and a spring-mass system. *Journal of Sound and Vibration*, 190(2):149–162, 1996.
- [59] HJ Ensikat and W Barthlott. Liquid substitution: a versatile procedure for sem specimen preparation of biological materials without drying or coating. *Journal of Microscopy*, 172(3):195–203, 1993.
- [60] Jeanie L Drury and David J Mooney. Hydrogels for tissue engineering: scaffold design variables and applications. *Biomaterials*, 24(24):4337–4351, 2003.
- [61] Tommaso Baldacchini. *Three-dimensional Microfabrication Using Two-photon Polymerization: Fundamentals, Technology, and Applications*. William Andrew, 2015.
- [62] Bojan Ilic, D Czaplewski, Harold G Craighead, Pavel Neuzil, Christine Campagnolo, and Carl Batt. Mechanical resonant immunospecific biological detector. *Applied physics letters*, 77(3):450–452, 2000.
- [63] Alexander Bietsch, Jiayun Zhang, Martin Hegner, Hans Peter Lang, and Christoph Gerber. Rapid functionalization of cantilever array sensors by inkjet printing. *Nanotechnology*, 15(8):873, 2004.
- [64] Gerald Göring, Philipp-Immanuel Dietrich, Matthias Blaicher, Swati Sharma, Jan G Korvink, Thomas Schimmel, Christian Koos, and Hendrik Hölscher. Tailored probes for atomic force microscopy fabricated by two-photon polymerization. *Applied Physics Letters*, 109(6):063101, 2016.
- [65] Rick Waasdorp, Oscar van den Heuvel, Floyd Versluis, and Bram Hajee. Accessing individual 25-micron diameter nozzles of a desktop inkjet printer to dispense picoliter droplets on demand. *Manuscript in preparation*, 2016. not published.
- [66] Nicholas Ferrell, James Woodard, and Derek Hansford. Fabrication of polymer microstructures for mems: sacrificial layer micromolding and patterned substrate micromolding. *Biomedical microdevices*, 9(6):815–821, 2007.
- [67] Balaram Gajra, Saurabh S Pandya, G Vidyasagar, Haribhai Rabari, Ronak R Dedania, and Srinivasa Rao. Poly vinyl alcohol hydrogel and its pharmaceutical and biomedical applications: A review. *International Journal of Pharmaceutical Research*, 4(2):20–26, 2012.
- [68] IHS Markit Inc. *Chemical Economics Handbook: Synthetic Water-Soluble Polymers*. IHS Markit, 2016.
- [69] Shoji Maruo, Osamu Nakamura, and Satoshi Kawata. Three-dimensional microfabrication with two-photon-absorbed photopolymerization. *Optics letters*, 22(2):132–134, 1997.
- [70] Carlo Liberale, Gheorghe Cojoc, Patrizio Candeloro, Gobind Das, Francesco Gentile, Francesco De Nage-lis, and Enzo Di Fabrizio. Micro-optics fabrication on top of optical fibers using two-photon lithography. *IEEE Photonics Technology Letters*, 22(7), April 2010.
- [71] Anna Zakhurdaeva, Philipp-Immanuel Dietrich, Hendrikand Hölscher, Christian Koos, Jan G Korvink, and Swati Sharma. Custom-designed glassy carbon tips for atomic force microscopy. *Micromachines*, 2017.
- [72] Robert J Goldston and Paul H Rutherford. *Introduction to Plasma Physics*. Institute of Physics Publishing, 1995.

- [73] C Jeffrey Brinker and George W Scherer. *Sol-gel science: the physics and chemistry of sol-gel processing*. Academic press, 2013.
- [74] The Engineering ToolBox. Typical properties of engineering materials like steel, plastics, ceramics and composites. retrieved June 2017.
- [75] Sigma-Aldrich. Product specification. Poly(3,4-ethylenedioxythiophene)-poly(styrenesulfonate) 1.3 wt dispersion in H₂O, conductive grade, 2017.
- [76] Enrico Domenico Lemma, Francesco Rizzi, Tommaso Dattoma, Barbara Spagnolo, Leonardo Sileo, Antonio Quattieri, Massimo De Vittorio, and Ferruccio Pisanello. Mechanical properties tunability of three-dimensional polymeric structures in two-photon lithography. *IEEE Transactions on Nanotechnology*, 16(1):23–31, 2017.
- [77] BW Hoogenboom, PLTM Frederix, JL Yang, S Martin, Y Pellmont, M Steinacher, S Zäch, E Langenbach, H-J Heimbeck, Andreas Engel, et al. A fabry-perot interferometer for micrometer-sized cantilevers. *Applied Physics Letters*, 86(7):074101, 2005.
- [78] Douglas M Photiadis and John A Judge. Attachment losses of high q oscillators. *Applied Physics Letters*, 85(3):482–484, 2004.
- [79] Xiaoping Li, Wan Y Shih, Ilhan A Aksay, and Wei-Heng Shih. Electromechanical behavior of pzt-brass unimorphs. *Journal of the American Ceramic Society*, 82(7):1733–1740, 1999.
- [80] Bernhard (ed.) Schrader. *Infrared and Raman Spectroscopy*. VCH Publishers Inc.: New York, 1995. Chapter 4.
- [81] Lee Zhou, FX Lee, W Wilcox, and J Christensen. Magnetic polarizability of hadrons from lattice qcd. *Nuclear Physics B-Proceedings Supplements*, 119:272–274, 2003.
- [82] Li Jia Jiang, Yun Shen Zhou, Wei Xiong, Yang Gao, Xi Huang, Lan Jiang, Tommaso Baldacchini, Jean-Francois Silvain, and Yong Feng Lu. Two-photon polymerization: investigation of chemical and mechanical properties of resins using raman microspectroscopy. *Optics letters*, 39(10):3034–3037, 2014.
- [83] James Stewart. *Calculus (early transcendentals)*. Brooks/Cole Publ. Co, 6th edition, 2008. ISBN ISBN-13: 987-0-495-38273-7.